Extreme nonlinear optics in highly excited semiconductors

Dissertation

Zum Erlangen des akademischen Grades

Doctor rerum naturalium (Dr. rer. nat.)

---

vorgelegt dem Rat der

Physikalisch-Astronomische Fakultät

der Friedrich-Schiller-Universität Jena

von M.Sc. Richard Hollinger

geboren am 27.05.1989

Gutachter

1. *Prof. Dr. Christian Spielmann*
   Institut für Optik und Quantumelektronik
   Friedrich-Schiller-Universität Jena

2. *Jun. Prof. Dr. Giancarlo Soavi*
   Institut für Festkörperphysik
   Friedrich-Schiller-Universität Jena

3. *Prof. Dr. Giulio Cerullo*
   Institut für Physik
   Polytechnikum Mailand

Tag der Disputation: 09.09.2020

Zusammenfassung

In dieser Arbeit werden extreme nichtlineare optische Phänomene in hoch angeregten ZnO Halbleiterproben untersucht. ZnO hat eine Bandlücke von 3,2 eV im nahen ultravioletten Spektralbereich und die optische Anregung erfolgt mit starken Lichtfeldern im nahen bis fernen Infrarot. Folglich ist die Energie der Photonen sehr viel kleiner als die Bandlücke des Materials. Bei den optischen Phönomenen, die untersucht wurden, ist die Reaktion des Materials durch eine nichtlineare Abhängigkeit des Ausgangs- von der Eingangssignalstärke gekennzeichnet. Insbesondere wurde die kohärente Umwandlung von Laserlicht in hohe Ordnungen der ursprünglichen Lichtfrequenz, auch bekannt als Erzeugung hoher Harmonischer (HHG), und optisch gepumptes Lasing untersucht. HHG in Festkörpern resultiert aus einer Kombination von Laserfeld getriebenen nichtlinearen Intraband-Strömen und Interband-Polarisationsfeldern, und Lasing ist das Ergebnis der Verstärkung von Licht durch stimulierte Emission.

HHG von Laserpulsen im mittleren IR wurde in stark optisch angeregten kristallinem ZnO untersucht. Die gemessene HHG Emission zeigt ein Sättigungsverhalten und eine starke spektrale Blauverschiebung der harmonischen Ordnungen als Funktion der freien Ladungsträger. Darüber hinaus führen interatomare Kräfte aufgrund einer starken Modifikation der elektronischen Struktur zu einer Verschiebung der Gitterionen. Ein Pump-Probe-Experiment wurde durchgeführt, um die transiente Modulation des HHG-Prozesses als Funktion des Schwingungszustands der Gitterionen zu bestimmen. Die gemessenen Modulationsfrequenzen stimmen mit den charakteristischen optischen Phononenfrequenzen von ZnO überein. Folglich zeigte das Experiment die Wechselwirkung der Elektronen mit den Gitterionen auf einer Zeitskala kürzer als die halbe Schwingungsperiode des Laserfeldes.

Laserpulse im mittleren IR-Spektralbereich mit wenigen Zyklen und kontrollierbarer absoluten phase (carrier envelope phase, CEP) wurden zur Erzeugung hoher Harmonischer in kristallinem ZnO benutzt, um eine einfache Methode zur Vermessung des relativen CEP des Laserpulses zu demonstrieren. Hierfür wurde die Interferenz spektral überlappender harmonischer Ordnungen ausgewertet.

Lasing setzt ein, wenn die Vestärkung aufgrund der stimulierten Emission die Verluste übersteigt. Um Verstärkung zu ermöglichen, muss die angeregte Ladungsträgerdichte einen Schwell-

wert übersteigen (Inversion). Laseremission aufgrund optischer Anregung mit ultravioleten Licht in polykristallinen ZnO-Dünnfilmen und ZnO-Nanodrähten (NW) wurde bereits demonstriert. In dieser Arbeit werden jedoch starke Lichtfelder im Spektralbereich vom nahen IR (0,8 μm, 1,5 eV) bis zum fernen IR (10 μm, 0,13 eV) benutzt, um optisch gepumptes Lasing in polykristallinen ZnO-Dünnfilmen und ZnO-NWs zu erreichen. Dabei ist das Verhältnis der Materialbandlücke zur Photonenenergie im Bereich zwischen 3 und 26.

Die Laser- und spontanen Photolumineszenz (PL)-Emission von ZnO-Dünnfilmen wurde gemessen, um die Auswirkung einer Materialdotierung und den Effekt der Pumplaserpolarisation (Elliptizität) auf die Laserschwelle bzw. die Lichtabsorption zu untersuchen. In Aluminium dotierten ZnO-Dünnschichtproben ist die Pumpschwellenintensität im Vergleich zu einer intrinsischen Probe reduziert und Licht im nahen IR bei 0,8 μm wird effizienter über einen Drei-Photonen-Absorptionsprozess in ZnO absorbiert, wenn der Pumplaser linear anstelle von zirkular polarisiert ist. Die Messung der PL-Emission von Dünnschichtproben als Funktion der Pumplaserpolarisation stellt eine einfache Methode zur zerstörungsfreien Bestimmung des Absorptionskoeffizienten von zirkular polarisiertem Licht dar.

Die Schwellwerte der Pumplaserintensität und des Verstärkungskoeffizienten um Lasing in ZnO-NW, angeordnet in vertikal ausgerichteten Arrays, zu erreichen, wurden experimetnell verglichen. Die Ergebnisse ergaben, dass die Emissionseigenschaften von NW Arrays, durch die Einzeldrahtparameter definiert sind.

Aufgrund der starken elektrischen Felder und der Licht-Materie-Wechselwirkung fern der Absorptionsresonanz erfolgt die Absorption von Licht über Interbandanregung aufgrund von Multiphotonenabsorption und Tunneln sowie Elektron-Elektron-Wechselwirkung (Stoßionisation) als Folge der Intraband-Elektronenbeschleunigung. Die Rolle der Interband- und Intraband-Absorptionsprozesse wurde durch Vergleichen der experimentellen Ergebnisse mit Berechnungen mittels eines Ratengleichenmodelles identifiziert.

Abstract

This thesis studies extreme nonlinear optical phenomena in highly excited ZnO semiconductor samples. ZnO with a band gap of 3.2 eV, in the near-ultraviolet spectral range, is irradiated with far-off resonance strong light fields in the near to the far-infrared. The response of the matter is characterized by a nonlinear dependence of the output on the input signal strength. Specifically, the coherent conversion of laser light into high orders of the original frequency, also known as high harmonic generation (HHG) and optically pumped lasing were investigated. HHG in solids results from a combination of laser field driven nonlinear intraband currents and interband polarization fields and lasing is the result of light amplification by stimulated emission.
HHG from mid-IR laser pulses was investigated in crystalline bulk ZnO far out of its equilibrium state. As a result the saturation of the harmonic radiation and a strong spectral blueshift of the harmonic orders were measured as a function of the free carrier density. Furthermore, interatomic forces due to strong modification of the electronic structure lead to lattice ion displacement. Performing a pump-probe experiment, the transient modulation of the HHG process reveals the vibration state of the material. The modulation frequency overlaps with the characteristic optical phonon frequencies of ZnO. Consequently, the experiment revealed an interaction of the ionic- and electronic structure on a timescale below the oscillation period of the laser field. Using few-cycle and CEP controllable mid-IR laser pulses to generate high harmonics in crystalline ZnO, a simple method to measure the relative CEP of the laser pulse was demonstrated using the interference of spectrally overlapping harmonic orders.
Lasing sets in when the material gain, due to stimulated emission, overcomes the material losses. For that, the excited electron density has to overcome a threshold value (inversion). Optical pump lasing was demonstrated upon UV pumping in polycrystalline ZnO thin films and ZnO nanowires (NW). However here, strong light fields in spectral range from the near-IR (0.8 μm, 1.5 eV) to the far-IR (10 μm, 0.13 eV) optically pump lasing in polycrystalline ZnO thin films and ZnO NWs. Thus, the ratios of the material band gap to the photon energy covered the range from 3 to 26.
Studying the lasing and the spontaneous photoluminescence (PL) emission from ZnO thin films, the effect of Aluminium doping and the effect of the pump laser ellipticity on the lasing thresh-

old and light absorption, respectively, was determined. Aluminium doped ZnO thin film sample reduce the pump threshold intensity compared to an intrinsic sample and near-IR light at $0.8\,\mu$m is more efficient absorbed via a three photon absorption process in ZnO when the laser is polarized linearly instead of circularly. Measuring the PL emission from thin film samples as a function of the pump laser polarization, depicts a simple method to determine the absorption coefficient for circular polarized light in a non-destructive manner. Comparing the pump laser threshold intensity with the threshold gain value, which were determined by the averaged parameters of the ZnO NW forming a vertically aligned array revealed that the emission properties of the NW array is defined by the single wire parameters.

Due to the strong applied electric fields and the light-matter interaction far-off the resonance, the absorption of light via interband excitation occurs due to the multiphoton absorption and tunneling as well as electron-electron interaction (impact ionization) upon intraband free carrier absorption. The contribution of the interband and intraband absorption processes were identified by comparing the experimental results with calculations from a rate equation laser model.

Contents

Chapter 1

Introduction

From photosynthetic pathways in plants to generate oxygen [1], to the use of photovoltaics in semiconductors to generate electrical current [2], the absorption of sun light is from striking importance in our daily life.
It was Albert Einstein in 1905 [3] who suggested that light can only be absorbed by exciting a electron, when the photon energy is larger than the work function/excitation energy of the matter. In this microscopic explanation, light is assumed to be a particle that carries an energy proportional to its frequency. In 1931 Maria Göppert-Mayer predicted theoretically the absorption of photons with energies smaller than the band gap via virtual states, commonly called multiphoton absorption [4]. Here the absorption probability depends not only on the light frequency but additionally on the photon density, i.e. the light intensity. In 1934, Clarence Zener theoretically predicted that strong electromagnetic fields are able to perturb the electronic structure of matter enabling electrons to tunnel from the ground to an excited state [5]. The absorption probability, due to electron tunneling, depends only on the field strength of the electromagnetic wave and is independent on the wavelength and can thus be fully understood in the wave picture of light [5].
The multiphoton absorption process was experimentally demonstrated in 1961 right after the invention of the laser [6] and led among many other striking innovations to the invention of multiphoton microscopy, a nowadays indispensable biological imaging method [7, 8]. Even if it seemed impossible decades ago [1], applying strong electric fields in the range of V/Å provided by few cycle laser pulses with photon energies far from resonances in solid materials, is nowadays much more than a theoretical playground. Revolutionizing applications of light field driven petahertz electronics have been experimentally demonstrated [10, 11, 12, 13, 14]. Here the conductivity of condensed matter is manipulated by light field induced carrier injection via

[1] "...the huge fields required for Bloch oscillations in a bulk semiconductor could never be reached.", from the Nobel Prize autobiography (2000) of Herbert Kroemer [9]

Zener tunneling on a sub optical cycle time scale [15, 16].
The excitation of carriers via Zener-tunneling is a key aspect in light wave driven petahertz electronics. Due to the nature of the process, tunneling appears predominantly in slow oscillating fields, i.e. long wavelength radiation. However, slowly varying strong fields heat free electrons very efficiently and thus cause material damage due to an avalanche-like excitation of charge carriers by electron impact events. To avoid irreversible material modifications, ultrashort laser pulses, down to a few cycles of the electromagnetic field allow mitigating this impact. These pulses in the middle- to far-infrared spectral range became available only very recently. Thus the interaction of ultrashort laser pulses in the near to the far IR range with condensed matter as well as the absorption cross sections are unexplored.
Recently, High order Harmonic Generation (HHG) from mid-IR laser pulses in semiconductor materials has been reported to study light wave driven sub cycle electron movements [17, 18]. High field strengths are required to observe a strong HHG signal, which is associated with a high number of excited charge carriers. This may affect the HHG process since the electronic structure altered significantly. To study the electron motion, using HHG, a detailed knowledge about excited carrier density and its effect on the HHG process is needed.
In this work extrem nonlinear phenomena, namely HHG and lasing, appearing in highly excited semiconductor material as a result of strong light field, far from electronic resonance, interaction with nanomaterials and bulk semiconductors were studied. High harmonic emission was generated in highly excited bulk semiconductor zinc oxide (ZnO) far out of its equilibrium state and the dynamical effects of the excited carriers on the HHG process were investigated. A spectral blueshift of the harmonic emission and modulations of the transient high harmonic signal reveal that the strong modification of the electronic structure does not only affect the HHG-process but further leads to an interaction of the ionic structure and the field driven electrons. Using ZnO nanomaterials (thin films and nanowires), stimulated emission optically pumped via tunnel and multiphoton excitation was demonstrated for the first time. Beside the potential applications of nonlinear optically pumped nanoscale lasers, the onset of lasing was used to investigate light absorption in a wide spectral range covering the multiphoton and tunneling excitation regime. The results show that carrier excitation via electron-electron interaction after intraband, free carrier, absorption play a significant role for long wavelength light.
This work is structured as follows. This introduction is followed by a brief discussion about the fundamentals of the interaction of intense laser light with semiconductors, optically pumped semiconductor lasers and high harmonic generation in solids (Chapter 2). In Chapter 3 results on HHG in highly excited bulk ZnO material will be presented. The following sections report strong light field, far off-resonance, optically pumped lasing in ZnO thin films (Chapter 4) and nanowires (Chapter 5). After summarizing the work (Chapter 6), in Chapter 7 future perspectives and preliminary results from follow-up experiments are presented.

Chapter 2

Extreme nonlinear optics

Presented in this chapter are the fundamentals involved in the nonlinear interaction of intense laser light with condensed matter. Section 2.1 discusses the physics behind the absorption of ultrashort femtosecond laser pulses in the near (0.8 μm, 1.5 eV) to the far-IR (10 μm, 0.13 eV) spectral range in the wide band gap semiconductor material ZnO (E_g = 3.2 eV). Since the ratio of the ZnO band gap E_g to the used photon energies varies between 3 and up to 26 the absorption of light is a highly nonlinear function of the laser wavelength and intensity. Due to the much lower photon energy compared to the band gap, the interaction is also called far off-resonance. After introducing the interband absorption mechanism of multiphoton absorption and tunneling, the additional excitation channel of impact excitation resulting from electron intraband heating are discussed. To get an idea about the expected number density of excited carriers resulting from inter- and intraband excitation processes and thus an upper field strength limit which can be applied, both processes are considered using a rate equation model. The following Section 2.2 introduces the fundamentals of optically pumped semiconductor lasers. Three main components determine a laser device, namely: an external pump source, a feedback mechanism and a gain medium. The pumping of the gain material, aiming to achieve population inversion, using femtosecond laser pulses will be discussed in Section 2.1. It is assumed that due to the high excited carrier density, the gain mechanism is provided by an electron hole plasma (EHP). Two different materials systems, namely quasi one dimensional nanowire (NW) and quasi two dimensional (nm thick) thin film samples are used to study stimulated emission and lasing in far off-resonance excited ZnO samples. Further the responsible feedback mechanism is presented in Section 2.2.2. Band-to-band recombination processes subsequent electron excitation are delayed to the absorption process due to thermalization processes. Radiation can also be emitted coherently with the strong laser field due to introduced nonlinear intraband currents and interband polarization fields. These processes happen in every half cycle of the laser electric field which leads to the emission of a frequency comb whose frequencies are (high) harmonics of the

driver laser frequency. This high harmonic generation (HHG) process is discussed in the last part of this chapter (Section 2.3).

2.1 Strong field, far off-resonance, light matter interaction

Nowadays intense femtosecond laser pulses can be generated in a broad spectral range, covering the ultraviolet up to the far-infrared, using optical parametric amplifications systems (See Appendix A and B for more details). Presented in this section, are the fundamentals needed to understand the interaction of strong laser fields with condensed matter, where the material band gap E_g is much larger than the photon energy $\hbar\omega$ of the laser light. In Section 2.1.1 interband electron excitation as a function of the laser wavelength and intensity is discussed and a quantitative description of the electron generation rate will be introduced. Due to the high field strength necessary in off-resonance interband excitations, the quasi free electrons (holes) in the conduction band (valence band) are efficiently accelerated, also known as carrier heating, intraband excitation or free carrier absorption. The fast electrons will transfer their kinetic energy to bound electrons via an inelastic electron-electron scattering process which may result in impact excitation of the bound electrons. A quantitative description of free carrier absorption based on the Drude model is presented in Section 2.1.2. In Section 2.1.3 the inter- and intraband excitation rate are used in a combined model to simulate the number density of excited electrons as a function of the laser wavelength, intensity and pulse duration.

2.1.1 Interband electron excitation

The concept of electron excitation in solids is depicted in Figure 2.1 for three different excitation regimes, determined by the wavelength (frequency) and the intensity of the light. In semiconductors a electron is excited, when it is lifted from the highest occupied states in the valence band (VB) to a free state in the conduction band (CB). The energetic gap between the VB and CB is called band gap E_g.

Using the particle picture of light, in the frame of the quantum theory of light, A. Einstein explained in his famous work the photo effect: the mechanism of electron excitation in the case of above bandgap single-photon absorption (Fig. 2.1 a) [3]. Here, the excitation of an electron is only possible if the photon energy, determined by the light frequency, is larger than the material band gap. The excitation rate is proportional to the number of impinging photons given by the light intensity I and the electron density in the CB is naturally determined by the pumping fluence.

In case of photons with energies below the bandgap an electron can be excited in a step-like process using virtual states (Fig. 2.1 b). This process requires a high number of photons during the lifetime of the virtual state and thus a substantially higher level of light intensity. Thus, in this

nonlinear interaction regime, the excitation probability depend not only on the photon energy but also on the intensity of the incident pumping light. However, the multiphoton absorption process can be still described solely by the particle picture of light.
With increasing gap to photo energy ratio, the intensity of the light has to be increased to achieve a noticeable electron generation rate. For a sufficiently high intensity, i.e. strong electric field, the pertubation on the electronic structure can not be neglected. As a result, the electronic band is bent, which enables the tunneling of electrons from the valence to the conduction band (Fig. 2.1 c), also known as Zener-tunneling [5]. The light acts as classic Coulomb force and electron excitation happens entirely due to the wave nature of the light, thus excitation becomes independent on the photon energy but solely depends on the field strength of the pumping light.

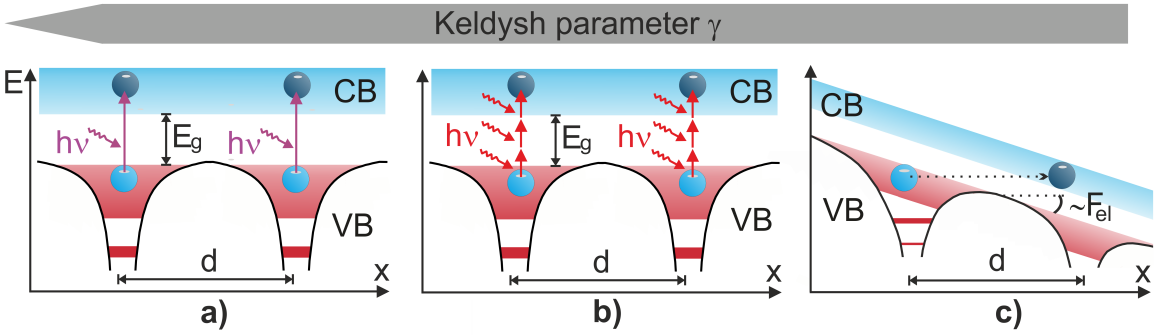

Figure 2.1: Photoexcitation mechanism as a function of the Kelysh parameter γ (see Equation 2.3). a) single-photon and b) multi-photon absorption of quanta with the energy $h\nu$, or c) tunneling of carriers from the VB to the CB through a barrier formed by an intense light-field F_{el}. Here, the potentials from two neighboring atoms/ions in a lattice, separated by a lattice period d, are schematically depicted as a function of the spatial coordinate x.

A respective theory describing excitations in semiconductors as function of the light wavelength (or frequncy ω) and field strength was developed by L.V. Keldysh back in 1964 [19].
The excitation rate is calculated using the Keldysh expression [20][2]

$$W_K(I,\omega) = 2\frac{2\omega}{9\pi}\left(\frac{m^*\omega}{\hbar\sqrt{\gamma}}\right)^{3/2} \cdot Q\left(\gamma, \frac{E_{\mathrm{g,eff}}}{\hbar\omega}\right) \cdot \exp\left[-\pi\langle\frac{E_{\mathrm{g,eff}}}{\hbar\omega+1}\rangle\frac{K(\Phi)-E(\Phi)}{E(\Theta)}\right], \tag{2.1}$$

where

$$Q(\gamma,x) = \sqrt{\frac{\pi}{2K(\Theta)}} \cdot \sum_{n=0}^{\infty} \exp\left[-\pi\frac{K(\Phi)-E(\Phi)}{E(\Theta)}n\right] \cdot \Psi\left[\sqrt{\frac{\pi(2\langle x+1\rangle - 2x+n)}{2\cdot K(\Theta)\cdot E(\Theta)}}\right]. \tag{2.2}$$

[2]Note, in the original publication from Keldysh [19] is a misprint, which was corrected in [20].

K and E are complete elliptic integrals with $\Theta = 1/(1+\gamma^2)$ and $\phi = \gamma^2/(1+\gamma^2)$.

$$\gamma = \frac{\omega\sqrt{m^* E_\mathrm{g}}}{e\mathrm{F}_{el}} \tag{2.3}$$

is the Keldysh parameter, $\Psi(x) = \int_0^x \exp(\psi^2 - x^2)\mathrm{d}\psi$ is the Dawson integral, E_g is the intrinsic band gap, m^* is the effective electron mass, ω is the laser frequency, e is the elementary charge and F_{el} is the amplitude of the laser pulse electric field related to the laser pulse intensity I by $\mathrm{F}_{el} = \sqrt{2\mathrm{I}/(\epsilon_0 c)}$ (Eq. A.4), c and ϵ_0 denote the vacuum velocity of light and permittivity, $E_{\mathrm{g,eff}} = 2/\pi E_\mathrm{g}\left[\sqrt{1+\gamma^2}/\gamma^2 \cdot E(\Theta)\right]$ is the bandgap value modified due to the Stark shift [20].
The Keldysh parameter (Eq. 2.3) is used to determine if single- or multiphoton absorption or tunneling is the dominant strong-field excitation mechanism. For $\gamma > 1$ valence band electrons are excited by multiphoton absorption and the excitation rate

$$W_\mathrm{MP}(I,\omega) = 2\frac{2\omega}{9\pi}\left(\frac{m^*\omega}{\hbar\sqrt{\gamma}}\right)^{3/2}\Psi\left[\sqrt{2N-2x}\right]\cdot\exp\left[2N\left(1-\frac{1}{4\gamma^2}\right)\right]\cdot\left(\frac{1}{16\gamma^2}\right)^N \tag{2.4}$$

depends on the laser intensity. The rate scales with I^N, where N=<$E_\mathrm{g}^\mathrm{MP}/\hbar\omega$> is the number of absorbed photons with <> denoting the integer part of a number. The work performed by the laser field includes the excitation of the electron from a bound state in the VB to a free state in the CB and the electron acceleration given by the electron quiver energy (pondermotive energy U_p). Thus, the effective band gap

$$E_\mathrm{g}^\mathrm{MP} = E_\mathrm{g} + U_\mathrm{p} \tag{2.5}$$

is given by the sum of the intrinsic material band gap and the pondermotive energy

$$U_\mathrm{p} = \frac{e^2\lambda_0^2 F_\mathrm{el}^2}{16\pi^2 m^* c^2}. \tag{2.6}$$

For intense, low frequency light fields, the Keldysh parameter becomes $\gamma < 1$ indicating a transition towards a predominantly tunnel ionization governed regime. The excitation rate

$$W_\mathrm{TUN}(I,\omega) = 2\frac{2\omega}{9\pi^2}\frac{E_\mathrm{g}}{\hbar}\left(\frac{m^* E_\mathrm{g}}{\hbar^2}\right)^{3/2}\cdot\exp\left[-\frac{\pi}{2}\frac{E_\mathrm{g}\gamma}{\hbar\omega}\left(1-\frac{\gamma^2}{8}\right)\right] \tag{2.7}$$

is then $\propto \exp\left[-\pi/2(E_\mathrm{g}\sqrt{m^* E_\mathrm{g}})/(e\hbar F_\mathrm{el})\right]$ (i.e. proportional to the exponential function of the laser electric field strength F_el).
To summaries, the Keldysh formalism provides the analytic expression W_K (later called "full Keldysh"), which is given in Eq. 2.1, to calculate the electron generation rate in semiconductors for an arbitrary light intensity and wavelength. In the theory a unitless parameter, the so-called Keldysh parameter γ (Eq. 2.3), determines if the electron excitation happens by multiphoton

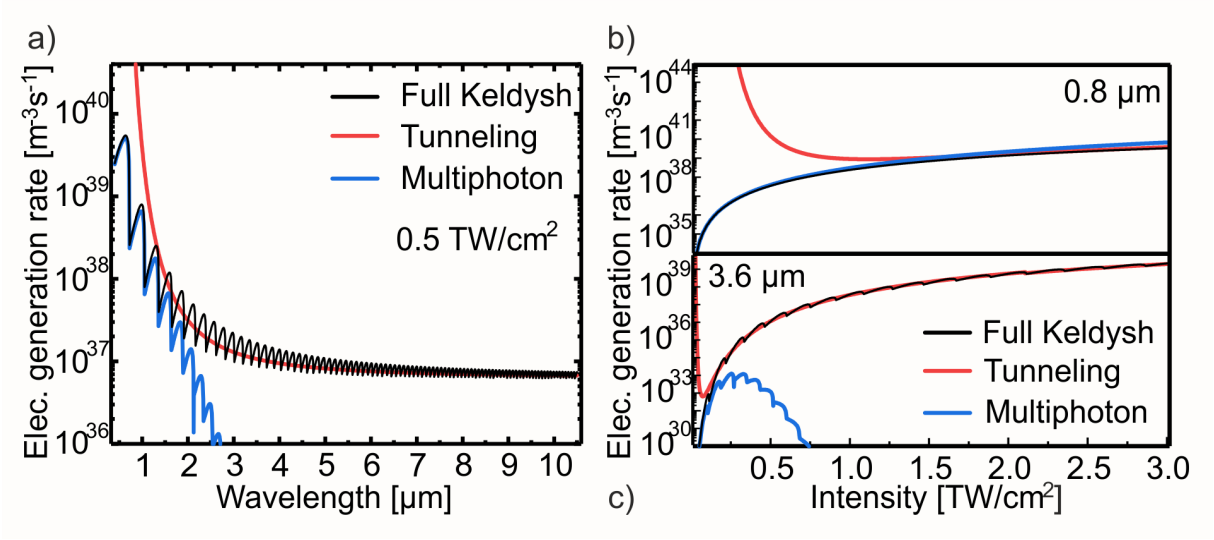

Figure 2.2: Calculated electron generation rate using the Keldysh formalism, when the formulas of full Kelysh (black line, Eq. 2.1), the tunneling ($\gamma < 1$, Eq. 2.7) and multiphoton ($\gamma > 1$, Eq. 2.4) approximation are applied. a) Wavelength dependence of the electron generation rate for a fixed field intensity of 0.5 TW/cm^2. b) and c) Electron generation rate as a funciton of the laser intensity for a fixed laser wavelength of 0.8 and 3.6 μm.

absorption (γ>1) or tunneling (γ<1). In the cases of γ>1 and γ<1 the excitation rate W_K can be simplified to the expressions W_{MP} and W_{TUN} given in Equation 2.4 and 2.7, respectively.

Using ZnO material parameters, $m^* = 0.29m_0$, $E_g = 3.2$ eV and equation 2.1, the calculated dependence of the carrier excitation rate as a function of the laser wavelength and for a fixed laser intensity of 0.5 TW/cm^2 is shown as a black line in Figure 2.2 a. In the limit of $\gamma > 1$ the rate follow the multiphoton excitation solution given by Equation 2.4 (red line), which exhibits a sharp intensity dependence with pronounced oscillations, corresponding to transition from N to (N+1) photon absorption and a strong decrease for wavelengths larger 1.5 μm. As given in Equation 2.5, the work performed by the laser field on the bound as well as free electron is considered. Thus, the band gap is wavelength and intensity dependent leading to the step-like dependences. The steps from a N to a N+1 photon absorption process follows the classical known relation N=<$E_g/\hbar\omega$> only for low intensities and short wavelengths.

In the opposite limit of $\gamma < 1$ the rate shows an asymptotic saturation and follows the tunnel excitation solution given by Equation 2.7. The saturation as a function of the wavelength can be easily understood from the physical mechanism of tunnel excitation based on classical work of the laser electric field on the electron. In this case, the photon energy does not matter anymore and only the electric field strength governs the tunneling process and the excitation rate is almost wavelength independent for longer wavelengths. Note that the tunnel asymptotic solution strongly overestimates the excitation rate for wavelengths below 1.5 μm in comparison to the exact and multiphoton asymptotic solutions. As can be seen from the validity of the multiphoton and tunneling limit, the transition from multiphoton to tunnel excitation occurs for laser

wavelengths at around 1.5 μm in the case of ZnO and the used simulation parameters.
Figure 2.2 b and c depicts the electron generate rate in ZnO material as a function of the light intensity for a fixed wavelength of 0.8 μm and 3.6 μm, respectively. While in the case of 0.8 μm a light intensity of 1.5 TW/cm^2 is needed to reach the tunneling regime (Figure 2.2 b) for 3.6 μm a much lower intensity of 0.15 TW/cm^2 is sufficient (Figure 2.2 c). Therefore, excitation of an electron in ZnO via tunneling is much easier to achieve using long wavelength light.
To derive the analytical Keldysh formula, some approximations are assumed. The electronic structure is simplified by quadratic bands and only monochromatic light matter interaction has been considered. Furthermore in the case of strong excitation no electron correlation effects, like band gap renormalization, are included. Despite these simplifications there is still (55 years after the publication of the Keldysh formula) no equivalent approach (beside time dependent density functional theory) to describe light-solid interaction for an arbitrary light intensity and wavelength.

2.1.2 Intraband free carrier absorption

The high intensities, or high electric field strength, required in the multiphoton absorption and tunneling regime act as additional work on the free electron system. This process in which the electron gains kinetic energy, also known as free carrier absorption (FCA), can be modelled by the Drude model [20, 21, 22]. The accelerated electrons can excite further electrons via impact excitation when their kinetic energy exceeds the band gap. The corresponding excitation rate is given by

$$\frac{\mathrm{d}n_{\mathrm{FCA}}}{\mathrm{d}t} = \frac{n_{\mathrm{e}}^{*}(t)}{E_{\mathrm{c}}}\sigma I(t), \tag{2.8}$$

while $\sigma = \frac{e^2}{m^* \epsilon_0 c \gamma_{\mathrm{s}}} \left(1 + \frac{4\pi^2 c^2}{\lambda^2 \gamma_{\mathrm{s}}^2}\right)^{-1}$ describes the free electron absorption cross section. $n_{\mathrm{e}}(t)$ is the free electron density, $E_{\mathrm{c}} > E_{\mathrm{g}}$ the critical energy, e the elementary charge, m^* the effective electron mass, ϵ_0 the vacuum permittivity, γ_{s} the electron scattering rate and c the speed of light.
The free carrier absorption scales with the laser intensity and wavelength proportional to $I \cdot \lambda^2$. This scaling law with laser intensity and wavelength is identical to the pondermotive energy (U_{p}) used in strong-field laser physics to determine the kinetic energy of an electron accelerated in the laser field. Assuming an oscillation period of the field which is much longer than the scattering time, which is given by $1/\gamma_{\mathrm{s}}$, $\sigma = 2U_{\mathrm{p}}\gamma_{\mathrm{s}}$ applies.
The dependence of the impact ionization on the free electron density $n_{\mathrm{e}}(t)$ implies the possibility of an avalanche process. Here, a chain reaction of excited electrons results in a carrier density above the critical value which may result in material damage. One criteria, responsible if avalanche sets in, is that the electrons gain sufficient kinetic energy during the pulse duration. To avoid the avalanche effect but on the other hand achieve a high excitation density, both in multiphoton absorption and tunneling regime, the laser pules must be sufficiently short (see Fig-

ure 2.5). A quantitative description of the excited electron density due to inter- and intraband absorption processes, also as a function of the laser pulse duration, will be presented in the next section.

2.1.3 Keldysh-Drude excitation model

Gaining quantitative insights into the physics of the wavelength and laser intensity dependent electron excitation rate demands simulations, which includes the interband strong field excitation rate $W_K(I, \omega)$ calculated using the Keldysh formula (given by Eq. 2.1) and the electron impact excitation following subsequent intraband free carrier photo-absorption (FCA), given by eq. 2.8:

$$\frac{\mathrm{d}n_e^*}{\mathrm{dt}} = W_K(I, \omega) + \frac{\mathrm{d}n_{\mathrm{FCA}}}{\mathrm{dt}}. \tag{2.9}$$

A comparison between the calculated excited electron density with (blue) and without (red) considering free carrier absorption (second term in eq. 2.9) as a function of the time during a laser pulse is shown in Figure 2.3 a. For calculations a Gaussian laser pulse at 3.6 μm with 100 fs duration and 0.5 TW/cm^2 intensity was applied, the scattering rate γ_{s} was fixed to $0.3 \cdot 10^{14}$ 1/s (i.e. a scattering time of 30 fs) and the critical energy E_{c} was assumed to be $1.1 \cdot E_{\mathrm{g}}$. The excited carrier density at the end of the pulse is increased by more than one order of magnitude taking free carrier absorption into account. The significance of intraband processes for light absorption was recently experimentally confirmed using an optical pump - XUV(attosecond) probe technique [15].

Figure 2.3 b and c depicts the electron density excited by a 100 fs laser pulse in ZnO material as function of the laser intensity and for fixed wavelengths of 3.6 and 10 μm, respectively. In both cases the calculations are performed with (blue) and without (red) the impact excitation channel subsequent free carrier absorption. Both curves reveal an increasing carrier density when the laser intensity is increased. Due to the λ^2 dependence, (see Equation 2.8) free carrier absorption is much stronger in the case of 10 μm compared to 3.6 μm.

The temporal structure of a continuous growing carrier density build up, shown in Figure 2.3 a, differs significantly from measured [15, 23, 24] and calculated [25, 26, 27] field oscillation resolved dynamics. The calculations are based on quantum mechanical models solving the time-dependent Schrödinger equation and time dependent density functional theory (TD-DFT) methods. There the reversible mutual energy transfer W(t) of a few-cycle laser pulse with the induced polarization field, interpreted as virtual excitations of conduction band electrons [24] is leading to a strong modulation and overshoot of the excited carrier density in the moment the field is present. The actual excited carrier density n_{e} is given by the irreversible transferred energy through $n_{\mathrm{e}} = \mathrm{W(t)}/E_{\mathrm{g}}$ with E_{g} the band gap of the material. Recent comparisons of hybrid TD-DFT calculations in combination with the Drude model compare well with simulations us-

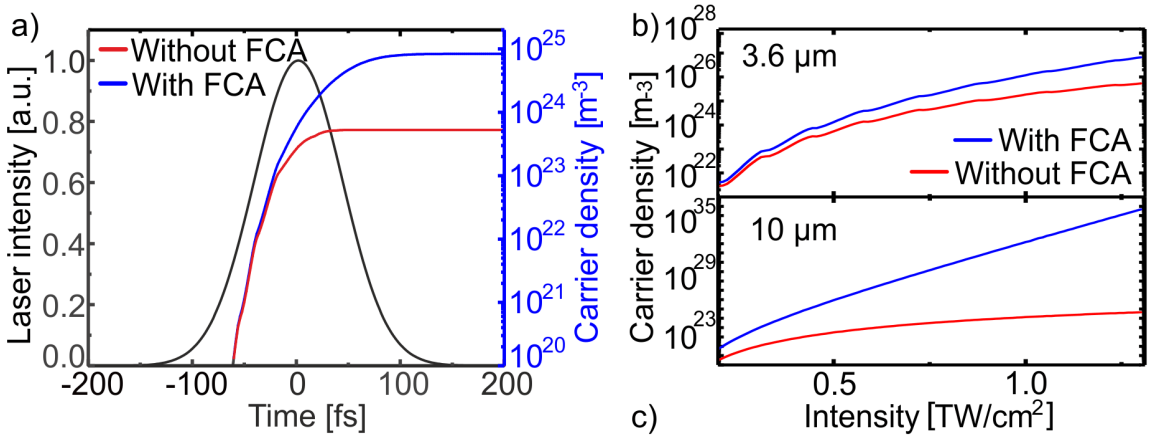

Figure 2.3: Calculated temporal evolution of the free-electron density in ZnO irradiated by a 100 fs pulse at 3.6 μm with a peak intensity of 0.5 TW/cm^2. The scattering rate γ_s and critical energy E_C were set to $0.3 \cdot 10^{14}$ 1/s and $1.1 \cdot E_g$, respectively. The blue and red lines show the total excited electron density with and without free carrier absorption (FCA) while the black line shows the Gaussian shape of laser pulse. b) and c) Laser intensity dependent excited carrier density for 3.6 and 10 μm.

ing the Keldysh together with the Drude formalism to describe inter- and intraband absorption processes[3]. Simulating femtosecond laser ablation dynamics in semicondcutors and dielectrics, beyond the model presented in this chapter have been developed. An overview of the applied models can be found in Ref. [20]. Recently Sergaeva *et al.* [28] presented calculations on the excitation of electrons using the Vinogradov equation instead of the Drude model to calculate the intraband absorption. This work was motivated to overcome the high-scattering rate of the Drude-Keldyh approach [28].

Contribution of free carriers to light absorption

Figure 2.4 depicts the calculated excited electron density as a function of the excitation wavelength using Equation 2.9, with and without the additional excitation channel of impact ionization as a result of free carrier absorption. The used model parameters were a 30 fs scattering time, 0.5 TW/cm^2 laser intensity and 100 fs pulse duration. For this conditions the excited electron density is not affected by the free carrier absorption up to a wavelength of 1.5 μm. The highest electron density of $1 \cdot 10^{26}$ m^{-3} is excited by a laser at 1 μm and decreases to $5 \cdot 10^{24}$ m^{-3} at 1.5 μm.

In the case of longer laser wavelength the simulations without FCA depict a decrease of the excited carriers to roughly $1 \cdot 10^{24}$ m^{-3} at 4.5 μm and a wavelength independent number of excited electrons of $5 \cdot 10^{23}$ m^{-3} in range from 9 to 11 μm. Taking into account intraband processes and impact ionization the excited electron number is roughly constant $1 \cdot 10^{24}$ m^{-3} between 2 and 4 μm and rapidly increasing from $5 \cdot 10^{26}$ m^{-3} to $5 \cdot 10^{27}$ m^{-3} when the laser wavelength is shifted

[3]Private discussion with Silvana Botti and Nicolas Tancogne-Dejean.

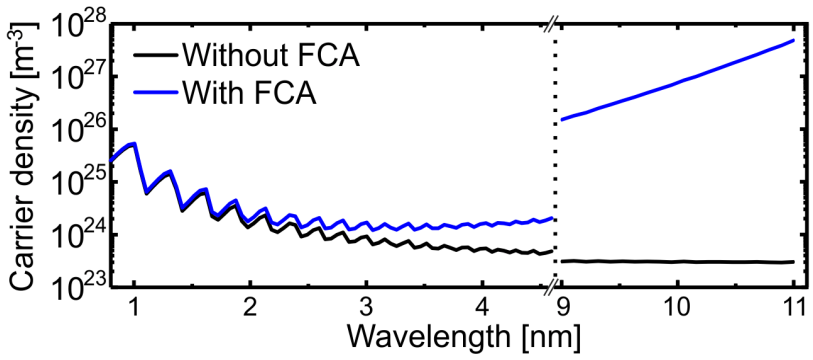

Figure 2.4: Calculated excited electron density using Equation 2.9 with (blue line) and without (black line) free carrier absorption. Used parameters: scattering time 30 fs, pulse duration 100 fs, laser intensity 0.5 TW/cm^2, critical energy $1.1 \cdot E_g$.

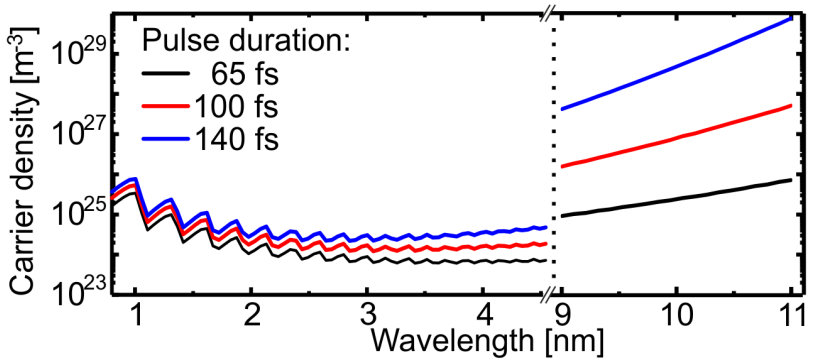

Figure 2.5: Calculated excited electron density using Equation 2.9 as a function of the laser pulse duration. Used parameters: scattering time 30 fs, laser intensity 0.5 TW/cm^2, critical energy $1.1 \cdot E_g$.

from 9 to 11 μm.

The increasing number of the excited electrons as a function of the laser wavelength can be understood by the λ^2 scaling of FCA. For longer wavelengths the electrons which are excited by multiphoton or tunneling excitation are more efficient accelerated (heated up) what finally results in an increased number of impact excitation. Simulations without considering intraband processes result in a wavelength independent number of excited electrons for long wavelengths in accordance with the Keldysh electron generation rate given in Equation 2.1 and shown in Figure 2.2.

Pulse duration dependence of carrier excitation

Figure 2.5 illustrates the calculated excited electron density as a fucntion of the laser pulse duration for a fixed laser intensity of 0.5 TW/cm^2. The parameters for the electron scattering time $1/\gamma_s$ and critical energy E_C in Equation 2.9 are 30 fs and $1.1 \cdot E_g$, respectively. Stretching the pulses from 65 to 140 fs clearly leads to a higher excited carrier density, for instance in the case of 4 μm and 10 μm an increase of 1 and 4 orders of magnitude are achieved, respectively. The higher excited electron density as a function of the laser pulse duration can be explained by the larger time window available for electron acceleration (heating) and consequently higher kinetic energy of the electrons.

Damage threshold criteria

The density of ZnO is $5.6 \cdot 10^6$ g/m^3 which corresponds to $4.2 \cdot 10^{28}$ molecules per m^3 or $160 \cdot 10^{28}$

electrons per m^3. Roughly one tenth of the total amount of ZnO electrons are concentrated in the valence band. A critical electron density, leading to irreversible modifications of the material is reached when ten percent of the valence electrons are excited to the conduction band [23]. Thus the number density of excited electrons should not exceed $5 \cdot 10^{27}\ m^{-3}$ to avoid any damage.

2.2 Lasing in optical pumped semiconductor material

After different regimes of photo-excitation and free carrier absorption were discussed, now the attention will be turned to the remaining two fundamental light-matter interaction processes: spontaneous and stimulated emission. Stimulated emission is especially important in the context of laser radiation. This thesis focuses on the formation of nanolasers in ZnO thin films and NWs.

A classical laser devices consists of three components: a gain medium, a feedback mechanism (resonator) and an external pump source[4]. The external pump source excites electron in the gain medium aiming to generate a population inversion and thus enabling gain which sets in if the stimulated emission dominates over the absorption process [29, 30]. In this thesis only optically pumped semiconductor laser, i.e excitation of electrons by the absorption of photons, using femtosecond laser pulses were investigated. The quantitative description of the wavelength and intensity dependent electron generation rate by the absorption of laser light in semiconductors was given in the previous section. Thus this section is dealing with the remaining parts: gain and the feedback mechanism. The section starts with a description of the gain mechanism (Section 2.2.1) in charge for the amplification of spontaneous emitted photons. Here, the concepts of excitonic and EHP gain are discussed. Next, in Section 2.2.2 the feedback mechanism in quasi one and two dimensional semiconductor systems, namely nanowires and polycrystalline thin films, are discussed.[5] While the NWs form a Fabry-Pérot cylindrical waveguide cavity, in thin films the scattering at grain boundaries results in random lasing. Finally, in Section 2.2.3 a laser rate-equation-model is introduced, allowing to simulate the dynamics and characteristics of semiconductor lasers optically pumped by femtosecond laser pulses.

2.2.1 Gain mechanism

The gain in the NW as well as in thin film laser is provided by the ZnO material forming the NW and the film. The internal gain mechanism responsible for lasing will be discussed in this

[4] There are also laser devices, which lack a resonator and instead use single pass gain. For example X-ray free electron laser works without any feedback mechanism.

[5] Since the size of the NWs and the thin films is much larger than the exciton Bohr radius in ZnO (1.8 nm), electron confinement effects can be neglected throughout this thesis.

section.

Highly exciting a semiconductor material, leads to a strong out of equilibrium and thus normally very complex situation to describe. Research on the gain mechanism in ZnO, done during the last decades [31], verified a strong carrier density and temperature dependence and its detailed description is still part of active research far from the scope of this thesis. For more details the reader is refered to Ref. [30]. A brief review of known optical processes in highly excited semiconductors which enable gain and their dependence on the carrier density and temperature follows. At low carrier densities the emission from free excitons dominates. Increasing the excited carrier density and thus the number excitons, they start to interact with free electrons, phonons and other excitons leading to exciton-electron, exciton-phonon and exciton-exciton scattering. Further the formation of excitons molecules, the so-called biexcitons were reported. Every recombination due to a exciton interaction process results in a characteristic emission line. For highest excitation densities the electron and holes start to screen each other, which prevents the formation of excitons and an electron hole plasma (EHP) is formed. The electron density at which the excitons dissociate and an EHP is formed is called Mott-density and was determined to be around $1 \cdot 10^{24}\,\mathrm{m}^{-3}$ [32].

Due to the weak binding energy, the formation of biexcitons is only stable at cryogenic temperatures [33, 34]. Emission from a exciton-phonon scattering process has been measured for temperatures below 70 K[35]. At room temperature only the exciton-exciton-, exciton-electron-scattering and the EHP have to be considered. Although in literature many experiments on stimulated emission in ZnO are explained by an excitonic or EHP-based stimulated emission process, it was discussed by Klingshirn *et al.* [36], that stimulated emission in ZnO based on excitonic processes at room temperature are very unlikely. The authors argue that the final exciton scattering states get thermally populated with increasing temperature, what leads to a dramatic reduction of the transition probability. Further reported stimulated emission thresholds correspond to carrier densities close to the Mott density [36], where excitons very likely dissociate. As shown in Figure 2.3 after optical pumping by femtosecond laser pulses, in the spectral range from the near to the mid-IR, excited carrier densities above the Mott density can be expected (see Section 2.1.3). Consequently it is assumed that under experimental conditions (excited electron density and temperature) present in this work the gain in ZnO results from an EHP. Note that the transition from a high exciton density to an EHP is not sharp, thus features of both recombination processes will be detected under intermediate conditions.

The spectral evolution of the absorption and gain coefficient of ZnO as a function of the excited carrier density was theoretically determined by Versteegh *et al.*[32]. The absorption coefficient of ZnO material switches its sign, i.e. stimulated emission dominates over absorption, when $2 \cdot 10^{25}\,\mathrm{m}^{-3}$ electrons are excited. In the previous section it was shown that the ZnO material can be excited very above this value and thus making lasing, subsequent far off-resonant exci-

tation, possible. The gain values reported in literature for ZnO material are in the range of 0.1 to 1 μm^{-1} [32, 37].
As a consequence of electron correlation, resulting from the high electron density in an EHP, the bandgap as well as the gain spectrum experience a shift towards lower energies, also known as band gap renormalization [32].

2.2.2 Feedback mechanism

Together with the population inversion inserted by an external pump source in the gain material, a feedback mechanism is essential prerequisite to realize laser emission.

Nanowire

As illustrated in Fig. 2.6 a and b semiconductor NWs provide in principle all necessary prerequisites to design of nanoscale lasers [34, 38, 39]. As discussed before the semiconductor

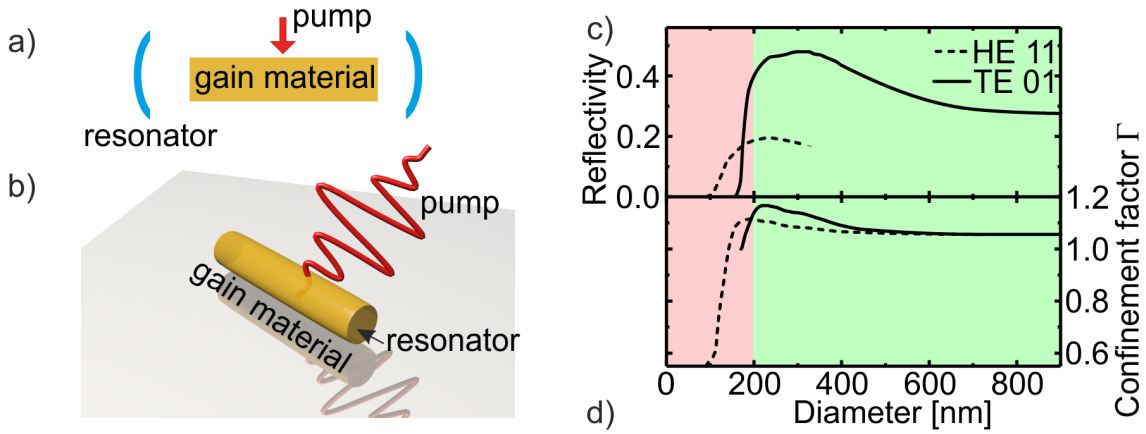

Figure 2.6: Laser feedback mechanism in a Fabry-Pérot cylindrical NW waveguide cavity. a) Schemtic illustration of a classicl laser device. The laser is formed by a gain material, an external pump source and a feedback mechanism (resonator). b) Illustration of experimental situation, a NW is pumped by an ultrashort laser pulse. The image highlights the similarities of a classical laser and a NW laser. c) and d) Calculated reflectivity of the wire end facets and confinement factor as a function of the wire diameter for the two lowest guided modes HE11 and TE01.

material of the wire acts as an optical gain medium [38]. The wave guiding cylindrical geometry together with reflecting end facets naturally form a cavity supporting Fabry-Pérot (FP) modes. The spectral mode spacing

$$\Delta f = \frac{c}{2Ln_r} \tag{2.10}$$

is defined by the cavity (nanowire) length L and the material refractive index n_r. Moreover, a large confinement factor provided by the NW geometry (see Fig. 2.6 d) enables lasing that in practice would not be possible for a different cavity geometry under conditions of the ultrashort

cavity length [40].
Since all components of the NW laser are identified, as a next step the gain threshold to observe stimulated emission can be determined quantitatively. In a single ZnO NW stimulated emission becomes dominant, if the round trip loss in the wire is compensated by the optical gain. This threshold gain g_{th} is given by:

$$\Gamma g_{th} = \alpha_w + \frac{1}{2L}\ln(R_1 R_2). \tag{2.11}$$

With the confinement factor Γ describing the overlap of the guided mode inside the wire with the gain material [34]. The loss on the right-hand side is the sum of the waveguide loss α_w and the mirror losses, which are determined by the reflectivity on the wire-air end facets (R_1, R_2), and the length of the wire L [29]. Since the diameter of the NW is in the order of the wavelength, the mode confinement, the end facet reflectivity, and the transverse mode structure depend strongly on the wire diameter [34, 39]. It is assumed that the transversal mode structure is dominated by the HE11 and/or TE01 mode for wire diameters below and above 200 nm, respectively [41]. Figure 2.6 c and d provides an estimation of the reflectivity and confinement factor for different ZnO wire diameters. The values for wire diameters up to 400 nm have been taken from [34] and extrapolated for larger diameters assuming the plain wave field structure instead of a mode.
For NW with diameters larger than 1 μm whispering gallery modes may appear. This topic will not be discussed here, because the NW used in this work had diameters smaller 1 μm. The interested reader is refered to the following literature [42, 43].

Thin films

Beside NWs, thin films are a well known nanomaterial geometries showing laser emission. While in NW lasers the emission depicts clear resolvable modes which can be linked by their spectral spacing to the FP cavity, lasing from ZnO thin films lacks a unique emission feature. What follows is a verification why random lasing is assumed to be the reasonable feedback mechanism in polycrystalline ZnO thin films (Section 4).
As will be shown in Chapter 4.1.1, in experiments a 300 nm thick polycrystalline thin film consisting of ZnO material on sapphire substrate is used. The ZnO film is formed by crystalline grains with a lateral size of roughly 120-200 nm. The question is how the film provides the feedback needed for laser action.
The thin film geometry with its ZnO-sapphire and ZnO air interface forms in principle an axial Fabry-Pérot resonator [44]. Considering the threshold condition for lasing in Fabry-Pérot like cavities given in Equation 2.11 the threshold gain is one orders of magnitude larger than the gain thresholds observed in ZnO NWs (see Figure 5.8). Thus the formation of an axial Fabry-Pérot cavity is very unlikely due to the high amount of gain needed for the onset of lasing.

Further the formation of a lateral FP cavity is possible. In the case of a column like grown film, the cavity can be formed by a couple of grains which are excited above inversion [45]. That means the cavity length equals the excited spot size and the end mirrors are formed by the grain boundary interfaces [46]. Another possibility to form the FP cavity is a step like modulation of the ZnO material refractive index by the excitation pulse due to the carrier density dependent refractive index form the FP cavity. Simulations of the spatial variations of the refractive index inside the excitation spot showed refractive index variation of 0.2 over a length scale of 4 μm, i.e. 10 times the wavelength. Under this conditions the reflectivity is smaller than 1 % and in this spatial distance the light has to pass more than 20 grain boundaries. Similar considerations have be performed by Tang *et al.* [46], too. Taking that into account it is very unlikely that a lateral FB cavity can be formed by the pump laser modulation of the ZnO material refractive index.

Since feedback from a closed resonator can be excluded in polycrystalline thin films (used in the experiments), mirror less feedback mechanism need to be considered now. A prominent candidate is random lasing [44, 47, 48, 49]. Here, the feedback is formed by multiple folding the optical path via scattering [50, 51]. Between two scattering events the light experiences gain. Therefore the system size L has to be bigger than the transport mean free path $l_t = l_s/(1- < cos(\theta_s) >)$ between two scattering events, given by the the scattering mean free path l_s and the average scattering angle $< cos(\theta_s) >$. The scattering angle can be approximated by 0 and 0.5 in the case of Rayleigh ($\lambda_{ZnO}<l_s$) and Mie scattering ($\lambda_{ZnO} \approx l_s$), respectively. A distinction can be made between a localized and delocalized (diffusive or week scattering) random laser. The difference is defined by the light wavelength inside the material via $l_t<\lambda_{ZnO}<$L (localized) and $\lambda_{ZnO}<l_t<$L (delocalized). Emission features for the localized and delocalized case are narrowband lasing peaks (0.01 to 0.1 nm bandwidth) and a few nanometer broad emission spectra, respectively [52].

It is assumed that in the thin film geometry the amplification happens in the crystalline ZnO grains and the light is scattered at the grain boundaries. Taking the dimensions of the used polycrystalline films the transport mean free path l_t is slightly smaller or equal the same of the emission wavelength inside the ZnO material $\lambda_\mathrm{ZnO} = \lambda/n_\mathrm{r}$=190 nm using 380 nm emission wavelength and n_r=2 refractive index. The system size L is given by the optical pumped spot size, and thus much larger than the λ_ZnO and l_t. This meets the criteria for random lasing, but no clear distinction can be made between localized or delocalized random lasing.

Please note, spontaneous emitted photons can also be amplified if they propagate in an inverted material. This process is well known as amplified spontaneous emission (ASE).

2.2.3 Rate equation model

Simulations of optical pumped laser emission from ZnO are performed by solving the coupled rate equations considering conduction band electrons and emitted photons. In the experiment, the pumping is performed by femtosecond laser pulses in the spectral range from $0.8\,\mu$m to $10\,\mu$m. In ZnO, with a band gap energy of 3.2 eV, this will result in conduction band electrons with excess energy which can result from the multiphoton absorption process and/or free carrier absorption. As shown at this state the electron and hole distribution at large k-values can not be defined exactly. Due to electron-electron scattering appearing in the first hundreds of femtoseconds after the excitation process the electrons (hole) distribution in the conduction band (valence band) is described by the product of the Fermi-Dirac distributed function and the density of states (see Fig. 2.3). The electron distribution is defined by the electron temperature (T_e) which is hotter than the hole temperature (T_h). Both temperatures are much larger than the lattice temperature T_l. The quasi-Fermi levels for electrons (μ_e) and holes (μ_h) are laying inside the bands [53]. After a few picoseconds the electrons and holes thermalize as a result of electron-phonon scattering which transfers energy from the electron and hole system to the lattice. The Fermi-Dirac distribution function is now characterized by quasi-Fermi levels inside the bands. The electron and hole temperature roughly equals but are still hotter than the lattice temperature [54]. These thermalized electrons spontaneously recombine and emit photons. If the conduction band electron density exceeds a threshold density linked to population inversion, amplification instead of reabsorption of the emitted photons take place. Thus, the density of emitted photons is determined by the spontaneous as well as stimulated recombination process and reduced by the photon loss rate [29]. These processes are described by coupled rate equations containing the hot electron density n_e^*, the thermalized electron density n_e, and the photon density s:

$$\frac{\mathrm{d}n_\mathrm{e}^*}{\mathrm{dt}} = a_\mathrm{c} W_\mathrm{K}(\lambda, I(t)) + a_\mathrm{c}\frac{\mathrm{d}n_\mathrm{FCA}}{\mathrm{dt}} - \frac{n_e^*}{\tau_c} \tag{2.12}$$

$$\frac{\mathrm{d}n_\mathrm{e}}{\mathrm{dt}} = \frac{n_\mathrm{e}^*}{\tau_\mathrm{c}} - \frac{n_\mathrm{e}}{\tau_\mathrm{e}} - s g_0 (n_\mathrm{e} - n_0) \tag{2.13}$$

$$\frac{\mathrm{d}s}{\mathrm{dt}} = s g_0 (n_\mathrm{e} - n_0) + \frac{n_\mathrm{e}}{\tau_\mathrm{e}} - \frac{s}{\tau_\mathrm{s}} \tag{2.14}$$

The first term in Equation 2.12 denotes the electron generation rate described by the Keldysh formula $W_\mathrm{K}(\lambda, I(t))$ (Eq. 2.1) while $I(t) = I_0 \exp\left(-4\ln(2)t^2/\tau_\mathrm{FWHM}^2\right)$ is the pump laser intensity and λ is the laser wavelength. Further, free carrier absorption is taken into account as discussed in Section 2.1.2 with the expression for impact excitation given in Equation 2.9. As a result of strong excitation, transition channels become closed (Pauli exclusion principle for fermions) because no empty states are available in the conduction band (see Figure 2.7 b and c). The state blocking leads to a blue shift of absorption edge, also known as Burnstein-Moss-effect and

limits the electron excitation rate [55]. In the rate equation model the Pauli state blocking, i.e. a saturation of the absorption is taken into account via a phenomenological introduced saturation term

$$a_c = \left(1 + \frac{n_e^*}{n_c}\right)^{-1} \tag{2.15}$$

with n_c the saturation carrier density. For simulations n_c was set to $5 \cdot 10^{25}\, m^{-3}$.

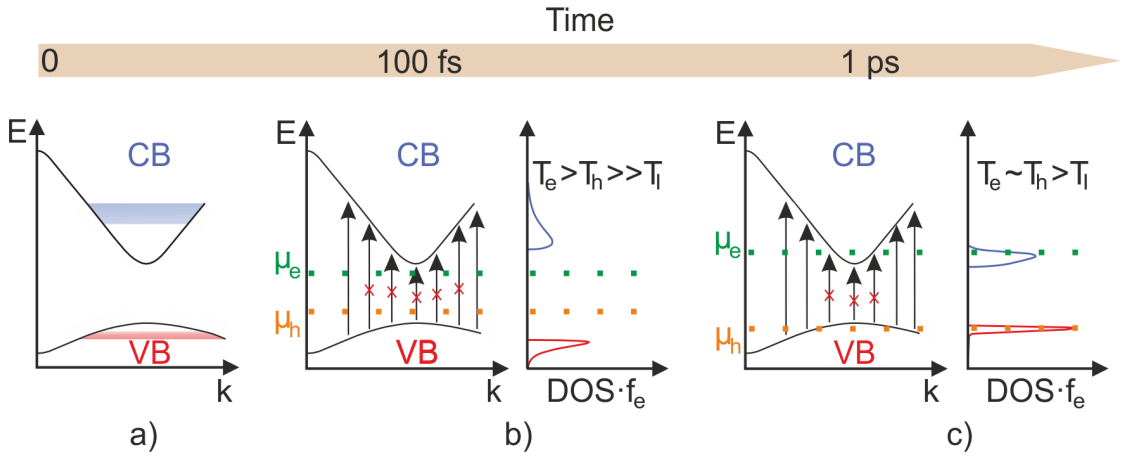

Figure 2.7: Thermalization process subsequent optical exciation semiconductors. a) As a result of interband excitation and subsequent free carrier absorption a certain, not exactly defineable, amount of states in VB and CB is occupied by holes (red area) and electrons (blue area). b) After hundreds of femtosecond the electron distribution will be rearranged via electron-electron scattering and the occupied states can be described by the product of the density of states (DOS) and the Fermi-Dirac function characterized by quasi Fermi levels of the electron and hole system located between bands and a nelectron temperature larger than the hole and both much hoter than the lattice. c) On a timescale of a few picoseconds the hot electron and hole sytem thermalizes via electron-phonon scattering. The Fermi-Dirac function is now described by an equal electron and hole temperature still hotter than the lattice and quasi Fermi levels located inside the bands. The black arrows in b) and c) indicate the available tranistion channels of electrons. Due to state blocking as a result of the Pauli exclusion principle for fermions transitions are closed (red crossing) near the band egdes (adopted from [54]).

The thermalization of the hot electrons, spontaneous recombination, and photon loss is described by a single-exponential decay with the time constants τ_c, τ_e, and τ_{ph} which were set to 1 ps, 100 ps, and 1.4 ps, respectively [37, 41, 56]. The threshold electron density n_0 that must be surpassed to observe gain was set to $2 \cdot 10^{25}\, m^{-3}$ [37, 38, 56]. The gain coefficient $g_0 = 2 \cdot 10^{-12}\,\mathrm{m^3/s}$ was chosen such that the relation $g_0(n_e - n_0) = \frac{c}{n_r} g(\lambda)$, where c denotes the speed of light and n_r the refractive index, is fulfilled with a spectral gain coefficient $g(\lambda)$ of around $2 \cdot 10^5\,\mathrm{m^{-1}}$, which is in the range of reported gain values in the literature [32, 46, 57, 58]. The system of coupled Equations 2.12-2.14 were solved using the Runge-Kutta-4th order method in the time frame from -0.2 to 40 ps using a step size of 2 fs.

Figure 2.8 depicts simulation results using a pump pulse at 3.2 μm with a duration of 100 fs. In Figure 2.8 a the temporal evolution of the pump pulse (upper panel), carrier density (n_e) (middle

panel) and the emitted photon density (lower panel) are shown for pump laser intensities below (green), around (black) and above the threshold intensity (red). The middle panel of Figure 2.8 a shows that in the case of lasing, the carrier density in the conduction band is depopulated until the transparency density n_0 is reached. If lasing sets in, i.e. that the gain is higher than the losses, the emitted photon density shows a fast decaying signal with a duration of a few picoseconds. The simulations show a faster onset of the emission for higher pump intensities. Note, the excitation process which happens on a fs time scale is decoupled from the emission process via the thermalization process (see Figure 2.7). Figure 2.8 a shows the characteristic s-shape of the output (integrated signal) vs. the pump intensity in a log-log-scale. The vertical dashed line highlights the threshold pump intensity I_{th} when lasing sets in.

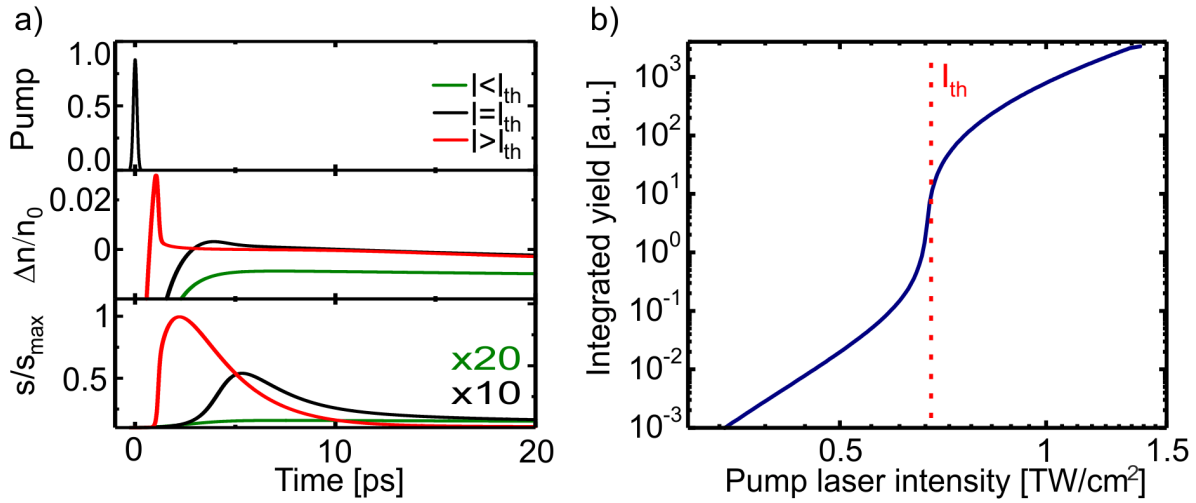

Figure 2.8: Illustration of the temporal emission and carrier dynamics calculated using Equation 2.12 to 2.14. a) Pump pulse (upper panel), excited carrier dynamics normalized to $\Delta n/n_0$ with $\Delta n = n_e - n_0$ (middle panel) and the normalized emitted photon density s (upper panel). b) Temporal integrated yield as a function of the pump pulse intensity at the central wavelength of 3.2 μm. The parameters for the laser model are given in the text.

2.3 High harmonic generation in solids

The nonlinear interaction of an electric field with matter is often linked with the generation of new frequencies, determined by harmonic orders of the fundamental light frequency [6]. In the frame of pertubative nonlinear optics these phenomena can be understood by the power expansion of the polarization field given in Equation A.7. The generation of non-pertubative, higher order harmonics, was observed using gas targets and increasing the pulse intensity so that ionization of the atoms begins [59]. After the first demonstration, HHG has been developed

[6]Note, the optical parametric process is a nonlinear process second order. Here, the new generated photon energies are not linked to harmonic orders.

to a table top laser driven XUV and soft x-ray source over the past decades[7]. Figure 2.9 depicts a typical HHG-spectra obtained by focusing an intense femtosecond near-infrared laser pulse in a gas target [62].
The spectrum can be separated in three parts:

- The low harmonics which decrease rapidly with increasing order can be well described by the pertubative description of the nonlinear interaction given in Equation A.7.
- The pertubative harmonics are followed by a plateau region, characterized by similar harmonic intensities of the orders.
- Highest generated orders are called cut off harmonics.

The HHG process in gases can be described semi-classically by the so-called three-step-model where the atom was described quantum mechanically and the light particle interaction classically. The three steps are [62]:

1. **Ionization:** Due to the strong light field the atom is ionized by multiphoton and/or tunnel ionization.
2. **Free space propagation:** After ionization the electron is considered as a free particle, while the attractive Coulomb potential of the ions is neglected. The free electron is accelerated in the laser field while scattering with other ions and electrons can be neglected if the gas density and ionization rate are low.
3. **Recombination:** Every half cycle the electric field changes its sign. This gives the electron a change to be brought back to the parent ion where it can recombine. The released energy is a sum of the ionization energy and the kinetic energy the electron gained from the field.

From the three step model a simple rule for the cut off photon energy of $h\nu_{co} = I_\mathrm{p} + 3.2U_\mathrm{p}$ appears, with I_p the ionization energy of the electron and U_p (see Equation 2.6) the pondermotive energy.
After the discovery of HHG in gases scientists desired to observe HHG in solids where a higher harmonic yield is expected due to a higher electron density of the material. Due to low damage threshold of condensed matter first attempts demonstrated the generation of high (up to 7th order), but still only pertubative harmonic orders [63]. The first demonstration of non-pertubative HHG from a femtosecond mid-IR laser in a solid ZnO crystal was published by Ghimire *et al.* [17] in 2010. The problem of the low damage threshold but required field strength was circumvented by applying strong mid-IR fields on wide band gap semiconductor material

[7]The spectral region which can be reached by HHG critically depends on the laser wavelength. Thus using near and mid-infrared driver wavelength gas-phase HHG up to 300 eV[60] and 1.6 keV [61] were demonstrated, respectively.

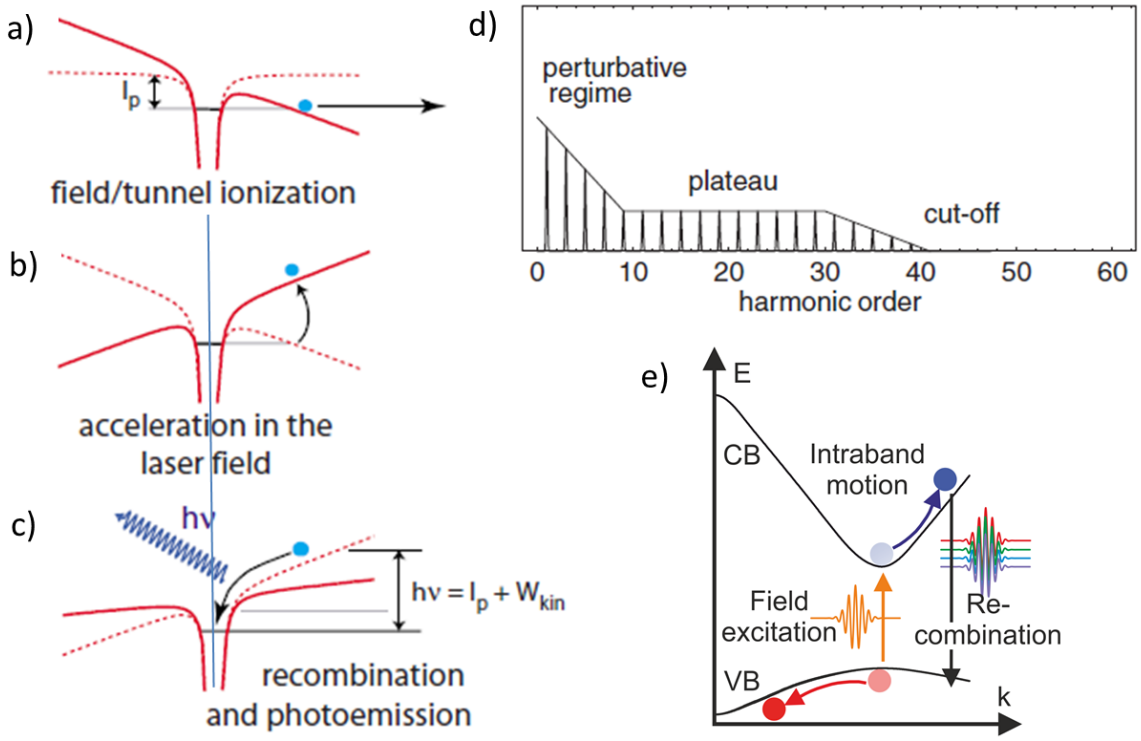

Figure 2.9: a)-c) Semiclassical three step model of HHG in gases. The strong light field of the laser pulse perturbes the binding potential of the atom leading to tunneling ionization of an electron. The quasi free electron is accelerated in electric field of the laser pulse. The change of the laser field sign may bring back the electron to its parent ion and recombination can take place. The emitted photon energy is given by the sum of the atom ionization energy and the kinetic energy the electron gained in the laser field. These processes repeat every half cycle of the laser pulse, as a result a periodic harmonic comb is generated with the frequencies defined by the harmonic orders of the fundamental laser field (adopted from [62]). d) HHG emission spectra. First, rapidly with the decreasing, harmonic orders (pertubative harmonic orders) can be explained by the power series expansion of the polarization field in frame of the pertubative nonlinear optics discussed on page 121. The following harmonic orders are characterized by a constant harmonic intensity form the plateau in the spectrum. The end of the harmonic frequency comb is formed by the cut off harmonics. (adopted from [62]) e) Schematic illustration of the assumed mechanism resposible for HHG in solids. After field excitation of an electron from the VB to the CB the electron is accelerated in the CB resulting in a nonlinear intraband current. Further the high kinetic electron in the CB and hole in VB can recombine creating a interband polarization field. The HHG emission is given by the sum of the intra- and interband contribution.

(ZnO). Performing HHG in solids further allowed to use functunalized nanostructures and/or material modifications to optimize, control and/or enhance the HHG signal [64, 65, 66, 67].
So far no unified model exists to describe HHG in a solid crystal. One reason is the more complex electronic (band) structure of condensed matter compared to the discrete energy levels of an atom. While in the atomic case the electron can be considered as a quasi free particle and for low gas pressures electron scattering processes are neglectable, in a crystalline solid the excited electron in the conduction band is still bound to the lattice ions and high electron densities results in rapid dephasing by electron-electron scattering. To understand the underlying physical mechanism of HHG in solids is still topic of active research [68]. The most widely accepted

understanding is that after field excitation the quasi free electron in the conduction band will be accelerated by the electric field of the laser pulse (analogous to the situation described in Section 2.1.2) which results in a coherent nonlinear intraband current (see Fig. 2.9 e). Additional to this intraband movement the accelerated electron in the conduction band with a quasi momentum k≠ 0 can recombine with a hole in the valence band leading to a nonlinear interband polarization field. The detected high harmonic signal is given by the Fourier transformation of the sum of the intraband and interband contribution. The spectral emission characteristics of HHG from gases and solids are very similar and the same three parts, discussed above, can be identified [69, 70].
As reviewed by Ghimire *et al.* [68] there is a clear relation between the material band gap, wavelength of the driving pulse and the measured cut off energy. Thus short wavelength drivers in the NIR spectral range efficiently generate high harmonics in dielectric materials and show a cut off at high energies around 20-50 eV. Compared to mid-IR and THz pulses which show HHG preferentially in wide and small bandgap semiconductors, linked with low energetic cut off energies at roughly 10 and 2-5 eV, respectively. Using ZnO material, efficient HHG was demonstrated from femtosecond pulses in the spectral range from 3-4 μm [17, 71].

2.4 Conclusion

In this Chapter the basic knowledge about off-resonance strong light field matter interaction was introduced.
Photo-excitation of electrons in semiconductors appears, dependent on the band gap to photon energy ratio and light intensity in the regime of single/multiphoton absorption or tunneling. A decision which effect dominates can be made on the basis of the Keldysh parameter γ. Another excitation channel is given by electron-electron (impact) excitation upon intraband free carrier absorption. This energy transfer from light wave to the free electrons scales beneficial towards long wavelengths were tunneling is the dominant excitation mechanism. To avoid irreversible damage due to an avalanche excitation process upon carrier heating, ultrashort laser pulses are necessary.
The concept of optically pumped lasing in semiconductor nanostructures made from the wide band gap material ZnO was introduced. Lasing can be achieved, if the excited carrier density exceeds the lasing threshold, i.e. the semiconductor material provides gain and the sample morphology provides the required signal feedback. Two nano laser types, namely the FP cavity formed by ZnO NWs and ASE together with random lasing in ZnO thin films were discussed.
Furthermore, the HHG process in condensed matter was introduced. Applying intense mid-IR laser light on ZnO, electrons are dominantly excited by the tunneling process. The free electrons experience a large shift of their momentum due to the strong electromagnetic field. As a result

a coherent nonlinear intraband currents and in the case of coherent electron-hole recombination interband polarization fields are formed. Due to the temporal repetition of these processes at every half cycle of the laser pulse harmonic orders of the driving laser field are generated. Special attention was paid to femtosecond laser pulses in the near to far-IR spectral range (see Appendix A) and ZnO semiconductor material because these were applied in experiments which will be presented in the following chapters.

Chapter 3

High harmonic generation in crystalline ZnO

The previous chapter introduced the fundamentals of far off-resonance interaction of femtosecond laser pulses with ZnO. The direct semiconductor ZnO has a band gap of 3.2 eV at room temperature. In the experiments outlined here, ZnO samples were irradiation with mid-IR light at 3.2 μm central wavelength. This corresponds to a photon energy of 0.39 eV and thus a band gap to photon energy ratio of 9. Consequently, for this wavelength the ZnO is highly transparent from a classical point of view. As discussed in Section 2.1.3, using ultrashort laser pulses reaching TW/cm^2 intensities what corresponds to V/Å electric field strengths, strong interband excitations due to Zener-tunneling can be induced [5, 19]. Here, the field of the laser pulse perturbs the electronic system that electrons can tunnel from the valence band (VB) to the conduction band (CB) what finally may result in a high excited carrier population. The free electrons in the CB gain kinetic energy from the laser field due to the classical Coulomb force that the laser field affects on the electrons. Considering the scaling law of this intraband process, the kinetic energy which can be transferred to the electrons is given by the pondermotive energy $U_\mathrm{p} \propto I_0\lambda^2$. Thus, the electron acceleration in the conduction band benefits from long wavelength drivers (see Section 2.1.2 for more details). The field driven electrons on the one side can excite other electrons via impact ionization or in case of scatterless propagation it can generate higher order harmonic emission via a nonlinear intraband current or interband polarization fields in the case of electron-hole recombination (see Section 2.3 for more details).

A successful implementation of light wave driven petahertz electronics relies on a detailed understanding of the material modifications upon strong carrier excitation. In this thesis HHG in highly excited semiconductors is used to study the effects of a high CB population on the nonlinear carrier dynamics. In Section 3.1.1 results on the effect of the high carrier density on the HHG process are presented. The laser intensity and thus excited carrier density dependent emis-

sion spectra reveal a strong blueshift of the generated harmonics. Furthermore, a pump-probe method was applied to shed light on the HHG dynamics caused by the field excited carriers leading to a strong out of equilibrium state of the ZnO. In Section 3.1.2 results are presented that show how ZnO is perturbed by a 3.2 μm pump pulse and probed in a noncollinear geometry by time delayed 3.2 μm pulse generating high harmonics in the carrier doped material. The results reveal that dependent on the carrier density excited by the pump pulse the HHG signal is reduced. Furthermore, the non-equilibrium state of the ZnO matter displace lattice ions due to interatomic forces resulting in coherent phonon excitation. The coherent and harmonic oscillation of the lattice is traced by high harmonic generation of the time delayed probe pulse.
In the previous section it was shown that the use of ultrashort pulses, ideally only a few cycles long, enables to apply high field strength while avoiding avalanche excitation. A beamtime at the Extreme Light Infrastructure for Attosecond Laser Physics Science (ELI-ALPS) in Szeged, Hungary enabled experiments with few-cycle (2.4-cycle) and carrier-envelope-phase (CEP) controllable mid-IR (3.2 μm) laser pulses with a high pulse repetition rate of 100 kHz. The CEP describes the phase offset between the envelope and the oscillating part of the electric field (see Figure A.1) and becomes important, when the duration of the pulse is reduced to only a few cycles of the electric field. Using this world wide unique laser system (see Appendix C) the dependence of the high harmonic emission on the CEP was investigated and a simple but very efficient method to measure the relative CEP using HHG in solids was developed.
Results of this section were published in Ref. [72] and [73].

3.1 High harmonic generation in highly excited semiconductors

In this section high harmonic generation (HHG) in crystalline bulk ZnO from femtosecond 3.2 μm mid-IR laser pulses is investigated. As discussed in Section 2.3, the HHG process in condensed matter is much more complex compared to HHG in gaseous media. The intrinsic properties of condensed matter, under equilibrium conditions, already increase the complexity of the strong field matter interaction process dramatically, which prevents a detailed microscopic understanding of the HHG mechanism so far. The situation becomes even more difficult considering a highly excited semiconductor, far out of its equilibrium state, as a result of strong field excitation. As discussed in Section 2.1.3, a high number of electrons are excited by a femtosecond laser pulse even in the case of far off-resonance interaction, i.e. for a band gap to photon energy ratio much bigger than one. This involves transient changes of the optical properties of the material due to modifications of the electronic as well as crystalline structure of the material. In Section 3.1.1 results on HHG in a 100 μm thick sheet of bulk ZnO are presented as a function of the free carrier density. Furthermore, a pump-probe experiment was used to

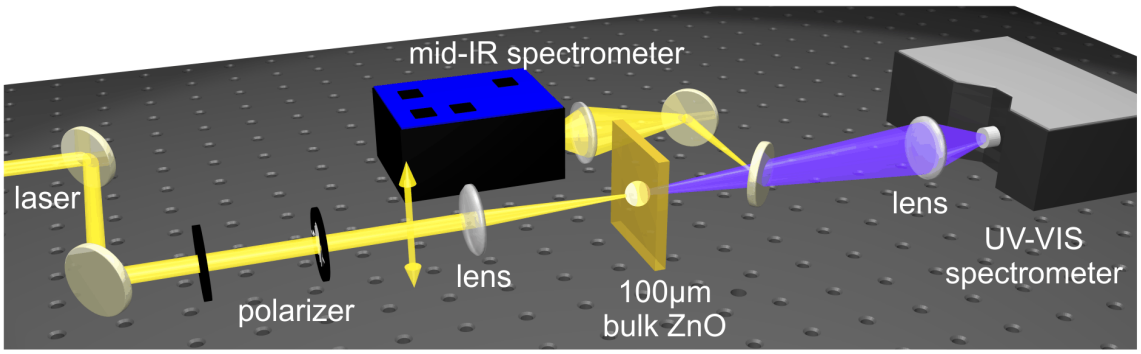

Figure 3.1: Experimental setup used to study the dependence of HHG on the laser intensity. The mid-IR laser power is attenuated by a pair of wire grid polarizers. The linear polarized laser is focused, using a f=10 cm CaF_2 lens, to a focal spot size of 65 μm in the plan where the 100 μm thick ZnO sample was placed. The high harmonic emission from the sample and the transmitted mid-IR fundamental was detected with a UV-VIS spectrometer and a mid-IR spectrometer, respectively.

investigate the transient effects of the out of equilibrium state of the ZnO on the HHG process (Section 3.1.2).

3.1.1 Carrier density dependent HHG in solids

The carrier density dependence of HHG in solids was investigated using 3.2 μm laser pulses with roughly 100 fs duration, 1 kHz repetition rate and up to 80 μJ pulse energies, which were generated by non-collinear DFG between the signal and idler beam from a BBO based OPA (more details see Page 125). Figure 3.1 illustrates the used experimental setup. The laser pulse energy was adjusted using a pair of wire grid polarizers before the laser was focused normal onto the 100 μm thick sheet of c-cut ZnO bulk material to a spot size radius of 130 μm using a f=10 cm CaF_2 lens. The high harmonic radiation was collected and refocused into a UV-VIS spectrometer (USB4000, Ocean Optics) using a f=5 cm CaF_2 lens. The fundamental laser spectrum was measured, after the laser beam propagated through the ZnO material, using a broadband mid-IR spectrum analyser based on an acoustic optical modulator (Mozza, Fastlite). The pulse duration and spot size at the sample position were characterized by a SH-FROG and knife-edge technique as exemplary illustrated in Figure 4.2 c,d and Figure 4.3 in Section 4.1.2, respectively. The laser intensities were calculated out of the measured pulse energy, duration and laser spot size in the plane of the sample using Equation A.5. To obtain the laser intensity inside the ZnO, the reflection losses (R(3.2 μm)=0.1)[8]) from the air-ZnO surface were taken into account. The excited carrier density was estimated as function of the laser intensity using the Keldysh-Drudel model (Equation 2.9), which considers inter- as well as intraband absorption processes.

Figure 3.2 a depicts the high harmonic emission as a function of the laser intensity. With in-

[8]The value was taken from the online refractive index database: https://refractiveindex.info/.

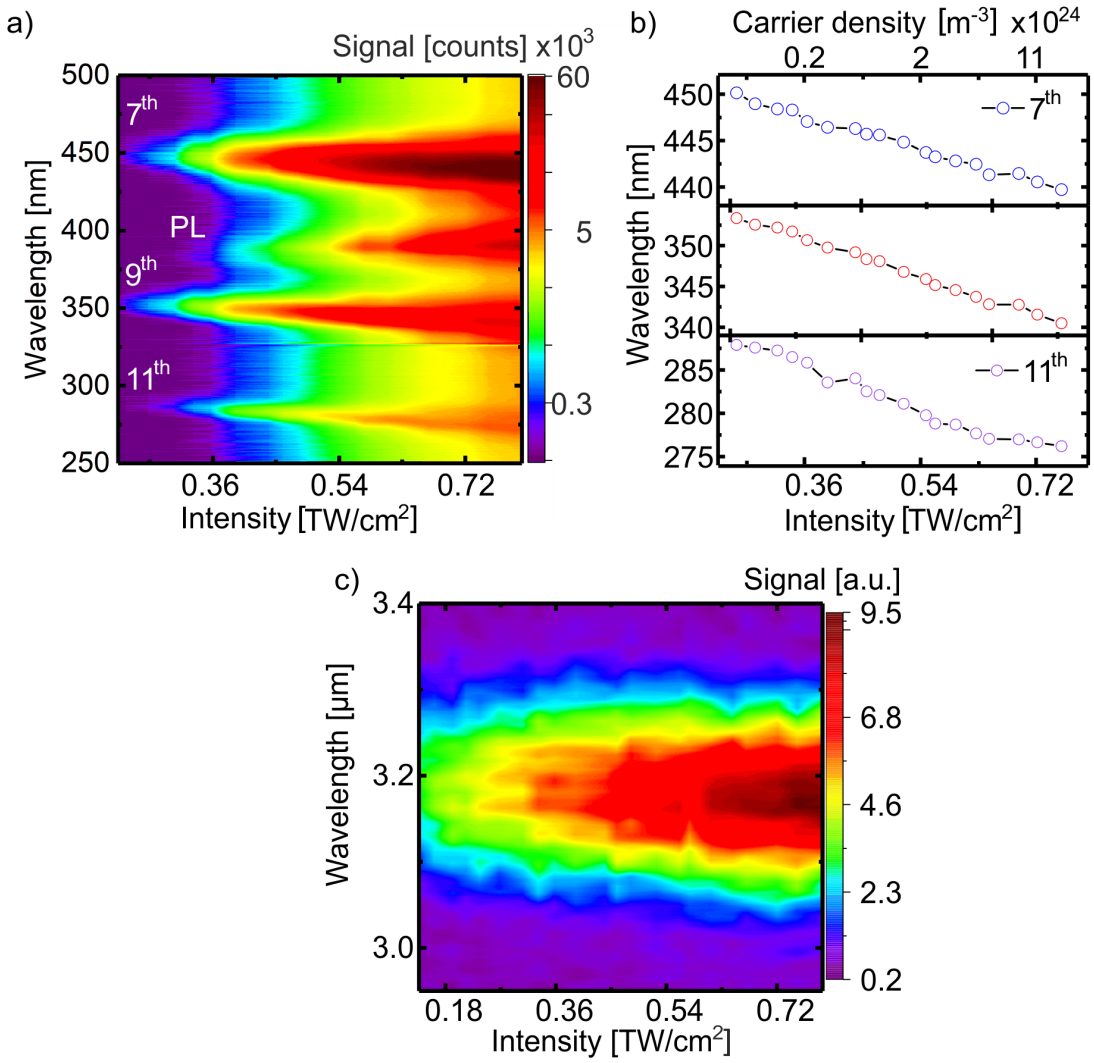

Figure 3.2: a) Emission spectra from a 100 μm thick sheet of bulk ZnO irradiated with a mid-IR femtosecond laser pulse at 3.2 μm as a function of the laser pulse intensity. High harmonic orders 7th, 9th, 11th and the photoluminescence (PL) at 390 nm are shown. b) Spectral evolution of the center of mass of the differnt harmonic orders as a function of the laser pulse intensity. All observed harmonic orders clearly shift to shorter wavelengths for increasing laser pulse intensity. c) Spectral evolution of the fundamental mid-IR laser spectrum as a function of the laser intensity, measured after propagation through the 100 μm thick ZnO sample.

creasing laser intensity the harmonic signal of the detected 7th, 9th and 11th order increases and the spectral center of mass for the different high harmonic orders shift to shorter wavelengths (blueshift). Furthermore, the photoluminescence due to band-to-band recombination was observed at roughly 390 nm wavelength. Due to the inversion symmetric arrangement of the electric field to the material c-axis no even order harmonics are detected [71]. The harmonic spectra were fitted using a sum of Gaussian functions to obtain the harmonic signal (amplitude) and the spectral position of the maximum. Figure 3.2 b shows the spectral position of the maximum for the different harmonic orders as a function of the laser intensity. The 7th, 9th and 11th harmonic

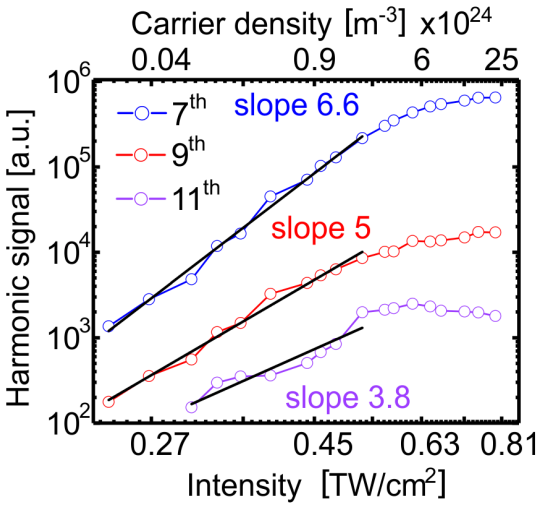

Figure 3.3: Harmonic emission signal as a function of the laser pulse intensity. The deviation of the slopes from the expected pertubative orders (7, 9, 11) indicates the non-pertubative nature of the HHG emission.

order experience a shift from 450 to 440 nm, from 353 to 340 nm and from 288 to 276 nm, respectively. Consequently, a laser intensity increase by a factor 4.5 results in a roughly 10 nm spectral shift. The excited carrier densities increased by two orders of magnitude from roughly 0.1 to $11 \cdot 10^{24}\,\mathrm{m}^{-3}$ (see on top of Figure 3.2 b). To investigate the origin of the blue shift of the harmonic spectra the fundamental mid-IR laser spectrum was measured as function of the laser intensity after the laser pulse propagated through the ZnO sample (see Figure 3.2 c). The measurements revealed, that the fundamental laser spectrum is insensitive to the propagation through the highly excited semiconductor material.

Werner *et al.* [74] performed similar experiments using the semiconductor ZnSe (E_g=2.6 eV) irradiated by femtosecond laser pulses at 3.4 and 3.8 μm, respectively. Blue shifted harmonics up to the 7th order have been observed. Using laser pulses at 3.4 μm and 3.8 μm a laser intensity increase by a factor 7 and 8 resulted in a 33 nm and 48 nm shift of the 3th harmonic emission spectrum, respectively. In the work of Werner *et al.* [74] the fundamental spectrum experience a laser intensity dependent redshift by 5 nm, which is neglectable compared to the large spectral shift of the harmonics. Based on space- and time-resolved simulations[9] the authors mediate the observed blue shift of the harmonic emission spectrum to the high free carrier density. This conclusion is supported by the calculated excited carrier densities presented in this thesis. A electron density up to $2 \cdot 10^{25}\,\mathrm{m}^{-3}$ is reached in ZnO for highest applied laser intensity.

Figure 3.3 depicts the harmonic emission signal (given by the fit amplitude) as a function of the laser intensity. The power scaling law of the harmonic emission clearly deviates from the pertubative scaling law, suggesting the non-pertubative nature of the generation mechanism [75]. For high laser pulse intensities of 0.5 $\mathrm{TW/cm}^2$ the generation of harmonic signal saturates. It is assumed that the saturation of the HHG is linked to state blocking and thus a decreasing excitation rate [54]. The power laws of the individual measured harmonics are much lower than

[9] No further details about the simulation are given in the work of Werner *et al.* [74].

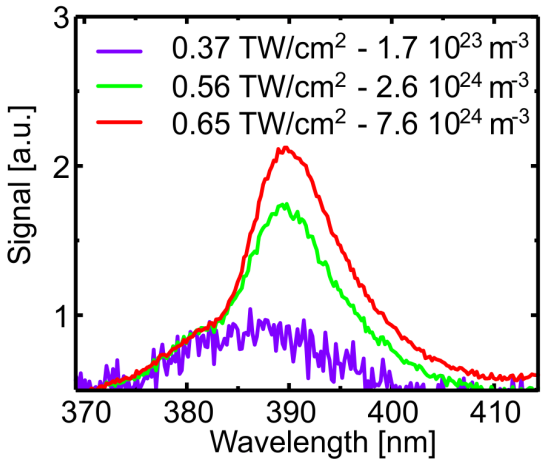

Figure 3.4: Photoluminescence emission as a function of the mid-IR laser and corresponding excited electron density. For a carrier density of $1 \cdot 10^{24}$ m^{-3} a second emission band appears. In this excitation regime a transition to an electron hole plasma (Mott-transition) is predicted.

reported values in literature [17]. The dependence of the harmonic generation process on the laser intensity is still part of active research and no universal intensity dependence (power scaling law) was discovered so far.

For ZnO a transition of the electronic system from an excitonic to a correlated electron system (electron-hole-plasma (EHP)), also known as Mott-transition, is predicted for carrier densities around $1 \cdot 10^{24}$ m^{-3} [32]. Figure 3.4 depicts the photoluminescence emission spectra as a function of the laser intensity. Applying an intensity of 0.37 TW/cm^2, which corresponds to an excited carrier density of $1.7 \cdot 10^{23}$ m^{-3} regarding calculations using Equation 2.9 a broad emission band centered around 387 nm is detected. A second narrow and stronger emission band at 390 nm is appearing when the laser intensity was increased to 0.56 TW/cm^2. At this intensity a carrier density around $2.6 \cdot 10^{24}$ m^{-3} is excited from the VB to the CB. Thus the additional emission band appears for a carrier density where the Mott transition is expected. The conformity of the calculated Mott density with the occurrence of the EHP emission band confirms the use of the Drude-Keldysh model. Further increasing the laser intensity results in a weak spectral broadening and redshift, in agreement with emission features of an EHP and bandgap renormalization in highly excited semiconductor ZnO, respectively [32].

3.1.2 Coherent optical phonons traced via HHG

As shown in the previous part a high number of carriers is excited in a 100 μm thick slab of bulk ZnO by a 100 fs laser pulse at 3.2 μm. The high number of excited electrons cause dynamical changes of the ZnO material which is far out of the equilibrium state after the strong field excitation process. A pump-probe setup was used to investigate dynamical effect of the highly excited system on the HHG process. The same laser system has been used as described in the previous section. As shown in Figure 3.5 the laser was split in a pump and probe arm using a 45:55 beamsplitter. The energy and the polarization of the pump and the probe beam

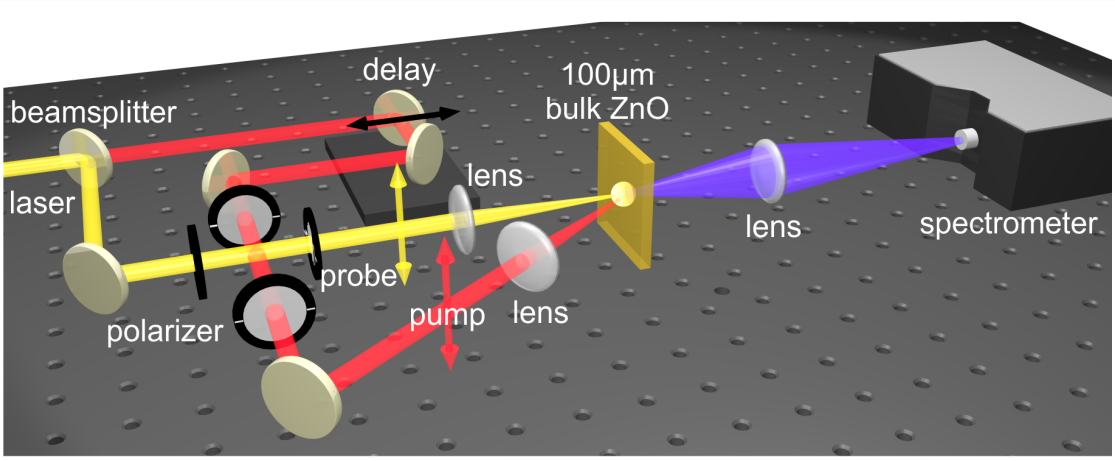

Figure 3.5: Schematic illustration of the pump-probe setup used to investigate the dynamics of highly excited semiconductors on HHG in ZnO. Using a beamsplitter the laser was seperated in a pump and a probe beam whose pulse energies were seperatly adjusted by a pair of wire grid polarizers. The probe beam was focused normal to the surface of a c-cut ZnO crystal using a f=10 cm CaF_2 lens aiming to generate high harmonics which are detected by a UV-VIS spectrometer. The pump beam, used to bring the ZnO matter out of the equilibrium state was focused by a f=10 cm concave silver mirror under an angle of roughly 10° to the surface normal. The time delay between the pump and probe pulse was adjusted by a motorized delay line.

was adjusted independently using pairs of wire grid polarizers. The probe and pump beams are separately focused under an angle of roughly 10° using a f=10 cm CaF_2 lens and a f=10 cm concave silver mirror, respectively, to a radius of 75 μm on the surface of a c-plane oriented 100 μm thick single crystalline ZnO slab. The temporal delay between pump and probe pulses was set by a motorized delay line with a minimum step size of 3 nm and full travel range of 15 cm. The spatial overlap of the pump and probe beam at the sample position was monitored using an imaging system formed by a CCD camera and a microscope objective (not shown). The spectral intensities of harmonics, generated in the bulk ZnO by the probe pulse, were measured by a UV-VIS spectrometer (Ocean Optics, USB 4000). All experiments were carried out at room temperature and ambient atmosphere. The intensities inside the ZnO material were calculated using the measured pulse energy, duration and laser spot size in the plane of the sample by Equation A.5, taking into account the reflection losses (R(3.2 μm)=0.1)[10]) from the ZnO surface.

The colour plot in Figure 3.6 a depicts the measured emission spectra containing the photoluminescence (PL) and the 5^{th}, 7^{th} and 9^{th} harmonic as a function of the pump-probe delay. For positive time delays the probe pulse, generating the detected harmonics, arrives before the pump pulse. Thus the harmonic emission is generated in an unperturbed material. At zero time delay the pump and probe pulse overlap in time. In this case harmonic generation vanishes and at the same time the PL emission is strongly enhanced. Its assumed, that the strong PL and lowered HHG signal results from higher number of excited electrons from constructive interfering

[10]The value was taken from the online refractive index database: https://refractiveindex.info/.

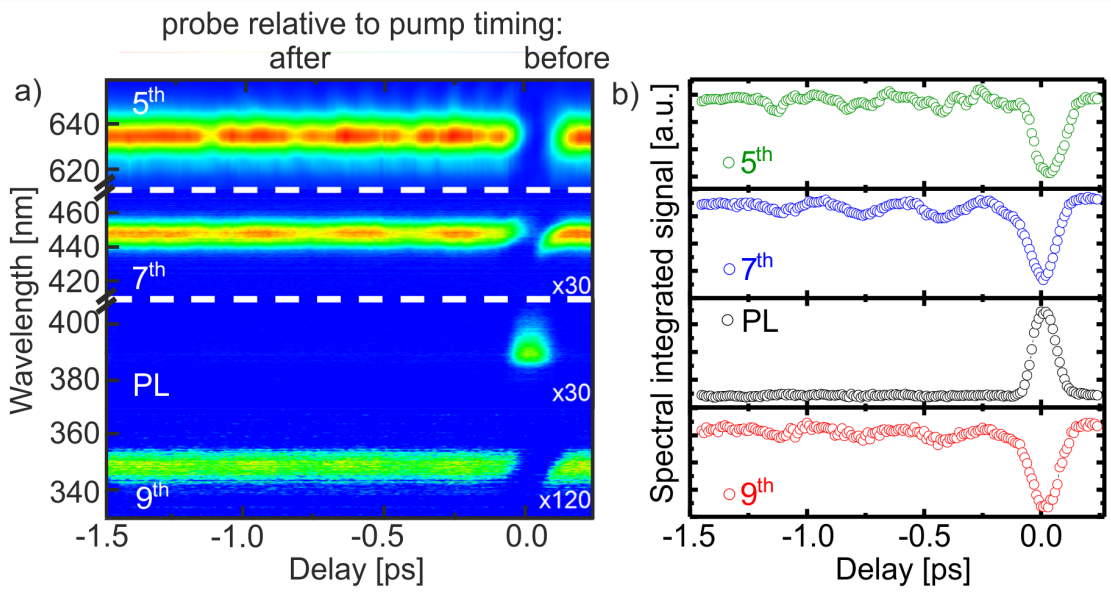

Figure 3.6: High harmonic signal as a function of pump-probe delay. a) Measured 5th, 7th and 9th harmonic as well as photoluminescence (PL) spectra as a function of the pump-probe delay. Positive time delays cover the situation of a probe pulse-matter-interaction in unperturbed material because the pump pulse arrives later. At time delay zero the pump and probe pulse arrive at the same time which lead to vanishing HHG and a very strong PL. The increased PL signal was used to calibrate the delay timing. For negative time delays, i.e. the pump pulse arrives before the probe pulse the high harmonics of the probe pulse are generated in ZnO out of the equillibrium state. Dependent on the time delay the harmonic signal shows a modulated structure whicht ends after roughly 1 ps. b) Spectral integrated signal of the 5th, 7th and 9th harmonic as well as the photoluminescence (PL) as a function of the time delay between the probe and pump pulse. No harmonic signal is detected for zero time delay, for negative delays the all harmonics show a modulation with a oscillation period of roughly 300 fs, only the 5th harmonic is additionally modulated with a high frequency signal. The PL shows a symmetric signal around zero delay and disappears otherwise.

pulses and disturbed electron coherence due to electron scattering, respectively. The strong PL signal was used to calibrate the time axis. For negative time delays, the probe pulse arrives after the pump pulse on the ZnO sample, i.e. the probe pulse generates harmonics in an already excited ZnO material. In this case the signal of each harmonic order is periodically modulated as a function of the pump-probe delay, while the modulations stop at a pump-probe delay of 1 ps. Figure 3.6 b shows the spectrally integrated signal of the different harmonic orders and the PL as a function of the pump-probe delay. Note, the harmonics clearly experience modulations while the PL signal level keeps constant. While the 7th and 9th harmonic clearly show the same modulation frequency, the 5th harmonic is modulated by a fast and slow oscillating signal. The modulation is symmetric around the signal level which was detected for positive time delays (HHG in unperturbed material), i.e. the modulation of the transient high harmonic signal leads not only to a signal reduction but also to an increase. The origin of the oscillation frequencies were revealed by performing a fast Fourier transformation (FFT) analysis of the oscillating part (see Figure 3.7). Therefore, the data are multiplied by a super-Gaussian function to isolate the oscillating part. Before calculating the FFT, the data are centered at zero and zero padding was

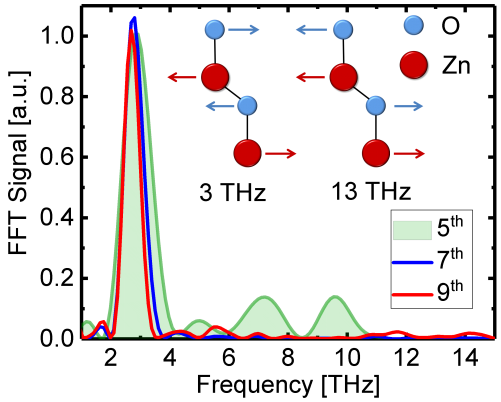

Figure 3.7: Fourier transformation of the data shown in Figure 3.6 b. All harmonics are modulated with an oscillating frequency of roughly 3 THz, only the 5th (filled green area) harmonic is additionally modulated with a signals at 7 and 10 THz. For ZnO two transversal optical phonon modes E_2^{low} and E_2^{high} with the eigenfrequencies 3 and 13 THz are known. The modulation at 7 and 10 THz are asigned to hybride modes E_2^{high} - E_2^{low} and E_2^{high} - $2 \cdot E_2^{low}$, respectively. The lattice displacement of the unit cell basis atoms under E_2^{low} and E_2^{high} phonon oscillation is shown in the inset.

applied to obtain a higher spectral resolution. The Fourier analysis, shown in Figure 3.7, reveals a modulation frequency of 3 THz for all detected harmonic orders. Tthe fifth harmonic is additionally modulated by a roughly 7 and 10 THz signal.

The oscillation frequency of 3 THz overlaps with the transversal optical E_2^{low} phonon mode in ZnO [76, 77]. Furthermore, a E_2^{high} mode at roughly 13 THz and a hybrid mode E_2^{high}- E_2^{low} at 10 THz were identified in ZnO using Raman [76, 77, 78] and neutron scattering methods. The lattice displacement of the Zn and O atoms in the crystal unit cell as a result of the E_2^{low} and E_2^{high} oscillation mode are shown in the insets of Figure 3.7. The excitation of coherent opitcal phonons in condensed matter, especially ZnO, was already demonstrated and studied by probing the transient changes of linear optical properties, like absorption [79, 80] and reflection [81]. Coherent optical phonon modes E_2^{low} [79, 80, 81], E_2^{high} [79, 81] as well as the hybrid mode E_2^{high}- E_2^{low} [81] were indirectly excited by near resonant excitation using 3.1 eV photons [81] and below band gap photons with an energy of 1.5 eV [79, 80]. The identified coherent phonon modes E_2^{low} and E_2^{high} were detected with frequencies at roughly 3±0.1 THz [79, 80, 81] and 13±0.3 THz [81], respectively. The impulsive excited coherent hybrid mode E_2^{high}- E_2^{low} was detected at a frequency of 9.7±0.3 THz [81]. Furthermore, the Raman tensor, defining the symmetry properties of the phonon modes were determined using Raman scattering techniques for different orientations of the symmetry c-axis of the ZnO crystal and are in full agreement with group theory calculations [76, 77, 78, 79]. Thus, it is assumed that the 3, 7 and 10 THz modulation, observed in this work, result from lattice oscillations belonging to the E_2^{low}, E_2^{high}- $2 \cdot E_2^{low}$ and E_2^{high}- E_2^{low} phonon mode, respectively. Please note, the E_2^{high}- $2 \cdot E_2^{low}$ phonon mode wasn't reported in ZnO so far. A roughly 7 THz phonon mode in ZnO was assumed in a nonlinear phonon up-conversion process to explain the temperature dependence of the E_2^{low} phonon mode lifetime [80]. However, the nature of the 7 THz signal is not fully understood, yet.

Assuming an impulsive coherent excitation mechanism [82], the E_2^{high} was not detected because the shortest used pulse duration (75 fs) was equal to the oscillation time of the E_2^{high} mode.

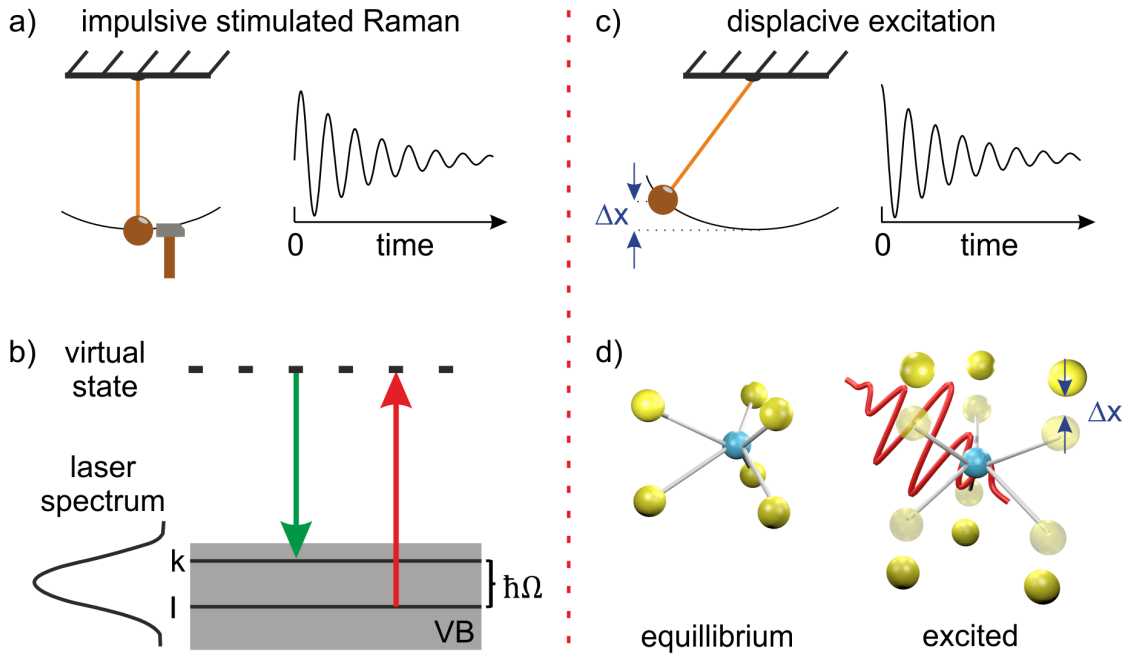

Figure 3.8: Comparision of indirect excitation mechanism of coherent phonons. Left: a) and b) impulsive stimulated Raman scattering (ISRS) . Right: c) and d) displacive excitation of phonons (DECP). For ISRS the lattice is in eqillibrium position and the phonon excitation happens via inelastic scattering of an electron with a lattice oscillation characterized by $\hbar\Omega$. Therefore the electron is excited by a photon with sub-bandgap energy to a virtual state (b). The lattice movement starts from zero with a delta peak (laser pulse) like external force and undergoes a damped oscillation (a). In DECP an ultrashort laser pulse brings the matter out of its equillibrium state by exciting electrons from its ground to unbound states. The lattice ions, will adopt to the new electronic structure due to inter atomic forces. As a result phonon modes are excited and the lattice will do an oscillatory movement. Because the lattice oscillations starts from the out of equillibrium situation the phase of DECP processes is $\pi/2$ phase shiftet in respect to the ISRS mchanism.

In order to verify, if the observed lattice oscillations were excited by an impulsive mechanism, the dependence of the oscillation frequencies on the pump pulse duration was investigated. Figure 3.9 depicts the Fourier analysis of the modulations in the 5$^{\text{th}}$ harmonic signal for the two excitation pulse durations of 75 and 116 fs. The fast oscillations at 7 and 10 THz are only present when the pump pulse is short. Considering the oscillation periods of 333, 143 and 100 fs of the E_2^{low}, E_2^{high}-2 $\cdot$ E_2^{low} and E_2^{high}-E_2^{low} phonon modes at 3, 7 and 10 THz, respectively, this findings are in agreement with an impulsive phonon excitation mechanism picture where the phonon mode amplitude

$$Q \propto \exp\left(-\frac{\tau_{\text{FWHM}}^2}{\tau_{\text{phonon}}^2}\right) \tag{3.1}$$

scales inverse exponentially with the quadratic ratio of the laser pulse duration τ_{FWHM} and the phonon oscillation period τ_{phonon} [83].

The question rises, how off-resonance mid-IR pump pulse can excite impulsive coherent optical

phonons in ZnO.
The E_2^{low} and E_2^{high} modes are Raman active phonon modes [77]. A direct excitation of the lattice oscillation by the 3.2 μm (94 THz) pump pulse can be excluded [84]. In past decades two indirect excitation mechanism of coherent optical phonons namely impulsive stimulated Raman scattering (ISRS) and the displaceive excitation of coherent phonons (DECP) mechanism were intensively discussed (see Figure 3.8). The ISRS mechanism is based on the Raman process, i.e. an electron is excited from its ground state to a virtual state where it scatters with a phonon which carries an energy of $\hbar\Omega$. The recombining electron occupies a state with an energy lowered in correspondence to the phonon oscillation energy $\hbar\Omega$ (Figure 3.8 b). In this case the ultrashort laser pulse acts as a delta peak like external force which "kicks" the lattice ions out of its equilibrium position (see Figure 3.8 a). The subsequent lattice motion can be described by a damped harmonic oscillator. The DECP mechanism relies on the excitation of bound electrons to high energetic states which bring the matter out of its equilibrium condition. As a result of the impulsive and strong excitation, electrons occupy higher lying orbitals. Due to interatomic forces this leads to a readjustment of the lattice ions (Figure 3.8 d). As illustrated in Figure 3.8 c, in the case of DECP the lattice oscillation starts from the maximum lattice displacement since the electronic excitation and readjustment of the lattice structure happens on a much faster time scale than the lattice can react. Similar to ISRS, the lattice displacement will undergo a damped harmonic oscillation. Historically DECP and ISRS had been considered as independent mechanisms and due to electron excitations to real and virtual electronic states the DECP and ISRS model have been linked to opaque and transparent materials, respectively. It has been shown that the DECP description is compatible with the Raman based interaction when the complex Raman tensor is considered [82, 85, 86]. In both descriptions of coherent optical phonon excitation processes, laser pulses shorter than the oscillation period of the phonon mode or, as shown in Figure 3.8 a, a laser pulse spectrum broader than the phonon mode eigenfrequency (Ω) are required [82].
Distinguishing between ISRS and DECP can be made by the pump laser scaling of the transient modulation. In the case of the ISRS excitation mechanism the modulation amplitude increases linear with the excitation laser intensity [79]. Figure 3.10 a depicts the modulation amplitude in the 5^{th} (green), 7^{th} (blue) and 9^{th} (red) harmonic signal determined by a Fourier analysis as a function of the pump pulse intensity and for a fixed probe pulse intensity of 0.3 TW/cm^2. For pump intensities below 0.36 TW/cm^2 the modulation amplitude follows a power scaling (slope) of 1.7, highlighted by the black line in Figure 3.10 a. The power law of the modulation amplitude (Figure 3.10 a) is identical for all detected harmonic orders. Furthermore, the pump pulse intensity scaling dependence linearly on the applied probe pulse intensity, as shown in Figure 3.10 b. The pump pulse scaling exponent increased from 1.25 to 2.2 when the probe pulse was increased from 0.13 to 0.42 TW/cm^2. The deviation of an linear intensity dependence

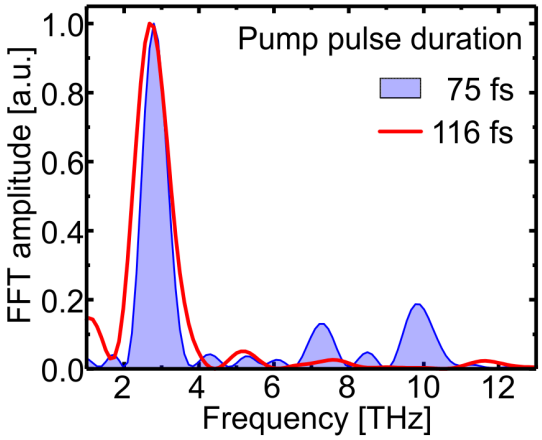

Figure 3.9: Oscillation frequencies as a function of the pump pulse duration. Measurments were performed with 75 (blue filled area) and 116 fs (red line) pump pulses. Using the short pulse the high harmonic signal is modulated with a 3, 7 and 10 THz signal. In case of a 116 fs long pump pulse the harmonic signal is only modulated with a 3 THz signal.

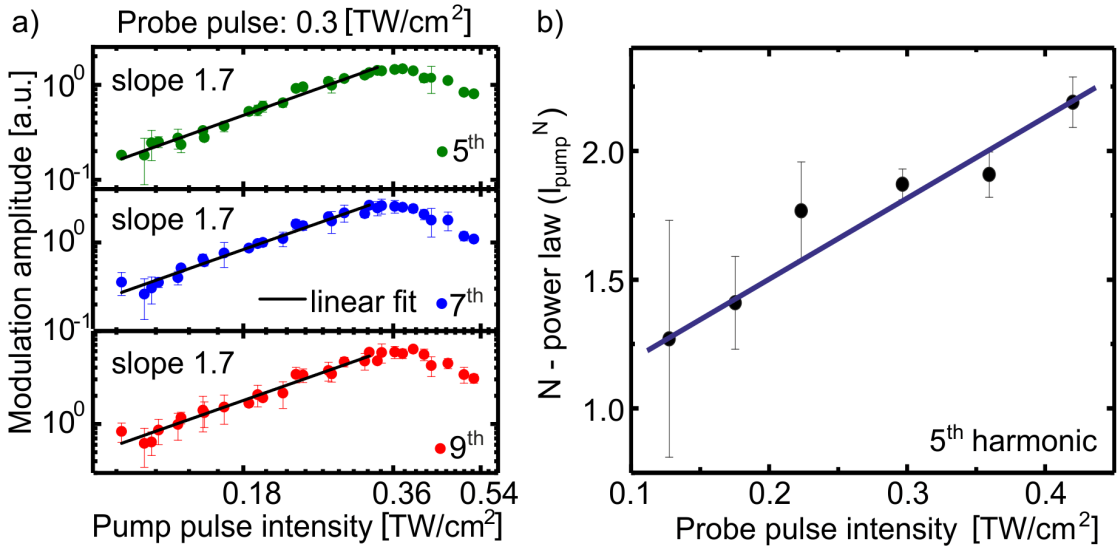

Figure 3.10: Dependence of the modulation on the pump pulse intensity. a) Amplitude of the 3 THz peak after the Fourir analysis of the time dependent 5^{th} (green), 7^{th} (blue) and 9^{th} (red) harmonic signal for different pump pulse intensities. The black line highlights the linear dependence of the oscillation strength on the pump pulse intensity up to roughly 0.4 TW/cm^2, in a log-log representation. b) Power law dependence of the oscillation amplitude (slope of the black line shwon in a)) on the probe pulse intensity, taken from the 5^{th} harmonic. The purple line is a guide to the eye to illustrate the linear growing dependence. Increasing the probe pulse intensity, the amplitude of the modulation grows faster as a function of the pump pulse intensity.

for all applied probe pulse intensities strengthen the role of the DECP instead of ISRS as the responsible coherent phonon excitation mechanism.

For higher pump pulse intensities, larger 0.36 TW/cm^2, the modulation amplitude saturates before it decreases. Note, it was experimentally confirmed that the drop of the amplitude is a reversible observation and not induced by material modifications (damage). Higher order phonon effects may set in, which could not be detected using HHG as a probe mechanism [77, 84, 87, 88].

Recently Uchida *et al.* [89] reported coherent phonons in GaSe excited by femtosecond mid-IR

pulses. By studying the transient transmission changes of a weak near-infrared pulse (1.5 eV), the authors also observed a saturation of the phonon amplitude for high mid-IR laser intensities. The authors suggest that the excitation of coherent phonons via ISRS saturates when the light intensity reach the non-pertubative light-matter-interaction regime.

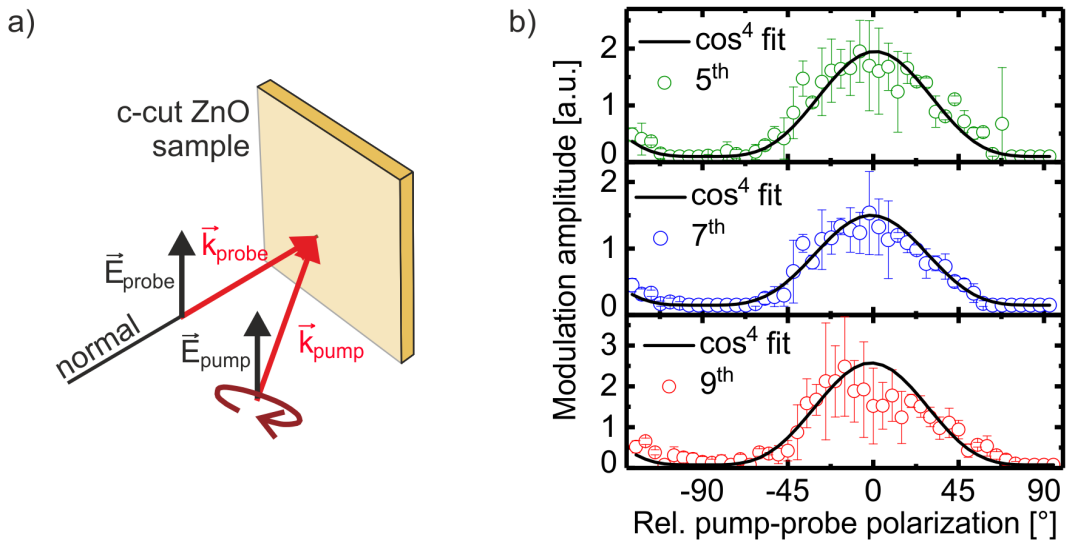

Figure 3.11: Modulation strength of the time resolved harmonic signal as a function of the relative pump-probe laser polarization. a) Experimental geometry of pump and probe beam alignment. The probe beam hits the ZnO sample normal to the surface, while the pump beam is aligned with an angle of roughly 10 ° In the experiment the probe pulse polarization $\mathbf{E}_{probe}$ was kept vertical linear polarized (perpendicular to the ZnO c-axis) while the linear pump pulse polarization $\mathbf{E}_{pump}$ was changed. b) Oscillation strength, determined by the Fourier analysis amplitude of the temporal resolved and spectral integrated 5th (green), 7th (blue) and 9th harmonic signal, as a function of the relative pump-probe polarization. The black line depicts a cos^4 fit of the data.

As the excitation and detection symmetry of the ISRS mechanism is defined by the symmetry of the Raman tensor, investigations on the symmetry properties may help to verify the role of the ISRS or DECP mechanism. Therefore, measurements on the relative pump-probe polarization were performed as illustrated in Figure 3.11 a. Figure 3.11 b shows the dependence of the modulation amplitude of the 5th (green), 7th (blue) and 9th (red) harmonic signal on the relative pump-probe linear polarization angle. The shown data, were measured for a fixed vertical probe pulse polarization $\mathbf{E}_{probe}$ and varied pump pulse polarization $\mathbf{E}_{pump}$. The oscillation amplitude is highest when pump and probe polarization are oriented parallel. However, there are no modulations present in the transient harmonic signal when the pump and probe polarizations are perpendicular to each other. Similar results are obtained when the pump pulse polarization $\mathbf{E}_{pump}$ was fixed and the probe pulse polarization $\mathbf{E}_{probe}$ was rotated. These results suggest a link between the pump pulse polarization and the phonon oscillation direction. Consequently, no influence on the HHG process is expected when the probe pulse polarization is perpendic-

ular to the lattice oscillations. The observations presented in Figure 3.11 b contradict to the symmetry properties expected from the ZnO Raman tensor which are theoretically predicted by group theory for a wurtzite structure [76, 77, 90, 91] and which have been experimentally proved by Lee *et al.* [79]. It is expected that both, the E_2^{high} and E_2^{low} mode, show a 180 ° rotational symmetry as a function of the relative pump-probe polarization angle and the modulation phase experience a π phase shift in the case of a 90 ° relative pump-probe polarization change (i.e. the modulation of the transient signal starts with a negative instead of positive slope). In Lee *et al.* [79] below band excitation using photon energies of 1.5 eV was used for the excitation of coherent phonons in ZnO (E_g=3.2 eV). Aside the fact that the authors make no statement about the used laser intensities, what makes it difficult to get a guess about the excited electron density, the experiment clearly works in the ISRS excitation mechanism regime. The harmonic modulation as a function of the relative pump-probe laser polarization shown in Figure 3.11 b is identical to observations of Ishioka *et al.* [81]. There close to the band gap, nearly resonant photon energies of 3.2 eV were used for impulsive coherent phonon excitation. Although the authors link their observations to the ISRS excitation mechanism, they also state that under the used experimental conditions $5 \cdot 10^{24}\,\mathrm{m}^{-3}$ electrons were excited. As shown by simulations given in Section 2.1.3 this number is equal or even higher than the excited electron density in experiments presented in this work using strong off-resonance excitation by 3.2 μm mid-IR laser pulses. Due to the high excited electron density in the work of Ishioka *et al.* [81] the role of DECP phonon excitation mechanism can not be neglected.

To summarize, the dependence of the high and low frequency modulation amplitude on the pump pulse duration clearly proves the impulsive character of the coherent phonon excitation mechanism. The modulation amplitude scaling as a function of the pump pulse intensity and the relative pump-probe-laser polarization contradicts with the expected dependence given by the Raman formalism. Additionally simulations, using the Keldysh-Drude approach and a strong PL emission, reveal a high excited carrier density. Thus, it is assumed that the DECP mechanism plays a dominant role in the excitation process of the coherent phonons.

If the higher frequency modulations at 7 and 10 THz are caused by nonlinear phononic processes, the dependence of the phonon excitation on the excitation power (=pump pulse intensity) should scale in respect to the nonlinear order. Figure 3.12 depicts the slow and fast modulation amplitudes of the E_2^{low}, E_2^{high}-$2 \cdot E_2^{low}$ and E_2^{high}-E_2^{low} mode at 3, 7 and 10 THz from a Fourier analysis as a function of the pump pulse intensity for a probe pulse intensity of 0.13 $\mathrm{TW/cm^2}$, respectively. An increasing power scaling law (given by the black line in Figure 3.12) of the E_2^{low}, E_2^{high}-$2 \cdot E_2^{low}$ and E_2^{high}-E_2^{low} is observed as a function of the modulation frequency. But the observed values contradict to the expected power scaling of N_{ph}, $3 \cdot N_{ph}$ and $2 \cdot N_{ph}$ for the E_2^{low}, E_2^{high}-$2 \cdot E_2^{low}$ and E_2^{high}-E_2^{low} mode, respectively.

It was shown in Figure 3.10 that the intense probe pulse has an effect on the vibrational state.

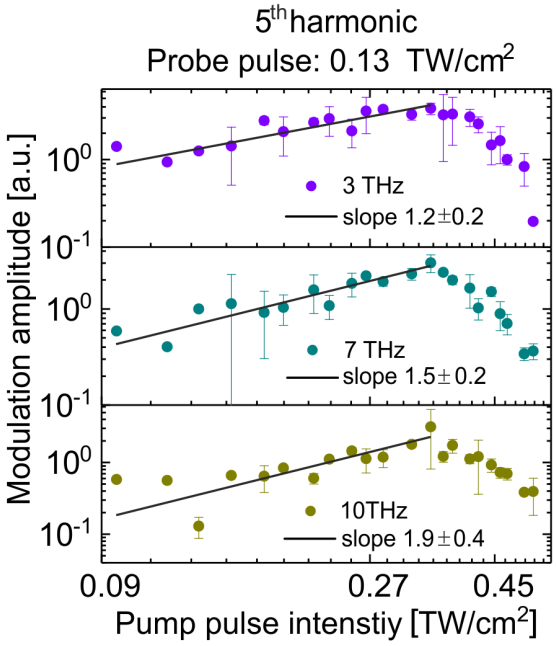

Figure 3.12: Pump pulse intensity dependent oscillations at the modulation frequencies 3, 7 and 10 THz in the 5th harmonic when the probe pulse intensity was 0.13 TW/cm^2. The power dependence given by the slope of the linear part in a log-log representation (highlighted by the black line) increases with the oscillation frequency.

Figure 3.13 a depicts the spectrally integrated transient high harmonic signal for the cases of 0.12 TW/cm^2 (upper), 0.16 TW/cm^2 (middle) and 0.21 TW/cm^2 (lower) probe pulse intensity when the pump pulse intensity was fixed to 0.27 TW/cm^2. While for the lowest probe pulse intensity the harmonic signal is modulated with multiple frequencies, the high frequency components become weaker for 0.18 TW/cm^2 and vanish completely for 0.21 TW/cm^2. This evolution is clarified by a Fourier analysis of the modulated harmonic signal as a function of the probe pulse intensity (Figure 3.13 b). The Fourier spectrum reveals for all measured probe pulse intensities a modulation frequency at 3 THz, whose amplitude is growing with increasing probe pulse intensity. For 0.12 TW/cm^2 and 0.16 TW/cm^2 probe pulse intensities the Fourier spectrum shows additionally a signal at 7 and 10 THz which becomes weaker and is shifted towards higher frequencies when the probe pulse intensity is increased. To explain the physics why the low frequency oscillation is increasing while the high frequency oscillations is decreasing as a function of the probe wavelength a theoretical model will be developed which is beyond the scope of this thesis.

Figure 3.13 c shows the modulation amplitude dependence on the probe pulse intensity for modulations in the transient 5th (green), 7th (blue) and 9th (red) harmonic signal. The modulation strength, is increasing as a function of the probe pulse intensity up to 0.25 TW/cm^2. For higher probe pulse intensities the amplitude saturates and decreases. In analogy to data shown in Figure 3.10 a it was confirmed that the drop of the modulation strength is reversible.

Figure 3.13 c and Figure 3.10 b clearly illustrate that the modulation strength depends on the pump pulse as well as on the probe pulse intensity. Thus the probe pulse, which is generating the high harmonic signal used to trace the lattice oscillations can not be considered as weak

pertubation to the matter. It is assumed that the coherent wavepacket created by the pump pulse interacts with phonons generated by the probe pulse in a coherent or incoherent manner.
So far only the excitation of coherent optical phonons in ZnO, their dependence on various experimental parameters and their effect on the HHG process were discussed. Now investigations on HHG in a transiently highly excited semiconductor ZnO will be presented.

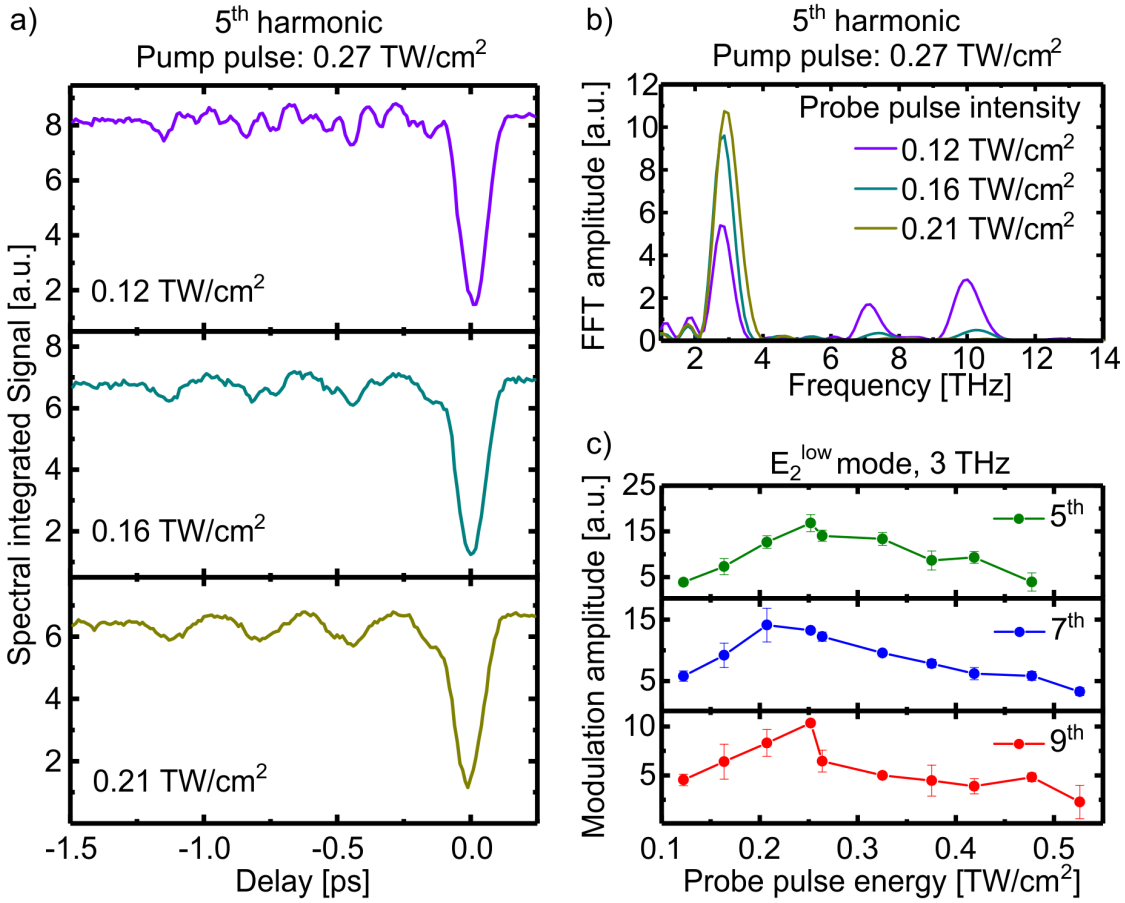

Figure 3.13: High frequency modulations of the transient HHG signal as a function of the probe pulse intensity for a fixed pump pulse intensity of 0.5 TW/cm^2. a) Spectral integrated signal of the 5th harmonic as a function of the pump-probe delay for three different probe pulse intensities. In case of the weakest probe pulse with an intensity of 0.12 TW/cm^2 the harmonic signal is clearly modulated with multiple frequencies (upper panel). Applying a larger probe pulse intensity of 0.16 TW/cm^2 the slow modulation becomes much more dominant but still there is a second modulation frequency visible (middle panel). For even higher intensities the fast modulation vanish and only the slow one with a period of roughly 300 fs are present (lower panel). b) Fourier analysis of the oscillatory part shown in a). The slow oscillation at 3 THz is growing with the probe pulse intensity. The fast oscillations show the opposite behaviour. Furthermore, the frequencies of the fast modulation at roughly 7 and 10 THz shift toward lower frequencies when the probe pulse intenstiy is decreased. c) Probe pulse dependence of the slowest modulation frequency amplitude in the 5th (green), 7th (blue) and 9th (red) harmonic signal determined from the oscillatory part of the transient HHG spectra by Fourier analysis.

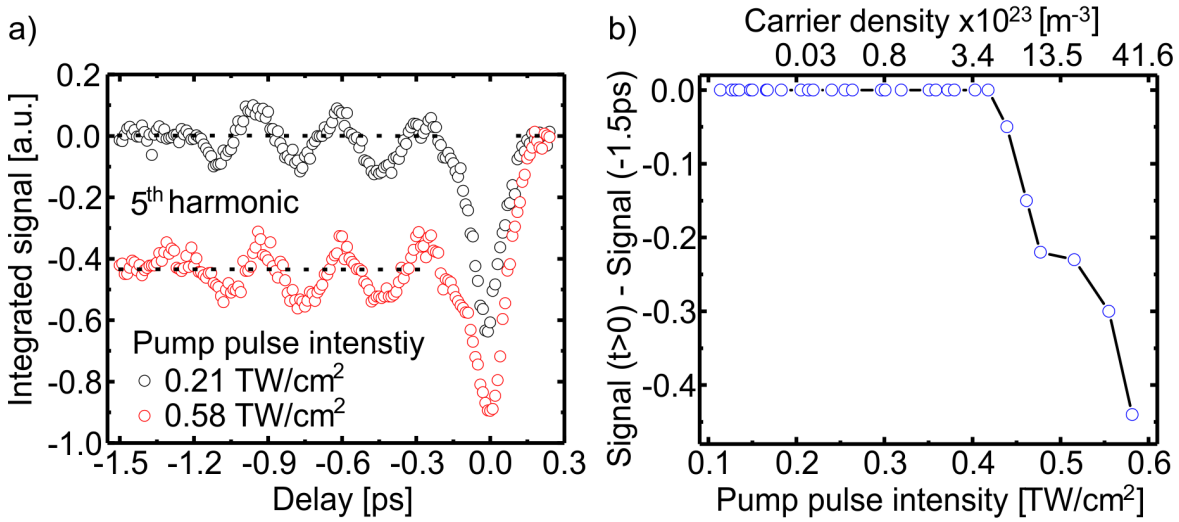

Figure 3.14: a) Spectrally integrated signal of the 5th harmonic for two pump pulse intensities and fixed probe pulse intensity. The harmonic yield generated when the probe pulse arrives after the pump pulse (ΔT<0) dependence on the pump pulse intensity. b) Quantitative drop of the high harmonic signal dependent on the pump pulse intensity.

As shown in Figure 3.6 a, b the HHG signal is the same for positive and negative time delays, i.e. for the situation that the pump pulse arrives after and before the probe pulse, respectively. Only when the probe and pump pulse overlap in time the harmonic signal vanishes. The strong PL signal shows, that this behaviour is most probably linked to high excited carrier density, i.e. the high density of free carriers prevents efficient HHG in the ZnO material. Figure 3.15 a depicts the spectral integrated signal of the 5th harmonic for the cases of two different pump pulse intensities 0.21 and 0.58 TW/cm^2. Indeed increasing the pump pulse intensity leads to a reduction of the high harmonic signal when the pump pulse arrives before the probe pulse (negative time delays). The difference between the harmonic signal when the pump pulse arrives after and before the probe pulse was considered as a value to quantise the HHG efficiency drop as a function of the excited carrier density. In Figure 3.14 b the HHG signal reduction is shown as a funciton of the pump pulse intensity. After a threshold pump pulse intensity the HHG efficiency drops. Wang *et al.* [92] performed similar experiments using near-ultraviolet light (0.4 μm, 3.1 eV) for pumping and mid-IR for probing HHG in photo doped ZnO. The authors measured a similar dependence, as shown in Figure 3.14 b and explained it by ground state depletion, i.e. the pump pulse excites a high amount of carriers and due to state blocking (Pauli blocking) the excitation probability induced by the probe pulse is reduced or zero at all. The authors further ruled out the possibility of a reduced HHG yield due to an increasing electron-electron scattering rate as a function of the excited electron density [92]. Further the authors recorded a HHG reduction (as shown in Figure 3.14) independent on the relative pump-probe field polarization in agreement with observations in this thesis. Wang *et al.* [92] state an excitation fraction of 1-25 percent, 10^{20} – 10^{21} cm^{-3} in their experiments. The authors of the paper do not specify which fraction

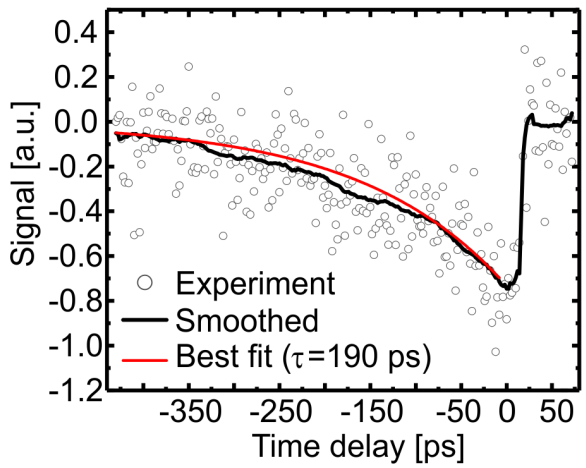

Figure 3.15: Spectral integrated signal of transient 5th harmonic signal as a function of the pump-probe delay up to 450 ps. A single exponential fit (red curve) reveals a decay time constant of 190 ps.

was used (VB or total electron number). The given numbers make only sense if its assumed that the excitation fraction of the VB electrons is meant (see page 14). Trusting that numbers, in the work of Wang *et al.* [92] two orders of magnitude higher electron densities are excited compared to the experiments presented here. Because the authors do not give any details about the laser pulse characterization especially pulse duration and spot size, it is not possible to recalculate the excited electron density. Thus a comparison with calculated values in this thesis is not possible.
In order to prove that the excited carrier density causes the HHG efficiency drop, experiments with long time delays were performed to cover the spontaneous electron recombination time. Figure 3.15 depicts the spectral integrated signal of the 5th harmonic as function of pump-probe delay up to a delay time of 450 ps. The high harmonic signal gradually recovers and the signal reaches the level of the unperturbed case (i.e. positive pump-probe delays) after roughly 430 ps. Using a single exponential fit (red curve) the recovery corresponds to a time constant of 190 ps, in agreement to reported spontaneous recombination times in literature [37, 93, 94].
To conclude, it was shown that HHG from a 3.2 μm laser pulse in highly excited semiconductors is affected by the free carrier concentration. Thus, the harmonic spectrum experience a continuous blueshift of tenths of nanometers as a function of the excited carrier density. Further, when the carrier density reaches the Mott density, the emission spectra shows an additional emission band resulting from EHP formation.
Furthermore, dynamical effects upon highly exciting a semiconductor far out of the equilibrium state by a far off-resonance 3.2 μm pulse, were studied using transient HHG from a 3.2 μm pulse in a pump-probe experiment. The large number of free carriers excite coherent optical phonon via the DECP mechanism. Investigations on the scaling of the modulation amplitude as a function of the pump and probe intensity revealed the invasive nature using HHG to probe transient material modifications. Furthermore, it was shown that high harmonic generation in solids can be controlled by the number density of excited carriers.
Although the experimental data clearly show that the observed oscillations in the harmonic ra-

diation generated by the probe pulse as a function of the pump-probe delay origin from lattice vibrations in the ZnO material, many open question remain. Mainly the coupling mechanism between HHG and coherent lattice vibrations (coherent phonons) is not fully understood, yet.

3.2 Carrier envelope phase resolved HHG in solids

The experiments presented in the previous section had been performed with femtosecond mid-IR laser pulsed generated in a BBO-based optical parametric amplifier with subsequent non-collinear DFG. While this allows the generation of mid-IR pulses of sub 100 fs duration, due to the different carrier-envelope phase (CEP) of the signal and idler beam the CEP of the mid-IR can not be passively stabilized.
In the following section experiments were presented using a CEP stable optical parametric chirp pulse amplification (OPCPA) which provides sub-50 fs pulse at 3.2 μm central wavelength. The laser system is operated at the Extreme Light Infrastructure (ELI) in Szeged, Hungary. The laser system passively stabilize the CEP due to the optical parametric generation process. Additionally the use of a f-2f interferometer generating a CEP feedback signal, in combination with a acusto-optical phase modulator allows active CEP stabilization and a precise control of the CEP. Applying adaptive compression techniques allowed to generate 24 fs (2.4-cycle) laser pulses. This laser system enabled investigations on the CEP dependence of the HHG process in ZnO.
A detailed knowledge about CEP of mid-IR laser pulses and its effects in light matter interaction are needed since in recent years strong field laser physics has experienced a shift towards from the near-IR to the mid-IR spectral range. This is mainly motivated by the beneficial scaling law of the ponderomotive energy $U_\mathrm{p} \propto I_0\lambda^2$ towards longer wavelengths [95, 96]. As discussed in Section 2.1.3, due to the risk of an avalanche excitation process, strong laser fields can only be applied when the pulse is short in order to avoid electron heating. Consequently, in strong field applications, few-cycle laser pulses are desired [97, 98, 99, 100], in which the CEP becomes increasingly important as the phase of the electric field relative to the envelope becomes a dominant contribution once the pulse duration reaches the cycle period of the laser pulse.

3.2.1 Experimental methods, (n-1)f-to-(n+1)f interferometry

The MIR laser system provides 145 μJ, 4 optical cycles pulses (45 fs), centered at 3.2 μm with a repetition rate of 100 kHz. The system has unique <100 mrad CEP stability and also provides unprecedented CEP control during experiments. The output of the OPCPA system is compressed to 24 fs using non-linear self-compression in a 2 mm-thick yttrium aluminum garnet

(YAG) crystal [101, 102, 103] and a 1 mm-thick Si plate for dispersion compensation. Figure 3.16 a depicts the temporal reconstruction of the compressed pulses measured by a SHG-FROG technique. The measured FROG trace is shown in the inset of Figure 3.16 a. To avoid any additional dispersion, the beam splitting in the FROG setup was realized by spatially dividing the beam in two D-shape parts using a D-shaped mirror. As shown in Figure 3.16 b after compression in the YAG material the spectrum is still centered at 3.2 μm. The reconstructed spectral phase shows a quadratic dependence roughly at the main part of the spectrum. The CEP of the laser pulses is passively stable and additionally actively stabilized and controlled by an acusto-optical phase modulator (Fastlite, Dazzler). The active regulation of the CEP was achieved by the feedback from an f-2f interferometer in combination with a CEP measurement processing unit (Fastlite, Fringezz). Beside stabilizing the CEP, the Dazzler can be used to vary the CEP continuously, while the f-2f interferometer monitored the CEP variations.

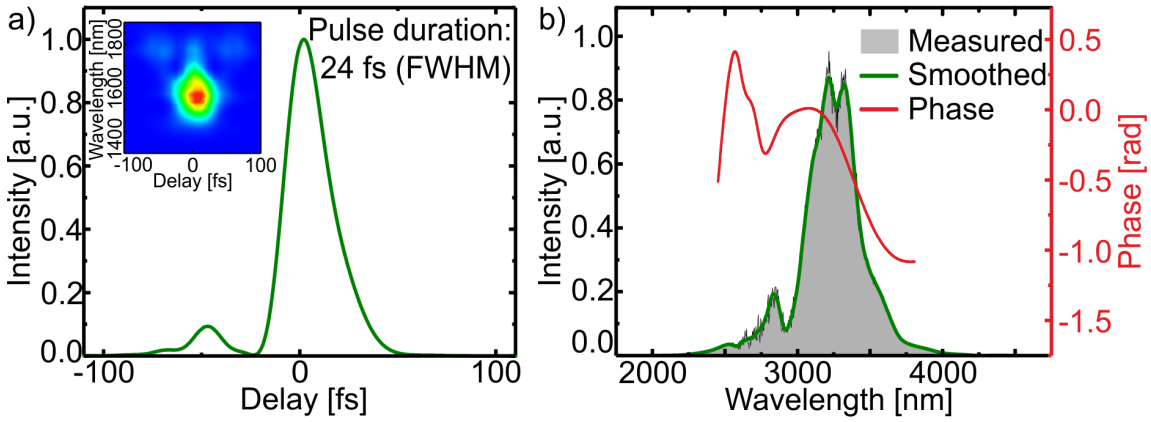

Figure 3.16: Laser pulse characterization. a) Reconstruction of the temporal shape of the laser pulse after spectral broadening in the YAG and compression in silicon material. The inset shows the measured FROG trace. The FWHM pulse duration was determined to be 24 fs which corresponds to 2.4 cycles of the electromagnitic field with a wavelength of 3.2 μm. b) Measured spectrum of the mid-IR laser pulse after compression (green line). Reconstructed spectral phase from the FROG trace shown in a) (red line). In the main part around 3.2 μm the phase shows small quadratic dependence.

Figure 3.17 a depicts a schematic illustration of the used experimental setup to investigate HHG in ZnO as a function of the CEP. To avoid dispersive material in the optical path of the laser a gold coated concave mirror (f=15 cm) was used to focus the laser to a spot size of roughly 200 μm normal to the surface of a 100 μm thick c-cut ZnO crystal. The peak intensity and field strength were calculated to be 3 TW/cm^2 and 0.4 V/Å, respectively. This values are clearly below the reported damage threshold value for ZnO excited under similar conditions [17]. The generated high harmonic radiation was focused to the entrance slit of a UV-VIS spectrometer (Avantes Avaspec ULS3648) by a f=5 cm CaF_2 lens. The integration time was typically 1 ms, which corresponds to averaging over 100 laser shots. To avoid focusing of intense mid-IR light onto the entrance slit of the spectrometer a fused silica window was placed after the sample and

in front of the spectrometer (not shown). All experiments were carried out at room temperature and ambient atmosphere.

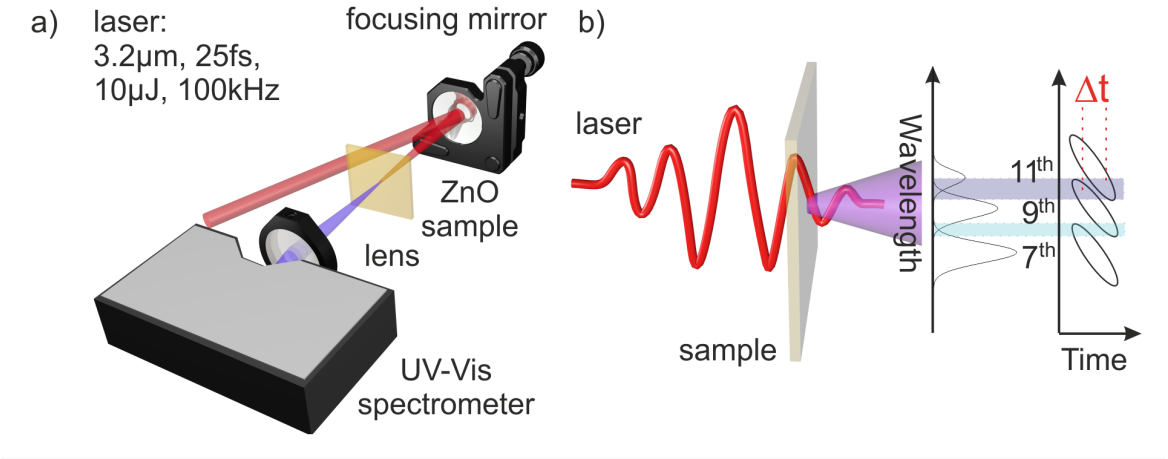

Figure 3.17: Experimental setup used to investigate high harmonic generation (HHG) from CEP stabelized laser pulses in bulk semiconductor ZnO. The laser source, an OPCPA system with subsequent pulse compression in a YAG plate and dispersion compensation in silicon, delivered the used few-cycle mid-IR laser pulses with a repetition rate of 100 kHz at 3.2 μm and a pulse duration and energy of 25 fs (2.4 cycles of the electric field at 3.2 μm) and 10,μJ, respectively. The laser was focused by a f=15 cm gold coated concave mirror onto the a 100 μm thick c-cut ZnO crystal. The emission from the sample was refocused to a spectrometer (UV-VIS) using a f=5 cm CaF_2 lens. b) Schematic illustration of the method used to exctract pulse and HHG phase information especially the pulse CEP by measuring high harmonic spectra.

Figure 3.17 b illustrates the method used to extract phase information out of the CEP dependent generation of high harmonics in ZnO. If the spectral width of the fundamental laser spectrum $\Delta\lambda_{\mathrm{FWHM}}$ fullfills the condition

$$\frac{\Delta\lambda_{\mathrm{FWHM}}}{\lambda_0} > \frac{2}{n} \tag{3.2}$$

the $n+1$ and $n-1$ harmonic order generated by a laser at the central wavelength λ_0 overlap. The spectral overlapping red and blue part of the $n+1$ and $n-1$ order lead to an interference pattern

$$\Pi_{int}(\omega) \propto \Pi_{n+1}\Pi_{n-1} \cdot cos(\phi_{int}(\omega)) \tag{3.3}$$

determined by the spectral intensities $\Pi_n = F_{\mathrm{el}}^n$ and the phase difference

$$\phi_{int} = \phi_{n+1} - \phi_{n-1}. \tag{3.4}$$

The spectral phase of the n-th order harmonic is determined by the driving field F_{el} and given by

$$\phi_n(\omega) = n \cdot \phi_{\mathrm{CEP}} + n \cdot \phi_1 (\omega - \omega_0) + n \cdot \frac{\phi_2}{2} (\omega - \omega_0)^2 + \phi_{n,\mathrm{HHG}}. \tag{3.5}$$

With ϕ_{CEP} the CEP, ω_0 the central frequency, ϕ_2 the GVD of the fundamental pulse and $\phi_{n,\mathrm{HHG}}$ an intrinsic phase introduced by the HHG-process itself. Because the linear term in Equation 3.5

has no effect, the interference between the harmonics is determined by the GVD and CEP of the fundamental pulse as well as the intrinsic phase. As illustrated in Figure 3.17 b if the fundamental pulse carries a non-zero GVD, this chirp is adopted by the individual harmonic orders, i.e. the red and blue spectral part of the harmonic orders are time delayed. Consequently, the interfering red and blue part of the n+1 and n-1 harmonic order are delayed by Δt (see Fig. 3.17 b). This leads to a modulation of the spectral interference pattern by a frequency Δt^{-1}. The phase of the interference pattern is given by:

$$\phi_{int}(\omega) = \omega\Delta t + \phi_{0,int} + \Delta\phi_{HHG} \tag{3.6}$$

Substituting Eq. 3.5 into Eq. 3.4, $\phi_{0,int}$ and Δt are identified to

$$\phi_{0,int} = 2 \cdot \phi_{CEP} \tag{3.7}$$

and

$$\Delta t = (n+1) \cdot \left.\frac{\mathrm{d}\phi}{\mathrm{d}\omega}\right|_{\omega_{red}} - (n-1) \cdot \left.\frac{\mathrm{d}\phi}{\mathrm{d}\omega}\right|_{\omega_{blue}}. \tag{3.8}$$

This theoretical consideration suggests, that the CEP of a spectrally sufficiently broad laser pulse can be determined by measuring the HHG spectra.

3.2.2 CEP measurement using HHG in solids

The following section demonstrates the measurement of the relative laser pulse CEP using HHG in ZnO.

Figure 3.18 a shows a typical recorded spectrum with harmonics up to the 13$^{\text{th}}$ order. Due to the used experimental geometry the electric field vector of the laser is always perpendicular to the c-axis of the ZnO crystal, leading to the generation of only odd harmonic orders [71]. Figure 3.18 b shows high harmonic generation spectra as a function of the recorded CEP-dependence. Here, the CEP of the driving laser pulses was varied in a triangular waveform manner using the acusto-optical phase modulator (Dazzler), i.e. a constant slope from 0 to 2π and back. Between all odd harmonics a clear oscillating structure of diagonal lines as a function of the CEP was observed. The variations in the signal strength (vertical features) were attributed to short-term fluctuations of the laser power or pointing. Importantly, the CEP-dependent interference pattern was not notably affected by these fluctuations which was attributed to the very similar intensity scaling of adjacent order harmonics in the non-perturbative regime [17]. Further the spectra presented in Figure 3.18 show another pronounced feature consisting in the strong modulations of the 5th harmonic. Note, this fringe pattern was independent on CEP changes. These oscillations result from the interference between the delayed 5$^{\text{th}}$ harmonic radiation generated at the front and rear surfaces of the ZnO sample. Thus, the spectral spacing in

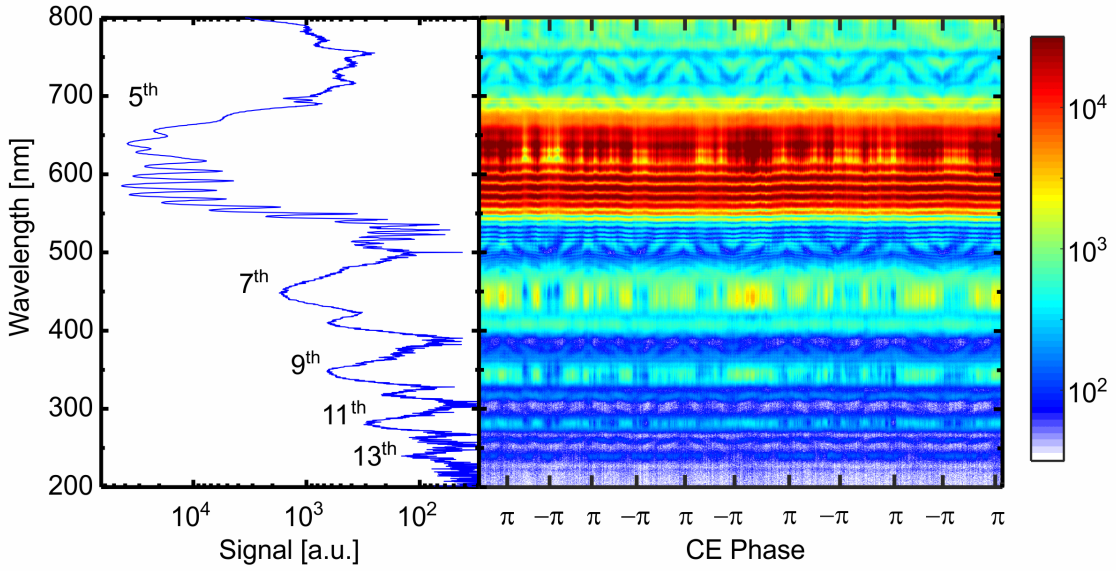

Figure 3.18: a) Typical spectrum showing odd high harmonics generated in a 100 μm thick c-cut ZnO crystal by a 25 fs long CEP-stabilized pulse. b) Measured series of high harmonic spectra using 25 fs pulse, while the CEP is varied using the acusto-optical phase modulator (Dazzler). The colorbar encodes the measured signal strength on a logarithmic scale.

the 5th harmonic is given by:

$$\Delta\lambda = \frac{\lambda^2}{c\Delta t} = \frac{\lambda^2}{cd} \cdot \left(\frac{1}{v_g(\lambda)} - \frac{1}{v_g(\lambda/5)} \right)^{-1} \tag{3.9}$$

In Equation 3.9 d denotes the thickness of the ZnO sample (100 μm),

$$v_g = \frac{c}{n_\mathrm{r}} \left(1 - \frac{\lambda}{n_\mathrm{r}} \frac{\mathrm{d}n_\mathrm{r}}{\mathrm{d}\lambda} \right)^{-1} \tag{3.10}$$

the group velocity of the fundamental beam and the 5th harmonic, n_r the refractive index and c the speed of light.

In Figure 3.19 a an enlarged view of the 5th harmonic spectrum, where the change of the variation of the fringe spacing is apparent, is shown. Figure 3.19 b depicts a comparison of the calculated fringe spacing $\delta\lambda(\lambda)$, using Equation 3.9, and the measured ones. The measured and calculated values coincide nearly perfectly, indicating that due to the wide spectrum of the 5$^{\mathrm{th}}$ harmonic the modulation frequency changes over the spectrum. Similar spectral modulations have been reported by Franz *et al.* [104]. The authors showed that the modulations vanish when a short focusing lens is used in the experiment. Thus, a higher intensity on the rear compared to the front surface of the sample is achieved which finally leads to a strongly reduced HHG from the front side. Due to absorption of the harmonics produced at the front side of the ZnO crystal the spectral interference disappears below roughly 500 nm. Consequently, for harmonics below

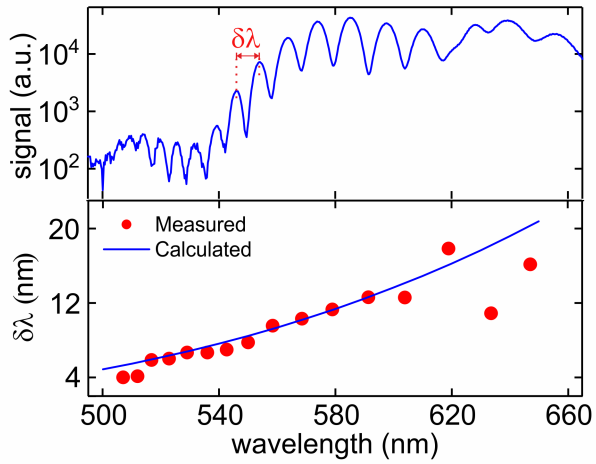

Figure 3.19: Spectral interference in the 5th harmonic. a) Measured spectrum in the vicinity of the 5th harmonic, exhibiting a narrow fringes pattern due to interference between harmonics generated on the front and back surface of the ZnO sample. b) Measured and calculated (using equation 3.9) spectral fringe spacing in the 5th harmonic.

500 nm only the light generated at the rear surface reaches the detector.

Now the focus will be on CEP dependent features shown in Fig. 3.18 b. Figure 3.20 a depicts measurements where the CEP was varied in a triangular pattern (sinusoidal pattern see appendix D) by applying a triangular shaped alternating voltage on the Dazzler. The spectra were recorded using a bandpass filter with transmission between 430 and 250 nm. The emission spectra show the 9^{th} and 11^{th} harmonic of the 3.2 μm laser and clear CEP-dependent interference patterns between the harmonic orders. The triangular phase variations are clearly imprinted in the interference pattern. Applying a fast Fourier transform (FFT) of the spectrum in the range from 260 to 400 nm, the relative phase of adjacent harmonics can be retrieved from individual spectra. The relevant frequency of the interference fringes was identified in the Fourier power spectrum and its phase was unwrapped and plotted in Figure 3.20 c. The reconstructed phase from the HHG signal (blue line) is twice, compared to the measured CEP using the f-2f interferometer at the laser output (red dots). It is important to note that the relative phase of the harmonics with order (n-1) and (n+1) varies by $2\Delta\Phi$ when the CEP is changed by $\Delta\Phi$ (see Equation 3.7). Therefore, the reconstructed phases in Figure 3.20 c oscillate between 0 and 4π while the CEP was varied between 0 and 2π. This increased sensitivity to CEP variations leads to an ambiguity of 2π when measuring the CEP via spectral interference of odd order harmonics. This ambiguity could be removed by using non-isotropic media such as a-cut ZnO, where even harmonics can be generated. In that case, the same procedure could be applied to neighbouring even and odd order harmonics, whose relative phase varies by $\Delta\phi$ when the CEP is changed by $\Delta\phi$. Note, it has been shown that the even harmonics may polarized perpendicular to the driving laser field [105, 106]., thus, a polarizer has to be used between the sample and the spectrometer to enable interference.

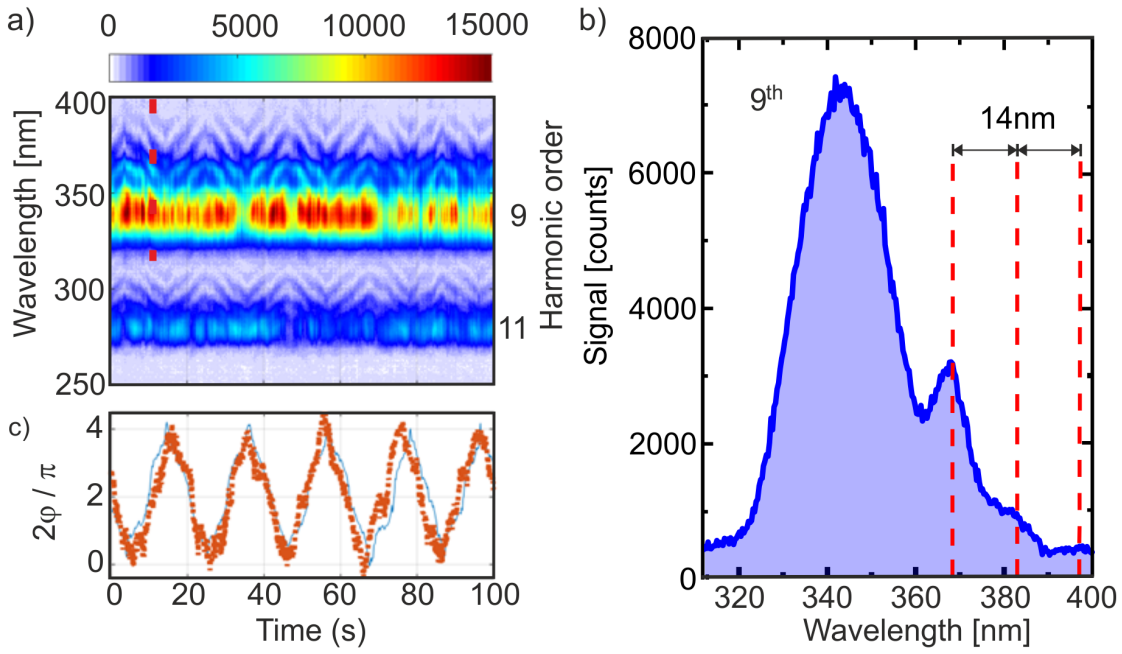

Figure 3.20: Determination of the relative CEP using HHG in ZnO. Shown are series of spectra in the region around the 9th and 11th harmonic. The CEP of the fundamental pulses is varied in a triangular pattern a) or a sinusoidal pattern b) with a frequency of 1/2 Hz. The fringe patterns in between the harmonic signals is used to obtain the relative phase between adjacent odd-order harmonics, which corresponds to twice the CEP π. Panels c) and d) show the reconstructed values of 2π (solid lines) along with the CEP values recorded by the f-2f interferometer (dotted lines).

Furthermore, the spectral interference shown in Figure 3.20 b reveal a temporal delay of the red part of 9^{th} and the blue part of the 7^{th} harmonics of 16.9 fs (as illustrated in Fig. 3.17). The group delay mismatch introduced from ZnO dispersion between the parts of pulse corresponding to the red part of the 9^{th} and the blue part of the 7^{th} harmonic are given by $9 \cdot 0.375\,\mu m = 3.38\,\mu m$ and $7 \cdot 0.375\,\mu m = 2.63\,\mu m$ was estimated to be 1.63 fs. Additionally the mid-IR pulse generating the harmonics was carrying a group delay mismatch before arriving the ZnO sample. From the reconstruction of the spectral phase, shown in Figure 3.16 b, a group delay mismatch of the red part of 9^{th} and the blue part of the 7^{th} harmonics generated by the mid-IR pulse was estimated using Equation3.8 to be 30 fs.

Together with the group delay introduced by the ZnO material a total time delay of 30 ± 2 fs is expected, this number differs by roughly a factor of 2 from the value derived from the spectral interferences (Fig. 3.20). This in fact implies that there is an additional phase term, resulting from HHG-process itself (also known as atto chirp) or due to measurement uncertainties the group delay of the laser pulse wasn't determined accurately enough. This uncertainty will be ruled out in upcoming experiments using two independent pulse characterization techniques (FROG and discrete d-scan) to determine the laser pulse phase.

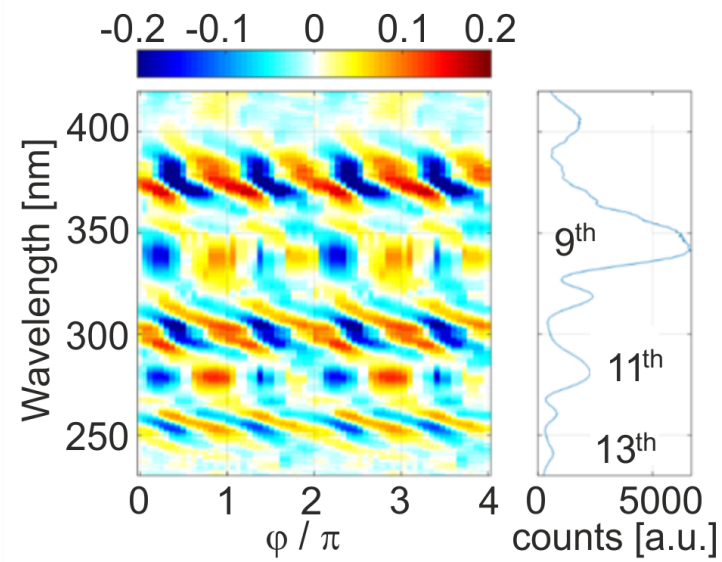

Figure 3.21: CEP-resolved high harmonic spectrum generated by a few-cycle mid-IR laser. Several harmonic orders are indicated. The relative CEP π is obtained from the interference fringes between the harmonics using the method described in the text.

So far it was shown that the relative CEP can be reliably measured using the spectral interferences in the HHG emission signal as it is predicted by Equation 3.5. Using this knowledge to extract the CEP as shown in Figure 3.20, Figure 3.21 shows a phase resolved high harmonic spectrum which was obtained by calculating the normalized difference, $(\Pi(\phi) - \Sigma)/(\Pi(\phi) + \Sigma)$, between the CEP-dependent harmonic spectra $\Pi(\phi)$ and the CEP-averaged spectra $\Sigma = 1/2\pi \int \Pi(\phi)\mathrm{d}\phi$. In addition to the interference fringes between the harmonics, the yield of the highest harmonics exhibits a clear CEP dependence, both show a π periodicity. While the interference fringes between the harmonic orders show a clear energy (wavelength) dependence, the modulations on the harmonic peaks do not exhibit a tilt. This suggests that they do not originate in spectral interference but rather in the HHG process itself and thus can be perspectively used to determine the intrinsic HHG phase.

The dependence of the HHG process on the CEP have already been investigated in different materials and driving laser wavelengths [14, 107, 108, 109, 110]. A π periodic modulation and shift of the photon energy of high harmonics as a function of the CEP have been reported in GaSe [14], fused silica [107], MgO [108] and Si [109] using THz, NIR and Mid-IR few-cycle laser pulses, respectively. While You *et al.* [108] explained their results by the delay between different harmonics, well known as atto-chirp from gas-phase harmonics, Shiari *et al.* [109] identified the chirp of laser pulse as the origin of the energy shift. In contrast to upper mentioned results harmonic modulations with a 2π periodicity without atto-chirp have been measured by You *et al.* [107] in crystalline quartz (SiO_2). This findings have be linked to the different crystalline properties compared to fused silca. Garg *et al.* [110] measured HHG in SiO_2, insensitive on the CEP and explained this with the intraband generation mechanism of the high harmonic radiation. A detailed explanation of the origin of the observed modulations using ZnO and the presence of an atto-chirp in HHG in solids will need further experimental investigations and is

out of the scope of this thesis.
To conclude, few cycle mid-IR laser pulses with a controllable CEP phase were used to investigate the dependence of HHG in ZnO. A simple and economical method to determine the relative CEP of mid-IR laser pulses using HHG in solids was demonstrated. Further the perspective potential to study the intrinsic phase of the HHG process was presented.

3.3 Conclusion

In this chapter interaction of intense mid-IR femtosecond laser pulses at 3.2 μm central wavelength with 100 μm thick ZnO bulk material was investigated. Due to the strong field Zener tunneling and impact ionization upon free carrier absorption a high carrier density is excited in the ZnO sample what modifies the HHG process. Increasing the carrier density by one order of magnitude from roughly 0.1 to $11 \cdot 10^{24}\,\mathrm{m}^{-3}$, the 7^{th}, 9^{th} and 11^{th} harmonic order spectrally shift by roughly 10 nm. Since the fundamental laser spectra show no spectral shift as a function of the injected carriers, it is assumed that the HHG-process itself is affected by the free carriers. A pump-probe experiment was used to study the transient effects of the high carrier density, induced by a 3.2 μm pump pulse, on the high harmonics generated from a 3.2 μm the probe pulse. The transient high harmonic radiation was modulated with frequencies at 3, 7 and 10 THz. This modulation can be linked to the E_2^{low}, E_2^{high}-$2 \cdot E_2^{\mathrm{low}}$ and E_2^{high}-E_2^{low} coherent optical phonon modes in ZnO. Investigating the modulation as a function of the pump pulse duration, relative pump-probe laser polarization as well as pump and probe pulse intensity revealed an excitation of the lattice displacement most likely via the DECP mechanism. Furthermore, due to the probe pulse parameter dependent modulation features, HHG depicts an invasive method to study the vibrational state of matter. It was also shown that photo-carrier doping of the conduction band by the pump pulse can be used to control the efficiency of HHG process.
This results demonstrate the complexity of the situation upon high carrier injection to the CB as a result of strong light field-condensed matter interaction. Consequently, the carrier based modifications on the electronic as well as crystalline structure have to be taken into account when intense ultrashort laser pulses are applied aiming to introduce conductivity changes with petahertz clockrate.
Using 2.4-cycle CEP stabilized and controllable laser pulses at 3.2 μm a simple method to measure the CEP using HHG in solids was developed by measuring the interference fringes created by adjacent harmonics. The study of the HHG as a function of the CEP perspectively may be used to study intrinsic phase terms introduced by the HHG process, also known as atto chirp.

Chapter 4

Far off-resonance pumped polycrystalline ZnO thin films

By reducing the thickness of a solid material in propagation direction down to hundreds of nanometer size its possible to study light matter interaction neglecting nonlinear propagation effects. Further interesting physical properties appear for polycrystalline semiconductor thin films due to their morphology which remain absent in bulk crystals. One reported feature is lasing emission benefiting from the high gain in semiconductors and the possible feedback mechanism linked to the grain boundaries leading to random lasing. Exploiting the intrinsic link between the onset of optically pumped lasing and the therefore required photo-excited carrier density (see Section 2.2.3), absorption can be investigated quantitatively as a function of the light wavelength in different regimes of excitation. Indeed optically pumped near-ultraviolet (NUV) lasing in polycrystalline ZnO thin films using pump light energies above the band gap and thus in the single photon absorption regime have been investigated intensively over the last decades [45, 111, 112, 113, 114, 115, 116, 117, 118, 119]. However, for many applications in medical (photodynamic therapy) [120], imaging (multiphoton fluorescence microscopy) [121, 122, 123] and information (three dimensional data storage) [124] technologies the multiphoton absorption regime is beneficial. In this Section, the onset of lasing is used as a experimental probe to investigate the photo-absorption of intense femtosecond near to far-infrared laser pulses in the semiconductor material ZnO as a result of strong light field interaction with matter.

Polycrystalline ZnO films with a defined thickness down to few hundreds of nanometers can be synthesized using different techniques [125]. The 300 nm thick ZnO thin film samples were synthesized by RF-magnetron sputtering. In Section 4.1.1 the results on the morphological and structural characterization of the films by scanning electron microscope (SEM) and x-ray diffraction (XRD) are presented. The role of free carriers on the lasing threshold was inves-

tigated using Aluminium (Al) doped ZnO thin films. Therefore the expected Al-doping concentration after ion implantation in the intrinsic ZnO films using a linear accelerator is shown. Section 4.1.2 is applied to explain the experimental setup including used laser sources to study the NUV emission from optically excited thin films. In Section 4.2 results on NUV stimulated emission pumped by a three photon absorption process are presented. Section 4.2.1 refer to the threshold pump laser intensity necessary to achieve stimulated emission in intrinsic and Al-doped ZnO thin films. Furthermore, the dependence of the three photon absorption process in ZnO thin films is presented as a function of the laser polarization, especially the ellipticity in Section 4.2.2. As introduced in Section 2.1, a significant carrier injection into the CB can be achieved in ZnO using far off-resonance femtosecond laser pulses in the near to the far-infrared spectral range. The carrier density can be even sufficient to induce population inversion and thus enable lasing if a resonator like morphology is applied. In Section 4.3.1 the results on stimulated emission in intrinsic ZnO thin films pumped by femtosecond mid-IR laser pulses in the tunneling regime are presented. A sudden spectral narrowing accompanied by a super linear increase of the ZnO emission as a function of the pump power mark the onset of lasing when threshold intensity is reached. The dynamics of the NUV emission were measured to ensure that the lasing is achieved. Conclusively the transition from a slow to a fast decaying signal appears when the laser threshold is reached, as described in Section 4.3.2. Moreover the dependence of the threshold pump intensity on the excitation laser spot size is used to reveal the underlying feedback mechanism. The optical pumping relies fundamentally on laser driven inter- and intraband absorption processes. In order to prove the concept and demonstrate the importance of intraband free carrier absorption in interband excitation processes, results on the pump wavelength dependence of the threshold pump intensity in the wide spectral range from the near to the far-infrared are presented in Section 4.3.3.
Results of this chapter are published in Ref. [126].

4.1 Methods on thin films experiments

High quality thin film samples in terms of good optical properties are required in order to emerge laser emission. Therefore, radio frequency (RF)-magnetron sputtering was performed followed by scanning electron microscope (SEM) as well as X-ray diffraction (XRD) methods applied to characterize the structural and morphological properties of the films.

4.1.1 Rf-magnetron sputtering, doping and characterization

RF-magnetron sputtering

The ZnO thin film samples were produced in collaboration at the Institute for Solid State

Physics at the Friedrich Schiller University Jena in the group of Prof. Carsten Ronning. Intrinsic, approximately 300 nm thick, polycrystalline ZnO thin films were grown by magnetron rf-sputtering (rf-power about 150 W) on 0.5 mm thick c-plane sapphire substrates at a pressure of about $2.95 \cdot 10^{-3}$ mbar in an argon atmosphere with a small amount (2 volume percent) of oxygen. Subsequently, the samples were thermally annealed in air at 900 °C for 60 min.

Sample characterization

The structural properties of the films were analysed using SEM and XRD techniques. The SEM cross section image, as shown in Figure 5.1a, depicts the columnar growth of the thin film grains and the film thickness of 300 nm. Both the intrinsic as well as the Al-doped ZnO film show a pronounced Bragg peak at 34.4 deg, as shown in Figure 5.1 b. This Bragg peak corresponds to the diffraction value of a c-plan-ZnO sample. Thus, the XRD data reveal a preferred c-plane crystalline orientation of the grains perpendicular to the substrate surface of both the intrinsic and Al-doped ZnO thin films. Using the Scherrer Equation [127]

$$G = \frac{\lambda_{x-ray}}{\Delta_{FWHM}(2\Theta)cos(\Theta_D)}, \tag{4.1}$$

the grain size G can be determined using the wavelength of the used x-ray source λ_{x-ray}, the FWHM-width of the rocking curve (given in 5.1b) and the Bragg-angle Θ_D. Thus, the grain size appears to be columnar with a roughly 200nm width and a value of roughly 300nm in height. The ZnO grains are thusin the range of the emission wavelength of ZnO in the material (i.e. divided by the ZnO refractive index).

Aluminium doping

Aluminium doping of the ZnO thin films is achieved by subsequent ion implantation of Aluminium into the as-grown intrinsic ZnO thin films. A combination of several ion energies ranging from 40 to 180 keV was used in order to ensure a homogeneous doping profile from 50 nm to 200 nm, as shown in Figure 5.1 c. The ion ranges were simulated with the Monte-Carlo program package SRIM [128]. Ion fluences ranging from $5 \cdot 10^{14}$ ions/cm^2 at 40 keV to $5.7 \cdot 10^{15}$ ions/cm^2 at 180 keV were used, yielding an Al-concentration of roughly 0.5 at.%.

4.1.2 Experimental setup

The ZnO thin films were optically excited using femtosecond laser pulses with a central wavelength varying in a broad spectral range from the near (0.8 μm) to the far-infrared(10 μm) spectral range.

Laser pulses at 810 nm, 1 kHz repetition rate, 46 fs duration and up to 0.7 mJ pulse energy were delivered from an chirped pulse amplification (CPA) Ti:sapphire laser system, while wavelength tunable near-infrared radiation between 1.2-1.6 μm (signal wave) and 1.6-2.8 μm (idler wave)

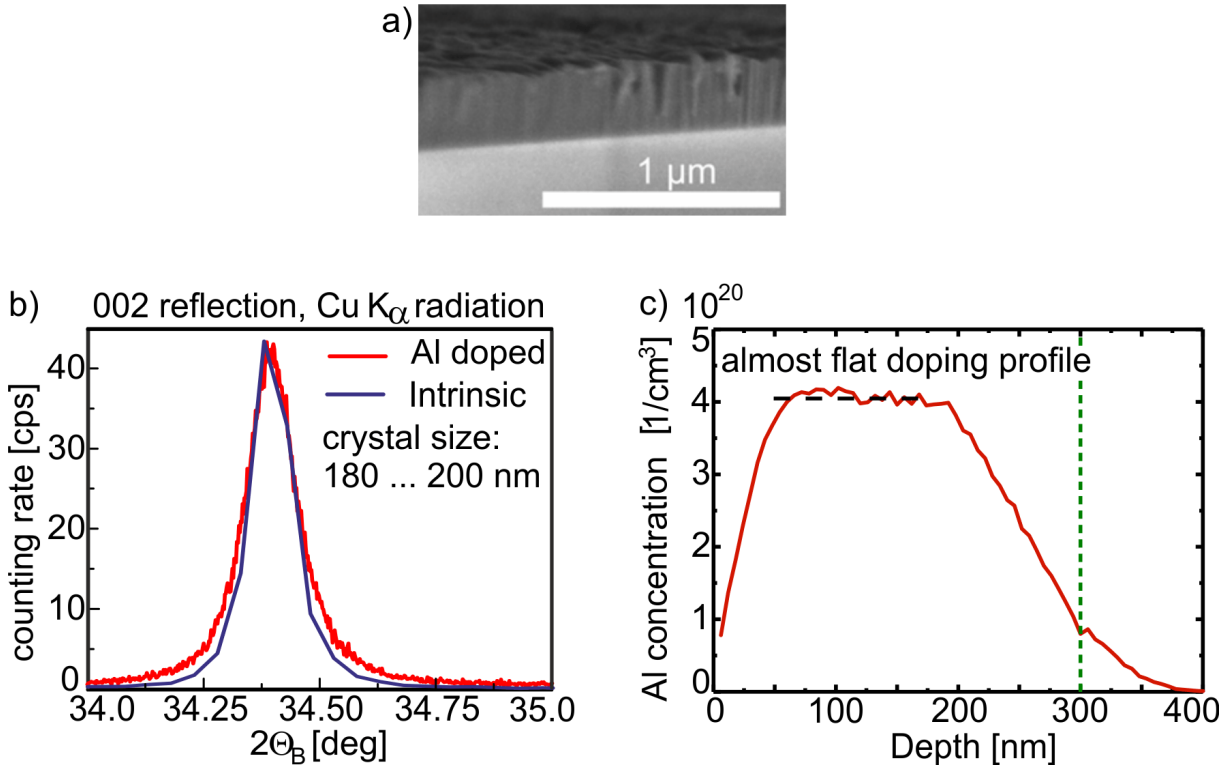

Figure 4.1: a)Scanning electron microscope image of the cross section of a 300 nm thick polycrystalline intrinsic ZnO thin film. b) X-ray diffraction (XRD) spectra from intrinsic and Al-doped ZnO thin films. c) Calculated implantation profile of Al in the ZnO thin film on top of a sapphire substrate using the Monte-Carlo program package SRIM. Multiple implantations with varying Al ion fluences $5 \cdot 10^{14}$ ions/cm^2 at 40keV, $6 \cdot 10^{15}$ ions/cm^2 at 70 keV, $2.2 \cdot 10^{15}$ ions/cm^2 at 130 keV, and $5.7 \cdot 10^{15}$ ions/cm^2 at 180 keV were used, in order to reach an almost homogeneous doping profile as a function of depth, resulting in a total fluence of $1 \cdot 10^{16}$ ions/cm^2 and roughly corresponding to an Al-concentration of 0.5 at.% in the ZnO film.

were generated in a commercial optical parametric amplifier (OPA, Light Conversion TOPAS). The parametric amplification of a white light seed was performed in multiple stages using Beta Barium Borat (BBO) nonlinear crystals pumped by a high power Ti:Sa femtosecond laser system. The pulse duration of the pulses delivered by the signal and ilder waves were 60-70 fs and 90-100 fs, respectively.

Femtosecond laser pulses generation in the mid infrared spectral range between 3 and 4 μm and in the far-infrared at 10 μm have been performed by noncollinear and collinear difference frequency mixing of the signal and idler waves in a potassium titanyl arsenate (KTA) and gallium selenide (GaSe) nonlinear crystal, respectively. In case of mid infrared pulses (3-4 μm) the 2-stage OPA was pumped with 5 mJ laser pulses having 1 kHz repetition rate and 35 fs duration. The OPA used to generated pulses in the far-infrared (10 μm) had 3-stages of parametric amplification which were pumped by a laser with 40 mJ pulse energy, 50 Hz repetition rate and 40 fs pulse duration[11]. The pulse energies and duration achieved by the DFG pro-

[11]The laser system providing the ultrashort laser pulses in the far-IR at 10 μm is available at the Advanced Laser Light Source, located at INRS-EMT, Quebec Canada

cess were up to 80 and 40 μJ and sub 100 fs in the case of mid and far-infrared laser pulses, respectively. The laser pulses were temporally characterized using SHG-autocorrelation and SHG-frequency optical gating (FROG) techniques (see Figure 4.2 a, c and e). The spatial characterization was performed by a CCD camera for wavelengths below 1 μm and using a knife edge technique above 1 μm (see Figure 4.3). The laser pulse spectra were measured by a grating spectrometer with a silicon detector (USB4000, OceanOptics), a broadband mid-IR spectrum analyser (Mozza Fastlite) and a home-made grating based monochromator with a nitrogen cooled HgCdTe-detector in the case of near, middle and far-infrared wavelengths, respectively. Figure 4.4 illustrates the experimental setup used to investigate the spectral NUV emission from polycrystalline ZnO thin films on sapphire substrates. Depending on the laser wavelength a λ/2-waveplate in combination with a thin film polarizer or two wire grid polarizer were used to adjust the laser power. The laser polarization was controlled by a broadband λ/4-plate or λ/2-plate. The laser pulses were focused with a spherical lens onto the sample at normal incidence. The emitted NUV light was collected in transmission geometry using proper collimating optics (f=25 mm lens, 36x reflective objective or 50x long working distance objective) and detected with a spectrometer (Ocean Optics USB 4000 UV-VIS). All experiments were carried out at room temperature and ambient atmosphere.

4.2 Three-photon absorption pumped stimulated emission in thin films

Polycrystalline ZnO thin films serve as well known sources of stimulated NUV emission when they are pumped by single photon excitation in the UV [45, 111, 112, 113, 114, 115, 116, 117, 118, 119]. Instead, roughly 50 fs long linear polarized pump pulses at 810 nm central wavelength in the near-IR were used in this experiment. According to the ratio of the intrinsic ZnO band gap (3.2 eV) and the used pump-photon energy (1.53 eV), carrier photo excitation requires a three photon absorption process to excite one electron from the VB to the CB [32, 129]. A f=50 cm lens has been installed to focus the laser pulses onto the film and a 36x reflective objective was used to collect the NUV emission from the film (experimental setup see Figure 4.4). The sample was placed out of focus where the beam diameter was roughly 0.6 mm in order to avoid laser induced damage of the ZnO thin film.

In the following paragraphs the properties of stimulated emission from polycrystalline ZnO thin films pumped by a three photon absorption process are investigated. Further results on the dependence of the threshold pump intensity of stimulated emission on the sample doping and the dependence of the three photon absorption coefficient on the laser polarization, especially the ellipticity, are presented as well.

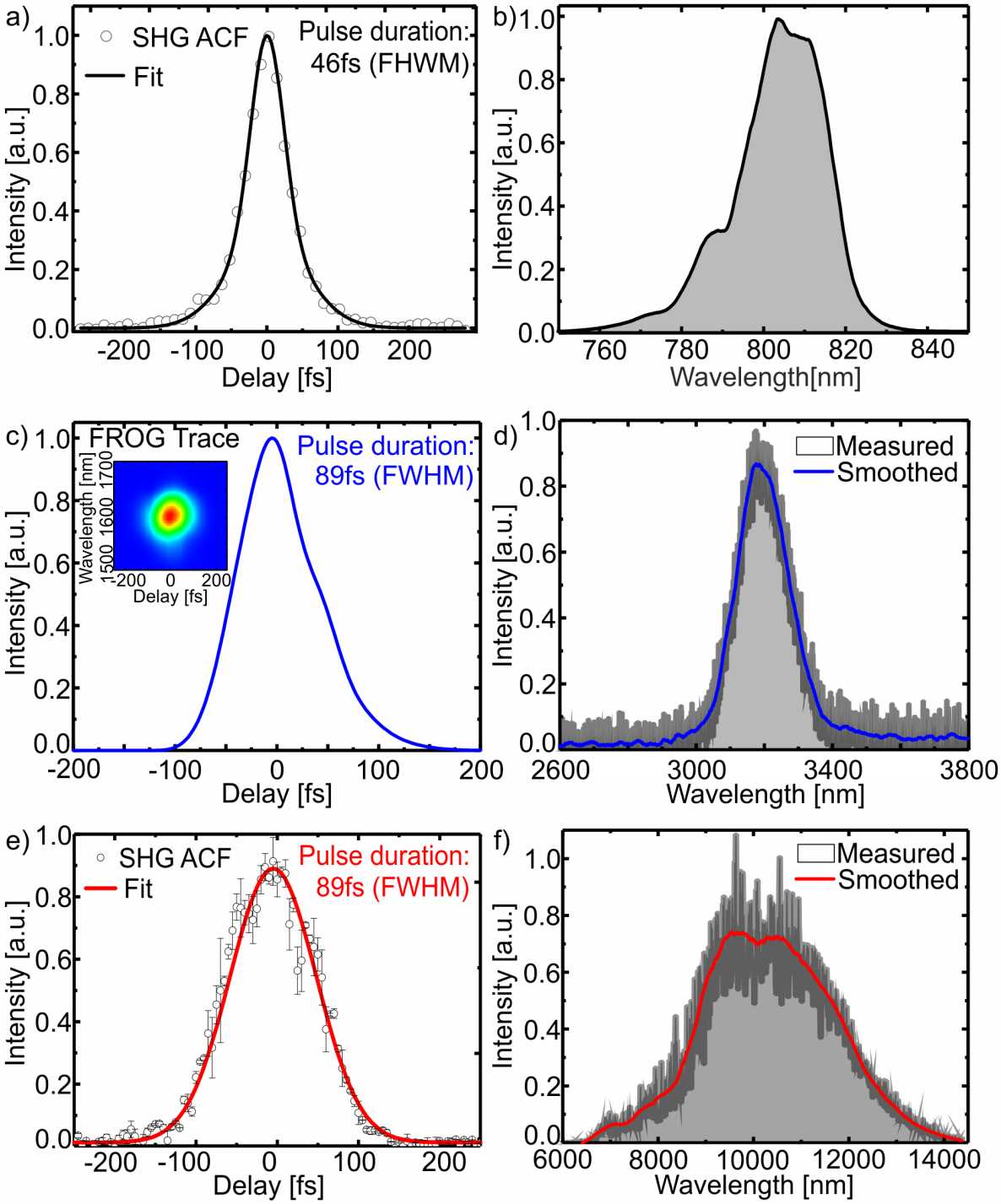

Figure 4.2: Laser pulse characterization. a) SHG autocorrelation and b) spectrum of 0.8 μm pulses. c) Reconstructed field intensity from a SHG-FROG measurement and d) spectrum of laser pulses centered at 3.2 μm. The inset in c) shows the measured FROG trace e) SHG autocorrelation and f) spectrum of laser pulses with a central wavelength at 10 μm.

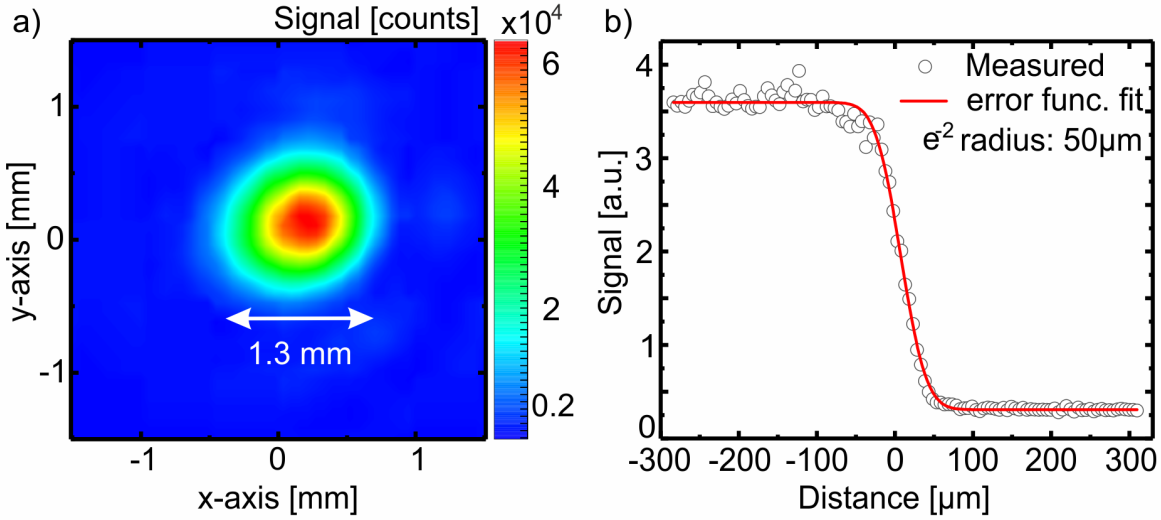

Figure 4.3: a) Beam profil of the focused laser with a wavelength of 0.8 μm, measured with a CCD camera. b) Knife edge scan trace of a 3.2 μm laser beam. The e^{-2} beam radius of 50 μm was determined by an error function (error func.) fit.

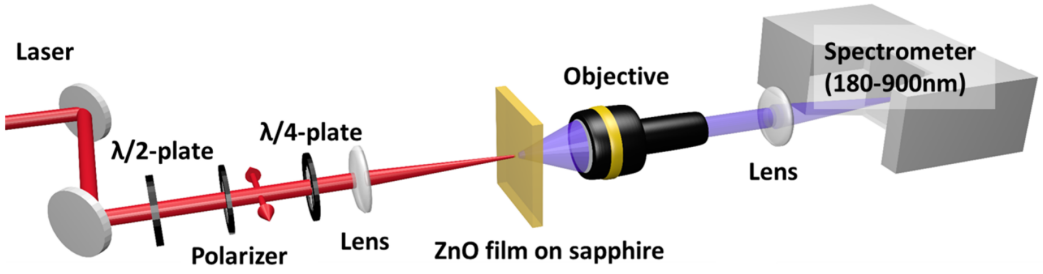

Figure 4.4: Experimental setup used to investigate optically excited polycrystalline ZnO thin films on sapphire substrates. Laser power attenuation was performed by a $\lambda/2$-plate in combination with a thin film polarizer or a pair of wire grid polarizers, dependent on the used laser wavelength. Polarization control of the laser field was performed by a $\lambda/4$-plate or $\lambda/2$-plate. The laser light was focused onto the thin film using a spherical lense. The NUV emission was collected, collimated and reimaged to the entrance slit of a spectrometer.

4.2.1 Influencing the laser threshold by free carrier doping

Figure 4.5 a, b show the NUV emission spectra measured from an intrinsic and Al-doped ZnO thin films (300 nm thickness, columnar grains with 200nm width) for pump intensities below ($I < I_{th}$), around the ($I = I_{th}$), and above the threshold ($I > I_{th}$) for stimulated emission, respectively. For low excitation intensity below the threshold two dominant emission bands, centered at 378 nm and 405 nm, arise in the emission spectrum. These lines originate from the spontaneous recombination of free excitions in ZnO at room temperatures [45, 111, 130] and second harmonic generation (SHG) of the pumping laser pulse in ZnO [125], respectively. Increasing the pump intensity, a third distinct line emerges between the emission lines of the excitons and

the SHG. With increasing pump intensity, this additional emission line shows a strong red-shift and a super-linear increase in intensity. Therefore, this third emission band is attributed to stimulated emission originating from an electron hole plasma (EHP) at high excitation densities, as these features match the well kown properties of an photoexcited EHP [45, 111, 113, 114, 115, 130].

In the following, focus the evolution of the spectral features attributed to excitons and stimulated (EHP) emission are explained in more detail. The generation of the second harmonic in ZnO thin films has been topic of intensive research [125] and will not be discussed here. In order to distinguish between the different contributions of the measured spectra, a sum of three Gaussian lineshapes was fitted to the measured data. The full width half maximum (FWHM) and the position of the emission maximum were directly obtained from this fit, the total yield was determined by spectrally integrating the contributions from the spontaneous excitonic and stimulated emission.

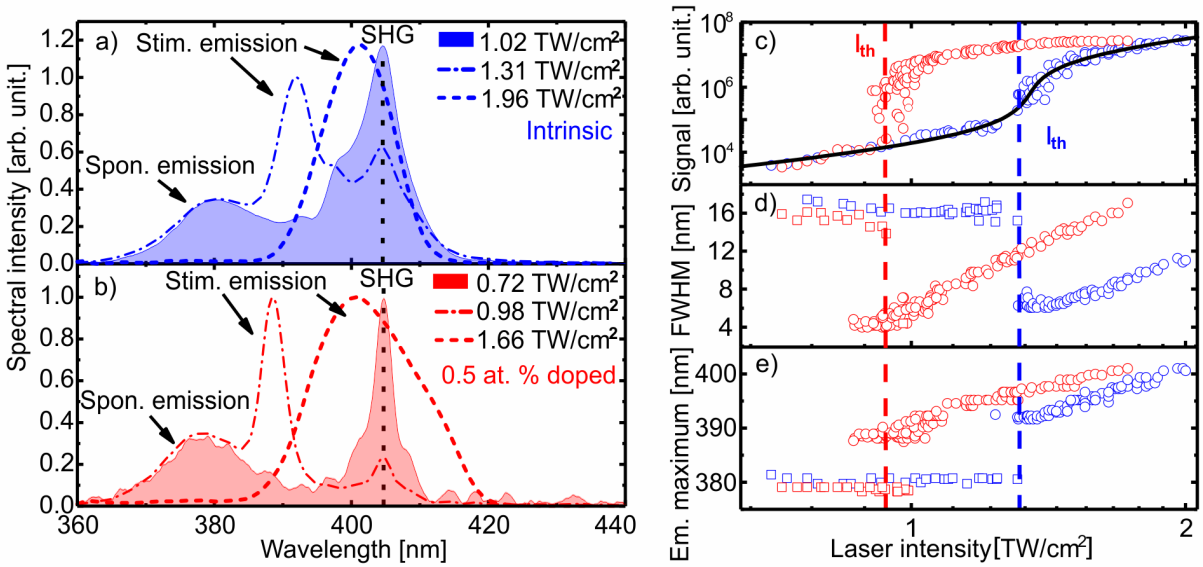

Figure 4.5: a) Emission spectra of intrinsic and b) 0.5 at. % Al-doped ZnO thin films for pump laser intensities below (solid line and filled area), close to (dash-dotted line) and above (dotted line) the stimulated emission threshold, respectively. The emission band at 405 nm corresponds to the second harmonic of the pump pulses. c) Integrated emission yield as a function of the pump laser intensity from experimental data in a,b (open dots) and simulation (gree and purple bands). Note, despite the assumed three-photon absorption the slope (i.e. power scaling) of the intensity dependent spontaneous emission deviates from the expected factor of 3 near the lasing threshold. d) Spectral FWHM and e) position of the spectral maximum of the emission of ZnO thin films, as function of the pump laser intensity for the intrinsic (blue) and 0.5 at. % doped (red) thin film ZnO sample, respectively. The blue and red dashed vertical lines mark the threshold intensity I_th, respectively. Data corresponding to excitons and EHP based emission are depicted by open squares and open circles, respectively.

The excitation laser intensity dependent evolution of the spectrally integrated emission yield, the spectral FWHM, and the position of the emission maxima for the intrinsic (blue) and 0.5

at.% Al-doped ZnO thin film samples (red) are shown in Figures 4.5 c-e. As expected an almost constant FWHM and position of the emission maximum of free excitons was observed, only the integrated yield increases with the pump intensity [112]. Close to the stimulated emission threshold, the yield, FWHM, and emission maximum show a abrupt change with increasing pump intensity, in agreement with previous experiments [45, 111, 115, 130]. The spectral integrated yield, shown in log-log representation, follows a linear trend for low pump powers, however the emitted NUV light increases rapidly by two orders of magnitude reaching the threshold intensity for stimulated emission. The FWHM of the PL emission peak is 15-17 nm for both the intrinsic and doped sample and nearly independent on the pump intensity. At the pump threshold intensity the emission peaks, resulting from stimulated emission, have a width of roughly 5 nm and are much narrower than the spontaneous PL. Increasing the pump intensities above the threshold, a strong broadening of the stimulated emission peak can be observed which is linked to the broadening of the excited carrier density dependent ZnO gain spectrum caused by an EHP and increasing temperature of the sample [32, 37, 131, 132, 133]. Here the doped sample shows a much stronger broadening effect compared to the undoped sample. The spectral positions of the emission maximum are constant and redshifted by more than 10 nm in the case of excitonic emission and stimulated emission in an EHP, respectively. The strong redshift due to band gap renormalization in an EHP are in agreement with previous experiments [30, 45, 111, 115, 130]. The vertical dashed lines indicate the threshold intensity when the stimulated emission from an EHP dominates the emission spectra. Thus the lasing threshold for intrinsic and doped thin film is 0.95 TW/cm^2 and 1.3 TW/cm^2,respectively. The super linear increase of the yield accompanied with strong spectral narrowing at the threshold pump laser intensity are characteristic for the onset of laser emission [134, 135].

The observed 1.4 times lower threshold and a more pronounced broadening of the emission spectra for the doped sample can be explained by the higher intrinsic carrier density in the conduction band (CB) for the highly n-type doped ZnO. Thus, less additional carriers have to be excited to reach the Mott density for EHP formation [30]. Additionally, the activated dopants block the low CB states and hence reduce the loss in the lasing process due to reabsorption [54]. Here it was excluded, that significant effects caused by a variation of the doping dependent band gap because of the minor difference of only a few tenth of meV for the intrinsic and the 0.5 at. % doped thin film [136, 137]. However, the qualitative evolution of the integrated yield, FWHM and the position of the emission maximum are similar below the threshold for both the intrinsic and Al-doped ZnO thin films.

Around the pump laser threshold, a steeper slope for the expected power dependence than $\propto I^3$ is obtained for the spontaneous emission yield as a function of the pump intensity, which is expected for a three photon absorption process. This deviation is a signature of stimulated emission already providing a significant contribution to the emission.

For a better understanding of the laser performance and especially the role of multiphoton excitation the photon emission yield was calculated as a function of the pumping intensity. The set of three coupled rate Equations 2.12-2.14 were solved, considering the temporal evolution of the photon number, density of hot and thermal electrons, respectively. In simulations the interband excitation rate was given by the three photon absorption coefficient as suggested by Versteegh et al. [32] instead of the rate given by the Keldysh formalism. Thus interband transition rate $\frac{dn_e^*}{dt}$ due to three photon absorption in Equation 2.12 becomes

$$\frac{dn_e^*}{dt} = \frac{\alpha_3}{3\hbar\omega_0} I^3 \tag{4.2}$$

with $\alpha_3 = \alpha_{3,A} + \alpha_{3,B}\left(1 + \frac{I^3}{I_S^3}\right)^{-1}$ with $\alpha_{3,A} = 0.5 \cdot 10^{-27}\, m^3/W^2$, $\alpha_{3,B} = 0.5 \cdot 10^{-27}\, m^3/W^2$ and $I_S = 0.2\,\mathrm{TW/cm^2}$. Free carrier absorption was neglected for 800 nm wavelength according to results shown in Figure 2.4. The calculated integrated photon yield is depicted as a function of the excitation intensity in Figure 4.5 c (solid line) and is in excellent agreement with experimentally measured numbers after a reasonable choice of the model parameters. The agreement provides not only confidence for the validity of the model it is also a further proof of lasing in the ZnO thin films.

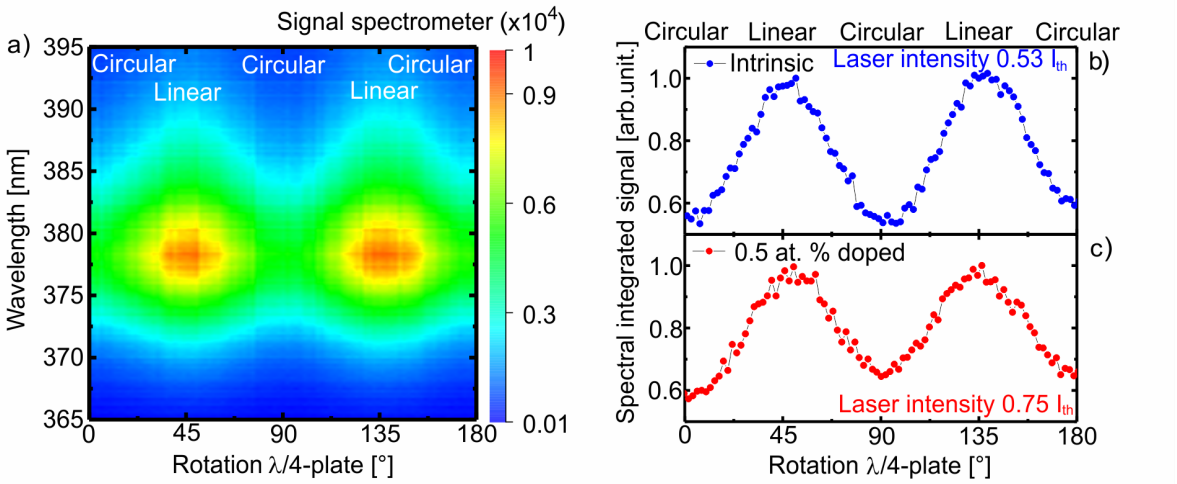

Figure 4.6: Ellipticity dependence of PL emission from ZnO thin films. a) Colour plot showing the emission spectra of an intrinsic ZnO thin film as a function of pump laser ellipticity for a constant pump intensity below the stimulated emission threshold in the spontaneous emission regime. b) Integrated emission yield for intrinsic and c) 0.5 at. % Al-doped ZnO thin films as a function of the pump laser ellipticity at an excitation intensity of 0.53 and 0.75 times the threshold, respectively.

4.2.2 Ellipticity dependence of pump process

This section is used to give insights in the dependence of the three photon absorption process on the laser polarization. Therefore, a $\lambda/2$ or $\lambda/4$-plate were installed in the experimental setup with the purpose to change the orientation of the linear laser polarization and to provide adjustable linear to circular polarization states of the pump laser, respectively. The XRD measurements shown in Figure 4.1 a confirmed that the c-axis of the micro-crystallites are preferentially oriented perpendicular to the surface of the substrate. Measuring the NUV emission spectrum as a function of the linear laser polarization orientation using a $\lambda/2$-plate shows no periodic modulations which may origin from a crystal c-plane symmetry defined absorption coefficient. Thus, any absorption anisotropy for linearly polarized pumping can be excluded.
However the influence of the pump laser ellipticity, controlled by a $\lambda/4$-plate, for three photon absorption in thin ZnO films is presented in Figure 4.6 for a pumping intensity below the pump threshold for stimulated emission in the spontaneous emission regime. For this intensity only the broad emission band around 380 nm is emitted from the ZnO thin film. Figure 4.6 b) and c) show a comparison of the ellipticity dependence for the spectrally integrated emission signal of the intrinsic and the Al-doped sample for the same pump laser intensity of $0.7\,\mathrm{TW/cm^2}$. Both ZnO samples, the intrinsic as well as Al doped ZnO sample reveal the strongest integrated emission for linear polarization and the modulation period is determined to occur with 90 degree (rotation angle of the $\lambda/4$ plate) with a pronounced minimum for the circular polarization. The ratio between the emission yield for linear and circularly polarized pump pulses is about 0.6. Comparing the ellipticity dependent PL yield, no substantial difference between the intrinsic and doping sample is observed, such that any impact of the Al doping and thus an increased density of free carriers can be excluded.
Figure 4.7 a shows the emission spectra as function of the rotation angle of the $\lambda/4$-plate while the pump intensity is fixed to 0.95 times the threshold intensity. As the $\lambda/4$-plate position determines the polarization state between linear and circular, the stronger emission for linear polarized pumping in agreement with the results for pure spontaneous emission in Fig. 4.6. Figure 4.7 b depicts the emission spectra obtained for linear (green) and circular (black) polarized pump pulses. While the broad emission of free excitons around 380 nm is observed for both polarizations, the stimulated emission peak at around 390 nm is only observed for linearly polarized pumping. This results suggest that the onset of stimulated emission can be controlled by adjusting the pump beam ellipticity via tuning the photo generation rate. Both the onset of stimulated emission (Fig. 4.7) and the intensity of excitonic emission (Fig. 4.6) is linked to the number of excited carriers. Thus, the shown results indicate that the generation of excited carriers i.e. the absorption of the pump pulse energy is strongly influenced by the polarization of the pump laser. For both ZnO samples, an enhanced absorption for linearly polarized light compared to circular polarization was observed.

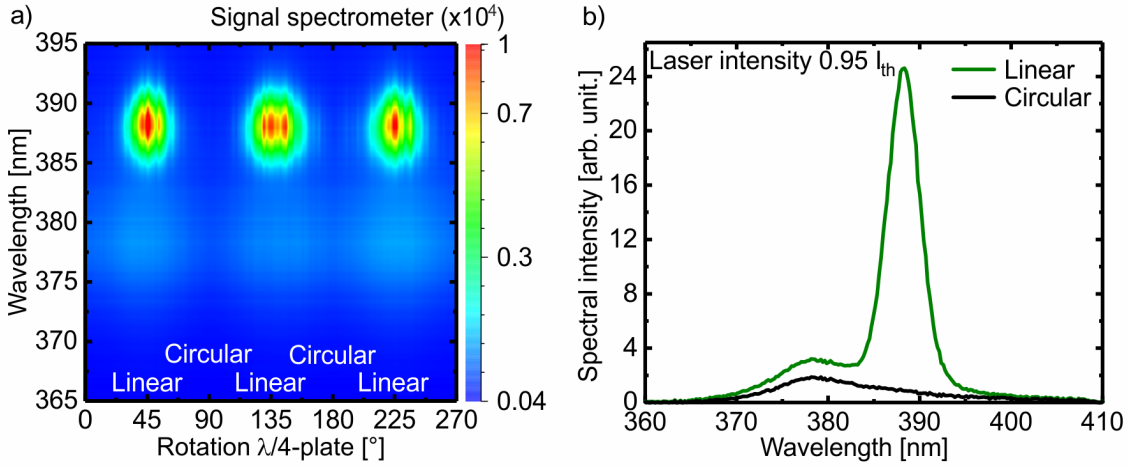

Figure 4.7: a) Contour plot showing the emission spectra of the intrinsic ZnO thin film as a function of the pump laser ellipticity for a pump intensity close to the stimulated emission threshold. b) Emission spectrum of intrinsic ZnO thin film for linear and circular pump laser polarization for a pump intensity close to the stimulated emission threshold of 1.25 TW/cm^2.

Surprisingly, a review of previous studies on the dependence of multiphoton absorption processes in solids on the light ellipticity contradict the above mentioned results for ZnO thin films. Temnov *et al.* [138] suggested that for low order N-photon absorption with N<5 circularly polarized light is more effectively absorbed than linearly polarized light, while for a N=6 photon process linearly polarized light results into a higher excited carrier density. These findings are confirmed by experiments on laser material processing using linearly and circularly polarized laser pulses [139, 140]. Additionally, Liu et al. [141] observed a dependence of the linear and circular laser induced damage threshold on the numerical aperture (NA) of the focusing optics in the experiment. Gawelda et al. [142] investigated the laser polarization dependent generation of filaments in dielectrics and determined a higher critical power to initiate a filament using circularly polarized pulses compared to linearly polarized ones. The results from Du et al. [143] showing the same threshold intensity for laser induced breakdown in dielectrics using linearly or circularly polarized laser beams is thus in contrast to all reported results. These previous investigations, besides their very different experimental conditions, do not allow distinguishing between the polarization dependence of the nonlinear absorption and the polarization dependence of the subsequent processes such as self-focusing or avalanche ionization.

In contrast, nonlinear propagation effects like self-focusing can be safely excluded here due to the small thickness of the ZnO films. As shown in Figure 2.4 avalanche ionization can be neglected for the applied experimental parameters. Thus, the carriers are excited via three-photon absorption only. Therefore, the presented experimental method, using thin films, provides direct access to the polarization dependent three-photon absorption coefficient. As presented in Figure 4.6 the ratio of the spectrally integrated spontaneous emission for linearly and circularly

polarized pump pulses can be estimated to be roughly 1.8. Further for ZnO thin film experiments with different pulse intensities revealed that this ratio is also independent of the pump intensity.

In order to understand the observed ratio, a theory developed by Arifzhanov et al. [144] was used. The authors investigated the polarization dependence of the three-photon excitation rate in bulk semiconductors theoretically and experimentally. Their study revealed that the three-photon absorption rate for linear and circular polarization varies as a function of the ratio $3\hbar\omega/E_g$, where E_g is the band gap of the material and $\hbar\omega$ is the pumping photon energy. Using this approach, the theoretical ratio of the three-photon absorption coefficients between linear and circular polarized light is approximately 1.5 for the conditions of this study of ZnO. This ratio is directly related to the measured ratio of the integrated spontaneous emission yield of 1.8 (Fig. 4.6) and thus is in good agreement with the value determined using the approach of Arifzhanov et al. [144]. The observed higher three photon absorption rate for linearly polarized light can be explained by the higher number of allowed optical transitions for a given band structure including the contributions of higher conduction band states [144, 145].

The integrated yield of the stimulated emission spectra shown in Figure 4.7 b yields a ratio of roughly 5.1 between linearly and circularly polarized pumping. Solving the rate equations 2.12-2.14 for an intensity of 0.95 I_{th}, a ratio for the stimulated photon yield of 4.7 between linear and circular pumping was obtained, if a three photon absorption coefficient $\alpha_{(3,lin)}$ of roughly $0.5 \cdot 10^{-27}\, m^3/W^2$ for linear radiation and $\alpha_{(3,circ)} = (1/1.8) \cdot \alpha_{(3,lin)}$ for circular polarization, respectively, was assumed in accordance to the results for spontaneous emission. Thus, an excellent agreement between experiment and simulation is obtained proofing that the three photon absorption coefficients for circularly polarized light can be directly determined from the absorption coefficient for linear polarized light and the ratio of the photoluminescence given in Figure 4.6 b and 4.7 b.

In conclusion femtosecond near-infrared laser pulses of 800 nm central wavelength can be used to induce stimulated emission from polycrystalline ZnO thin films. The onset of an emission dominated by stimulated recombination processes was determined by a rapid increase of the emission and spectral narrowing of the emission spectra when the threshold pump intensity was reached. A reduced, pump intensity threshold by a factor 1.4 was reported for 0.5 at % doped ZnO thin films compared to intrinsic ZnO thin film. Furthermore, the dependence of the three photon absorption (TPA) coefficient on the laser ellipticity was determined. With a factor of 1.8 when the laser polarization is circularly instead of linearly polarized.

4.3 Strong off-resonance excited ZnO thin films

So far, stimulated emission in intrinsic and Al doped polycrystalline ZnO thin films was investigated upon pumped by a three photon absorption process. In the following section far off-resonance excitation of ZnO thin films using strong light fields is investigated. The onset of stimulated emission from ZnO thin films pumped in the tunneling regime will be demonstrated not only in spectral but also in the time domain (Section 4.3.1 and 4.3.2). A quantitative comparison of light absorption from the multiphoton to the tunneling regime are presented in Section 4.3.3, by exploiting the fact that the absorption and emission process is decoupled in time by roughly one picosecond due to carrier thermalization. Thus, the onset of stimulated emission could be used as an experimental probe to monitor the density of excited electrons.

4.3.1 Strong off-resonance pumped random lasing

Figure 4.8 a shows the measured emission spectra from an intrinsic ZnO thin film (300 nm thickness, 120 nm grain width) far off-resonance irradiated by femtosecond laser pulses at 3.2 μm for three different pump laser intensities. The spectral evolution as a function of the mid-IR laser intensity is similar to the spectra observed upon TPA pumping, shown in Figure 4.7. For low pump laser intensities below the laser threshold two distinct peaks at 355 nm and around 380 nm are visible. The peak at 380 nm originates from the spontaneous emission due to the recombination of free excitons [45, 111, 130] and the peak at 355 nm corresponds to the 9^{th} order harmonic of the 3.2 μm pump laser, respectively. In the experiments higher order harmonics up to the 15th order located at 213 nm have been measured, which denote the detection limit of the used spectrometer (see Figure E.1 in the Appendix E). Increasing the pump power, a new narrow emission band evolves around 385 nm. This peak is rapidly growing, broadening and red shifting with increasing pump laser intensity and origin from stimulated recombination in an EHP [45, 111, 130]. At highest pump intensities of 0.37 TW/cm^2 the stimulated emission peak originally at 385 nm shifts up to 400 nm and its signal intensity dominates the measured spectrum. At such high pump intensities the emission resulting from spontaneous emitted free excitons and harmonic generation become negligible in comparision to the stimulated emission. Further insight on the dependence of the NUV-emission spectra on the laser intensity are depicted in Figure 4.8 b-d. It is shown, the output yield (upper panel) given by the spectrally integrated signal as well as the full width of half maximum (FWHM) (middle panel) and spectral redshift (lower panel) for the peaks resulting from spontaneous free exciton emission and stimulated emission in an EHP as a function of the pump intensity. The vertical red line define the pump threshold intensity $I_{th} = 0.275\,\text{TW/cm}^2$ (0.14 V/Å), when stimulated emission starts to dominate the emission spectra. For pump intensities below the threshold, the yield

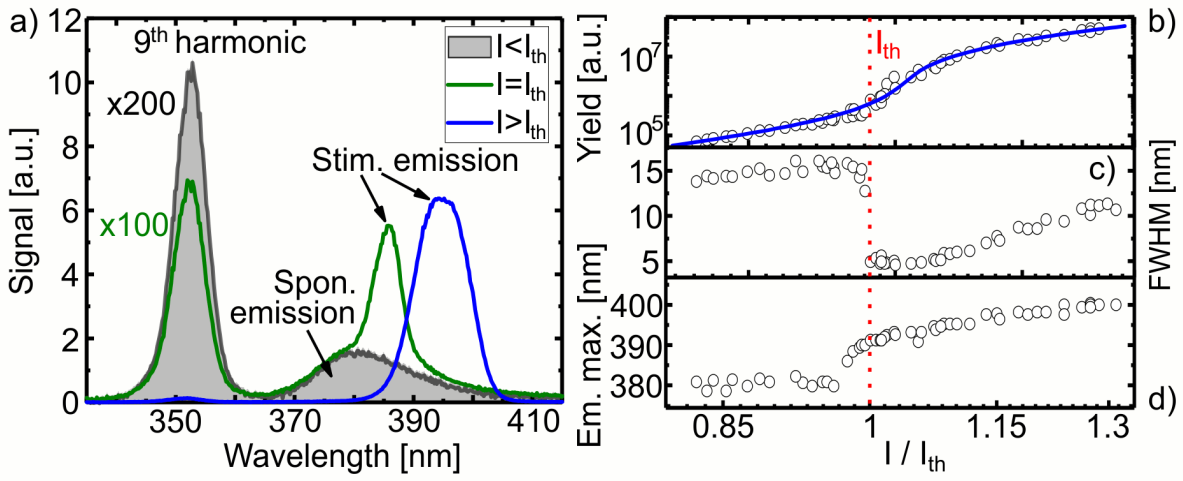

Figure 4.8: a) NUV Emission spectra from ZnO thin films strong off resonance excited by 3.2 μm femtosecond laser pulses. The black line shows the calculated emission yield as a function of the pump intensity using the coupled rate equations 2.12-2.14. b)-d) Spectrally integrated signal (yield), FWHM and the spectral maximum of the emission, respectively. The red line highlights the pump threshold intensity when stimulated emission dominates.

follows a linear trend in a log-log-representation. When the threshold intensity is reached the yield of the emission increases abruptly. Calculations using the rate equations 2.12-2.14 with given parameters, reproduce the lasing emission as a function of the laser intensity perfectly, as depicted by the blue line in Figure 4.8 b. Note, Figure 4.9 reveals a strong pump laser spot size dependence of the pump threshold intensity I_{th}. Please not that this feature was not covered by the simulations. The linewidth from an EHP based stimulated emission shows with 5-7 nm a much narrower FWHM compared to the 15-17 nm width of the free exciton emission spectra. Increasing the laser intensity above the threshold value leads to a broadening of the stimulated emission spectra from 5 nm to 12 nm, as depicted in Figure 4.8 c. This observation can be understood by the broadening of the carrier density dependent gain spectra and a heating of the ZnO gain material [32, 37, 131, 132, 133]. The spectral position of the emission peak maxima is constant below the threshold intensity value as shown in Figure 4.8 d. This is indeed indicative for an exciton based emission process [30]. For increasing pump intensity values above the threshold the stimulated emission peak shifts from 390 to 400 nm (redshift) due to band gab renormalization in an EHP excited in ZnO [32].

Note, the emission spectra as well as the pump intensity dependent spectral evolution due to an excitation using three photon absorption ($\frac{\hbar\omega_0}{E_g}$>2) shown in Figures 4.5 a, b and the far off resonance excitation process ($\frac{\hbar\omega_0}{E_g}$>8) shown in Figure 4.8 feature an identical behaviour. Thus, it can be assumed that laser emission was detected caused by strong field excitation using femtosecond laser pulses at 3.2 μm. The Keldysh parameter for this excitation conditions γ (Eq. 2.3) is 0.9 and thus excitation of the electrons is performed predominantly by tunneling excitation. Figure 4.9 depicts the lasing thresholds as a function of the excitation spot size when 3.2 μm

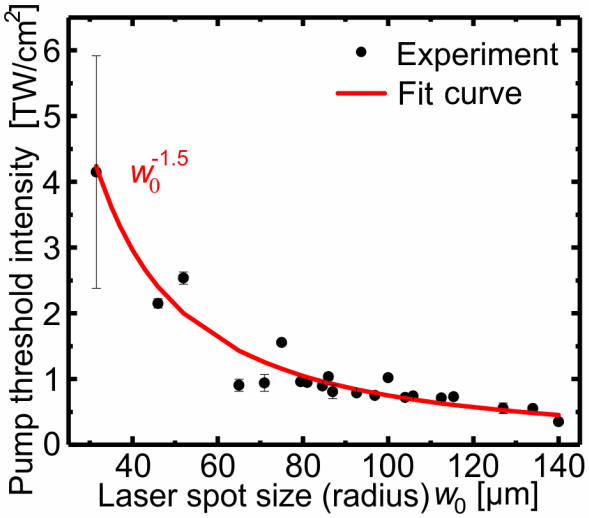

Figure 4.9: Dependence of the pump threshold intensity to observe stimulated emission from ZnO thin films on the excitation laser spot size. The black circles are the experimentally determined values and the red line depicts the result of a non-linear fit resulting in a $I_{th} \propto w_0^{-1.5}$ dependence.

pump pulses are used for excitation. The lowest threshold pump intensity of 0.27 TW/cm^2 was determined for a spot size radius (determined at e^{-2} of its maximum) of 137 μm. Decreasing the radius gradually to 31 μm results in an increase of the threshold pump intensity up to a value around 4 TW/cm^2. The large error bar at 31 μm radius is the result of four independent measurements on different positions on the sample. No dependence of the lasing onset on the sample position was measured except the smallest one. This highlights that the threshold dependsd on the pump laser spot size. The threshold intensity dependence on the spot size radius w_0 follows a $w_0^{-1.5}$ relation. A w_0^{-1} and w_0^{-2} dependence describe the light amplification onset threshold in media without (ASE) and with scattering centeres (random lasing) [146]. The measured decrease in laser threshold intensity as a function of an increasing pump spot size and a minimum threshold point size can be seen as a strong indication that both random lasing and ASE are taking place. However, no clear distinction between ASE or random lasing can be made [146, 147, 148].

4.3.2 Time resolved lasing process

To gain a deeper insight in the nature of the stimulated NUV emission from ZnO thin films time resolved measurements were performed using a frequency upconversion method. Polycrystalline ZnO thin films were irradiated with femtosecond laser pulses with a central wavelength at 3.2 μm to determine the dynamics of the NUV emission. The intensity of the laser was adjusted using a pair of wire grid polarizers (WG) before the laser was focused with a f=10 cm CaF_2 lens onto the thin film sample, normally to the sample surface. The ZnO emission was collected and collimated using a 50x long working distance objective (MO). As the temporal dynamics of the emission was measured using an upconversion method [149], the ZnO emission was overlapped with a time delayed 60 fs long laser pulse centered at 0.8 μm in a 200 μm thick

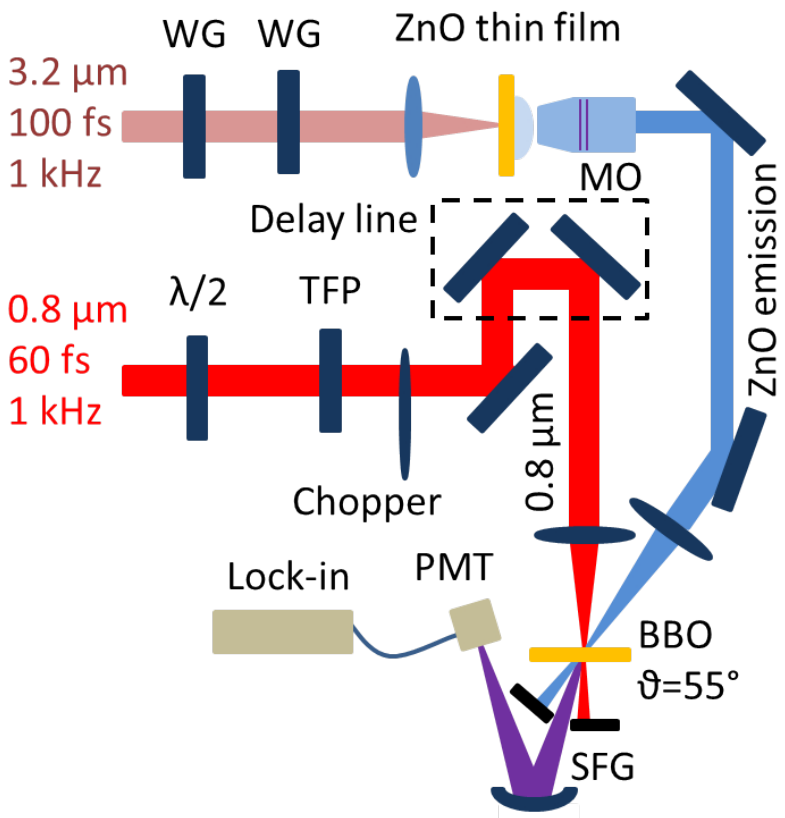

Figure 4.10: Upconversion setup used to determine the temporal evolution of the NUV emission from polycrystalline ZnO thin films on sapphire. The ZnO thin film was excited by mid-IR laser pulses at 3.2 μm. The laser power was adjusted by a pair of wire grid polarizers (WG) before the light was focused onto the film using a f=10cm CaF_2 lens. The NUV emission from the film was collected and collimated by a 50x objective. The femtosecond laser pulses at 0.8 μm used to upconvert the NUV emission were power attenuated using a λ/2-plate and a thin film polarizer (TFP), temporally delayed in respect to the mid-IR pulse by a delay line and overlapped with the NUV emission in a BBO crystall. The upconverted photons were refocused by a spherical mirror to a photomultiplier tube (PMT) whose signal was processed by a Lock-In amplifier.

type II BBO crystal (θ=55degree) with the purpose to generate the sum frequency (SFG) signal, which is shown in purple in Figure 4.10. The 800 nm laser (red in Fig. 4.10) was power attenuated using a combination of a λ/2-plate and a thin film polarizer. Furthermore, the 800 nm pulsed laser was temporally delayed in respect to the 3.2 μm excitation pulse (light purple in Fig. 4.10) using piezo-stage (Smaract) based delay line and a retroreflector (Newport). To achieve a high conversion efficience, the NUV emission as well as the 0.8 μm laser was focused into the nonlinear BBO crystal. The SFG signal at roughly 266 nm was refocused by a concave Aluminium mirror into a photo multiplier tube whose signal was detected with a Lock-In amplifier.

Figure 4.11 a shows the temporal dynamics of the ZnO emission when the thin film sample is exposed to femtosecond mid-IR laser pulses at 3.2 μm of different pump intensities. The upconversion of the high harmonic signal was used to calibrate the zero time delay. Note, that the broadening of the time resolved high harmonic signal is resulting from the non-collinear geometry of the upconversion setup [150]. For excitation intensities below the lasing threshold I_{th} only a slow decaying signal was measured with a characteristic time constant of the decay of roughly 110ps. This is indeed in very good agreement with previous measured spontaneous decay rates of ZnO [37, 93, 94]. At the lasing threshold a fast decaying signal appears superimposed to the slower spontaneous emission. This fast decaying signal is rapidly growing and its onset seems to appear earlier in time with increasing the pump intensity. Due to the short duration of 2-3 ps,

this signal can be attributed to the stimulated emission process in ZnO [41]. The change from a slow to a fast decaying dynamics occurs at the threshold for stimulated emission, as it was determined by analyzing the power dependence of the emission yield and width. Conclusively, these time-resolved measurements are an additional evidence for the onset of laser emission from polycrystalline ZnO thin films due to optical excitation with far off-resonance light in the tunnel regime.

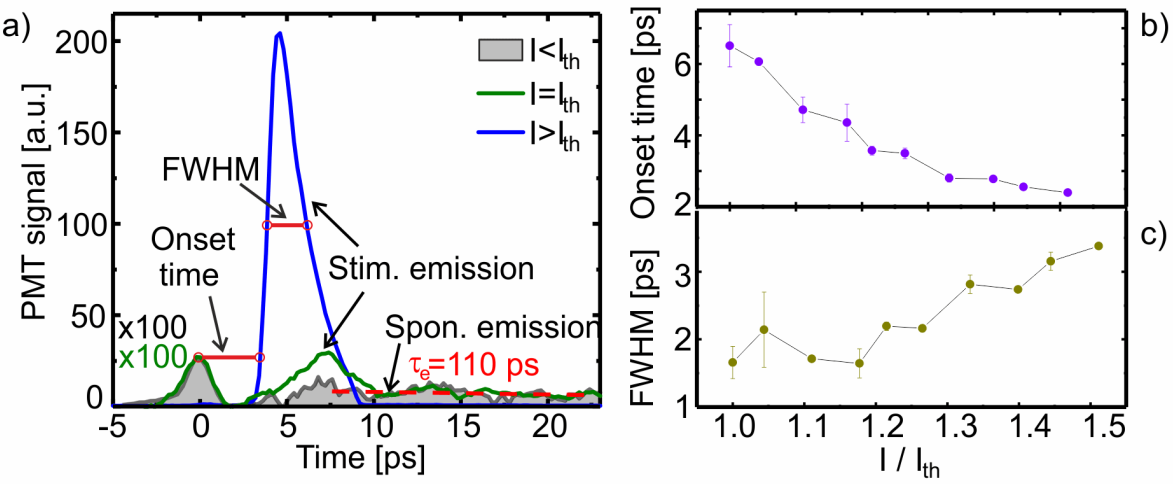

Figure 4.11: a)Termporally resolved NUV emission from ZnO thin films after strong off-resonance excitation using laser pulses at 3.2 μm. The signal at t=0 is the upconverted high harmonic signal. b) Laser intensity dependent stimulated emission onset time and FHWM.

Figure 4.11 b and c depict the excitation intensity dependent onset time and full width half maximum (FWHM) of the stimulated emission signal, respectively. The onset time is defined as the time difference between t=0 and the time delay when the signal reaches 1/e of it maximum value. This onset time drops from 6 to 2.4 ps when the the pump laser intensity is increased by a factor of 1.5 above the lasing threshold while the FWHM width of the stimulated emission peak increases slowly from 1.6 to 3.5 ps. The decreasing onset time of lasing and increasing FWHM, respectively, were qualitatively confirmed by lasing simulations using the rate equation model. The decrease of the onset of lasing with increasing pump intensities can be explained by an accelerated thermalization of the carriers. The increase in the NUV laser pulse duration is associated with a higher carrier density in CB leading to a longer time period, which is required to depopulate the carrier inversion until the transparency condition is reached. Recently, temporally resolved random lasing in ZnO nanopowders pumped by a three photon absorption process has been reported and confirmed by Tian *et al.* [151]. The lasing onset time and duration have been determined to be 7 and 3 ps, respectively [151]. As the temporal lasing emission characteristics originating from ZnO powders and ZnO thin films in this work coincide, this strongly indicates that random lasing is a present feedback mechansim in both samples. Beside nanopowders and thin films, nanowires have been used to realize nanoscale laser devices. As

explained on page 17, due to its geometry, nanowires form a waveguide resonator leading to Fabry-Pérot lasing if sufficient pumping is applied. The dynamics of individual nanowire lasers have been extensively studied and an onset time of 1 ps and emitted pulse width (FWHM) of roughly 10 ps have been reported [41]. While the lasing duration in ZnO nanowire lasers is similar to the measured values in thin films the onset time of lasing in ZnO thin films is larger by a factor 3.5. It is assumed that the extended onset duration is linked to the feedback mechanism.

4.3.3 Contributions of intra- and interband absorption processes

The results shown so far were obtained using very different experimental parameters, such as gain material, pump wavelength and excitation mechanism. Stimulated emission was achieved in intrinsic as well as Al-doped ZnO thin films. The pump conditions were varied in a wide wavelength range from 0.8 to 3.2 μm, leading to different electron excitation mechanism such as multiphoton and tunneling, respectively. Additionally the pump laser spot size on the sample was varied in the experiments which dramatically affected the pump conditions (see Figure 4.9), because the resonator feedback is caused by random path ways and single pass gain. Furthermore, it was shown on page 14 that the laser pulse duration strongly affects the electron intraband process and thus the number of excited electrons (Fig. 2.5).
The next paragraph highlights results on the investigation of the wavelength dependent threshold pump intensity. In order to enable a comparison of the results obtained with laser pulses in the different spectral regions from near-IR (1.2 μm) to far-IR (10 μm), the systematic variations in the experimental parameters were minimized as much as possible. First, the same intrinsic ZnO thin film sample (300 nm thickness, 120 nm grain size) was used for all measurements, second the pump laser spot size on the sample was fixed to a radius of 170 μm and the pulse duration varied only from 65-100 for near-IR pulses and 90-140 fs for pulses in the mid- to far-IR spectral range. Figure 4.12 depicts measured NUV-emission spectra from the intrinsic ZnO thin film excited with femtosecond laser pulses at 1.5 μm (Figure 4.12 a), 2.4 μm (Figure 4.12 b), 3.75 μm (Figure 4.12 c) and 10 μm (Figure 4.12 d) for three distinct pump intensities. The characteristics of the spectral evolution of the ZnO emission is identical independent of the pump wavelength. For low pump powers a broad emission around 380 nm is detected (orange filled area). Reaching the threshold pump intensity a narrowband peak at around 390 nm appears which increases rapidly and redshifts when the the pump power is increased. In Figure 4.5 c-e and 4.8 b-d an exemplary detailed quantitative analysis of emission yield, FWHM and redshift as a function of the pump intensity was given for 0.8 μm and 3.2 μm pump wavelengths, respectively. It should be noted that regardless of the pump wavelength, the spectral development as a function of the pump laser intensity is identical for the pump wavelength between 0.8 and 10 μm, which shows that laser emission in polycrystalline ZnO thin films can be achieved for a huge pump wavelength range.

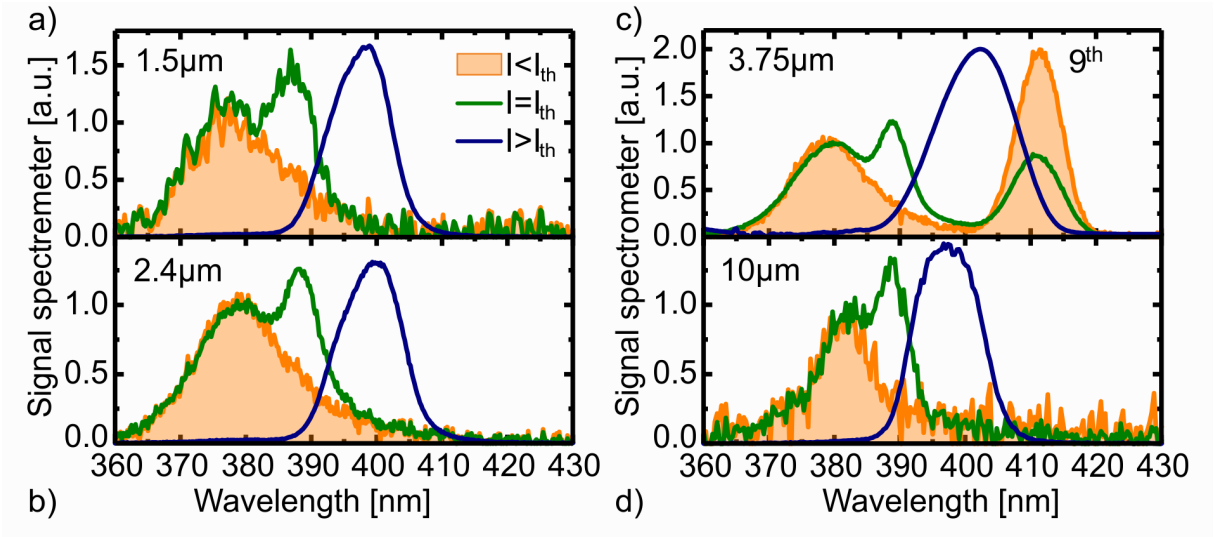

Figure 4.12: Emission spectra from a intrinsic ZnO thin film pumped below (orange), roughly at (green) and above (blue) the lasing pump threshold. The femtosecond laser pulses used to the excite the material had there central wavelengths of a) 1.5 μm, b) 2.4 μm, c) 3.75 μm and d) 10 μm. All emission spectra reveal an almost identical development of the spectral lineshape as a function of the pump laser intensity.

Figure 4.13 depicts the experimental (blue dots) and simulation (black line) results on the wavelength dependence of the threshold pump intensity for stimulated emission in intrinsic ZnO thin film. Increasing the pump wavelength from 1.2 to 2 μm the threshold pump intensity increases from 0.3 to 0.55 TW/cm^2. Further increasing the wavelength leads to a continuous decrease of the threshold pump laser intensity for stimulated emission. While for pump wavelengths between 3 and 4 μm the determined laser intensity was between 0.3 and 0.2 TW/cm^2, it was only 0.13 TW/cm^2 for a pump wavelength at 10 μm in the far-IR. The shown threshold intensity values are corrected in respect to the wavelength dependent reflection losses occurring on the air-film interface. To obtain a deeper understanding of the observed wavelength scaling of the lasing threshold and thus the wavelength dependent absorption in ZnO, simulations were performed using the coupled system of rate equations (Eq. 2.12-2.14) was solved using parameters given there and electron scattering time of 5 fs. Furthermore, it was assumed that a threshold carrier density of $2 \cdot 10^{25}$m^{-3} electrons in the CB enables negative absorption, i.e. optical gain [32, 37]. The excitation process occurs via interband transitions and impact ionization, subsequent free carrier absorption and is temporal decoupled from the emission process. Since the thermalization takes much longer than the duration of the laser pulse, only Equation 2.9 was considered to estimate the excited electron density as a function of the laser wavelength and intensity. In addition, the threshold carrier density of $2 \cdot 10^{25}$m^{-3} represents a universal quantitative parameter of the semiconductor active medium, which is independent on the geometry or structure. Therefore, in performed wavelength dependent simulations the threshold pumping intensity was determined as the value when the carrier density in the conduction band reaches $2 \cdot 10^{25}$m^{-3} by the end of the pump pulse. This is in fact one necessary condition to achieve

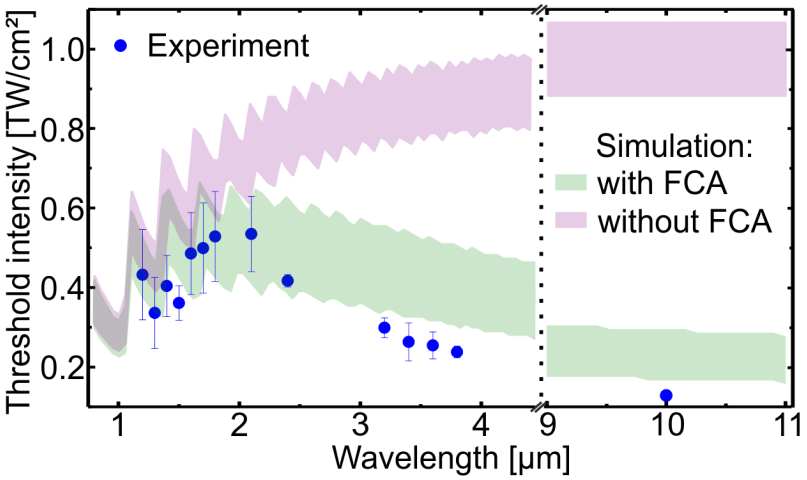

Figure 4.13: Pump laser threshold intensities to achieve lasing in a intrinsic ZnO thin film as a function of the pump laser wavelength (blue dots). The green and purple band depicts the simulated intensity with and wihtout including free carrier absorption, respectively, which has to be be applied to excite $2 \cdot 10^{25}\,1/\mathrm{m}^{-3}$ electrons and correspondingly to the provision of gain in the ZnO material. For calculations the coupled system of rate equations (Eq. 2.12-2.14) was solved using parameters given there and electron scattering time of 5 fs.

lasing, but obviously not sufficient because the threshold is also determined by the interplay between losses and gain.

The green and purple band in Figure 4.13 depicts the theoretically calculated pump threshold intensities in the upper and lower limit of experimentally used pulse durations of 60 and 150 fs with and without free carrier absorption (FCA). While The measured wavelength dependence of the threshold pump intensity of ZnO thin films coincide qualitatively well with the simulated values taking FCA into account the calculations without free carrier absorption deviate significantly. Thus, the initial increase of the threshold pump intensity between 0.65 and 0.9 $\mathrm{TW/cm}^2$ can be understood in accordance to the multiphoton absorption picture of light. Increasing the laser wavelength (i.e. lower the photon energy) leads to an increasing number of excited photons needed in order to maintain energy conservation and overcome the band gap. Comparing the simulated threshold pump intensity in the case with and without taking impact excitation of electrons into account, reveals that there is no significant influence of FCA for pump wavelengths below 1.2 μm. As shown in Figure 2.2 a for wavelengths longer than 1.5 μm and 0.5 $\mathrm{TW/cm}^2$ pump intensity the tunneling become more likely to be responsible to excite an electron instead of multiphoton excitation. This leads to the fact that excitation rate starts to become less wavelength dependent. The lowering of the threshold pump intensity for longer wavelengths are thus caused by additional intraband supported interband excitations via the field driven electron impact excitation process which scales quadratically with the laser wavelength (see Section 2.1.2). Best agreement between the experimentally measured and theoretically determined values was achieved using 5 fs electron-electron scattering time. Note, these results demonstrate that lasing in semiconductors can be achieved with an arbitrary pump wavelength if the the laser pulses are intense and short enough to initiate tunneling excitation and on the other hand avoid material damage as a consequence of an avalanche excitation process, respectively.

In conclusion ZnO thin films were irradiated with mid-IR femtosecond laser pulses at 3.2 μm,

according to the Keldysh theory (γ=0.9) excitation happens predominantly via electron tunneling from the VB to the CB. The NUV emission was distinguished by a abruptly growing and spectral narrowing signal when a threshold pump intensity was reached. This coincides with the spectral evolution already observed for near-infrared pumping at 0.8 μm. Furthermore, time resolved measurements, showed a transition from slow to fast decaying dynamics occurring at the threshold pump intensity proving the onset of laser emission. Experiments using different pump laser spot sizes (beam radius w_0) revealed a exp(-1.5·w_0) dependence of the laser threshold. The spot size dependent lasing threshold in combination with measured emission dynamics, indicate that random lasing and ASE are the responsible lasing mechanism in polycrystalline ZnO thin films. Finally the lasing threshold was investigated as a function of the pump laser wavelength in a wide spectral range from 1.2 to 10 μm corresponding to Keldysh parameters from 2.3 to 0.4, respectively. This spectral region thus covered the transition from multiphoton to tunnel excitation regime. The fact, that the measured wavelength dependence is in agreement with the Keldysh-Drude excitation model (see Section 2.1.3) highlights the importance of free carrier absorption for long laser wavelengths.

4.4 Conclusion

This chapter investigated stimulated emission from ZnO thin film samples optically pumped in the multiphoton absorption as well as in the tunneling regime. Using femtosecond laser pulses at 0.8 μm, the influence of the material doping and the laser ellipticity on the pump threshold intensity was investigated. The lasing threshold is reduced by a factor 1.4 when the material is doped with 0.5 at % Aluminium atoms. The three photon absorption coefficient is by a factor 1.8 lower for circular compared to linear polarization. A simple method based on the detection of the ellipticity dependent photoluminescence from thin films was introduced allowing to determine the three photon absorption coefficient for circular polarized light. Further random lasing and ASE in ZnO thin film upon far-off-resonance excitation by strong mid-IR light fields was demonstrated for the first time in the spectral as well as time domain. The occurrence of laser emission in polycrystalline ZnO thin films pumped in the tunneling excitation regime was proven by a characteristic s-shape of the output via input signal represented in a log-log scale, rapid spectral narrowing and a sudden acceleration of the recombination dynamics from 100 ps to 10 ps. The $w_0^{-1.5}$-dependence of the threshold pump intensity I_{th} on the pump laser spot size radius w_0 revealed random lasing and ASE as the responsible lasing mechanism. The dependence of the lasing pump threshold intensity in a wide spectral range from the near to the far-IR was determined. The nature of inter- and intraband absorption processes were evaluated by comparing the measured pump threshold intensities as a function of the laser wavelength with theoretical intensities linked to a carrier density enabling gain in ZnO. The laser threshold

increases from 0.33 to 0.6 TW/cm^2 when the excitation wavelengths are changed from 1.2 to 2 μm. At this state the interband absorption appears dominantly by multiphoton absorption. Increasing the pump wavelengths up to 10 μm a decreasing lasing threshold value down to 0.12 TW/cm^2 was observed. While the tunneling excitation rate becomes more or less constant for wavelength larger 3 μm, the decreasing threshold value for increasing wavelengths, demonstrates clearly that free carrier absorption (via impact excitation) plays an important role in the excitation process of mid to far-IR light. Comparing the experimentally measured values to simulations using the Keldysh-Drude excitation model revealed a electron-electron scattering time of 5 fs. With regard to practical applications, these results show the possibility of an optically pumped semiconductor laser in a multiphoton or tunnel excitation regime, regardless of the ratio $E_g/\hbar\omega$ of the band gap to the pump laser field frequency (wavelength). The findings of the last section act as a benchmark for the development of absorption models which include inter- as well as intraband processes and valid in the case of tunneling excitation. This knowledge might be from crucial importance of future light wave driven electronics and photonics in dielectrics and semiconductors.

Chapter 5

Nonlinear pumped nanowire nanolaser

The previous chapter was dedicated to the results on stimulated emission of a random lasing process in polycrystalline ZnO thin films upon highly non-linear pump processes with photon energies much smaller than the band gap. As demonstrated and discussed in Section 4.3.2, the random lasing onset dynamics in polycrystalline ZnO thin films appear slow compared nanowire (NW) laser systems [41]. Indeed NW laser systems are of particular technological interest since they depict the possible laser resonator, working close to the diffraction limit [40]. Because of an unique interplay of high modal gain and low loss guided modes resulting in a low threshold lasing threshold, NW lasers are from striking interest in metrology and sensing as well as switching applications [40, 152]. Moreover, the possibility of lasing in quasi one dimensional semiconductor NW systems pumped by far off-resonance excitation is highly desirable. This pumping regime requires to use strong light fields similar to the far off-resonance pumping in ZnO thin films.

First the NW sample synthesis method and characterization results are presented in Section 5.1.1, including both NW arrays and isolated/single NWs. This is followed by a brief presentation of the used experimental setup to study the emission from strong field excited NW arrays and single NWs (Section 5.1.2). The following Section 5.2.1 discusses the results obtained from a single ZnO NW. The excitation was carried out using a three-photon absorption process at a wavelength of 0.8 μm and a tunnel excitation at a wavelength of 3.6 μm. The threshold pump intensities required for NW lasing are compared for 0.8 μm and 3.6 μm pump wavelengths by investigating arrays of randomly oriented ZnO NWs, as presented in Section 5.2.2. Finally, in Section 5.3.1, experimental results on lasing in vertically aligned arrays of ZnO NWs are presented, revealing whether there is a coupling between the individual NWs of the collective array or whether the properties of the individual NWs determine the emission properties of the array. Results of this chapter are published in Ref. [153] and [154].

5.1 Methods for the nanowire lasing studies

The demand for high quality semiconductor NW lead to the development of a variety of synthetization methods over the last two decades [40]. In this work NW arrays, showing high crystalline quality and low defect densities were grown in a self-organized manner using a vapour-phase-transport (VPT) technique. Due to the nanoscale dimensions, below the resolution limit of light microscopes, advanced electron imaging techniques have to be applied in order to determine their structural and morphological properties. Therefore the used structures were investigated with a scanning electron microscope (SEM).

5.1.1 Nanowire sample synthetization

The ZnO NW samples used in experiments were produced in collaboration by the Institute for Solid State Physics at the Friedrich Schiller University Jena in the group of Prof. Ronning. A thermal-transport-technique was used to synthesize the nanostructured samples of different morphologies. The growing process takes part in a horizontal tube furnace. By adjusting the synthesis conditions (substrate preparation, temperature and pressure in the tube) vertically ordered or disordered arrays of NW were achieved in separate processes, which are explained in Ref. [155]. The mechanism responsible for structure growing is the vapor-liquid-solid (VLS) approach, which is explained in detail in Ref. [156].
The target substrate for NW growth, a Si waver, was covered beforehand with a 500 nm aluminium doped ZnO or 10 nm Gold layer in the case of ordered or disordered nanostructures, respectively. These layers form droplet alloys under high temperature, which act as liquid catalyst for the growth process and determine the diameter of the nanorods. The source material is delivered constantly by a mixture or a pure of ZnO and carbon powder evaporated in the hot zone of a furnace at 1050°C and 1350°C for ordered and unordered nanostructure samples, respectively. An Argon gas stream transported the vapour to the catalyst covered substrate. A growth of the nanorod occurs at the liquid-solid interface, if the cataylst droplet gets supersaturated with Zn and O at a certain temperature and pressure [157]. During the growth process the pressure was kept constant at 10 mbar and 100 mbar within the tube for ordered and disordered samples, respectively.
Examples of the as-grown nanostructure batches are shown in Figure 5.1 a-d. The array of vertically aligned nanorods (Figure 5.1 a, b, d) showing a length of around 6-10 μm and an average diameter of 200-450 nm. The disordered samples or randomly oriented NW arrays, as shown in Figure 5.1 b), are formed by an unordered collection of nanorods having an average length of 20 μm and diameters of 300-500 nm. The properties of the arrays such as length, diameter, and interwire spacing were evaluated using a scanning electron microscope (SEM), as shown in Figure 5.1. It becomes apparent that the growth method of the array fabrication features a

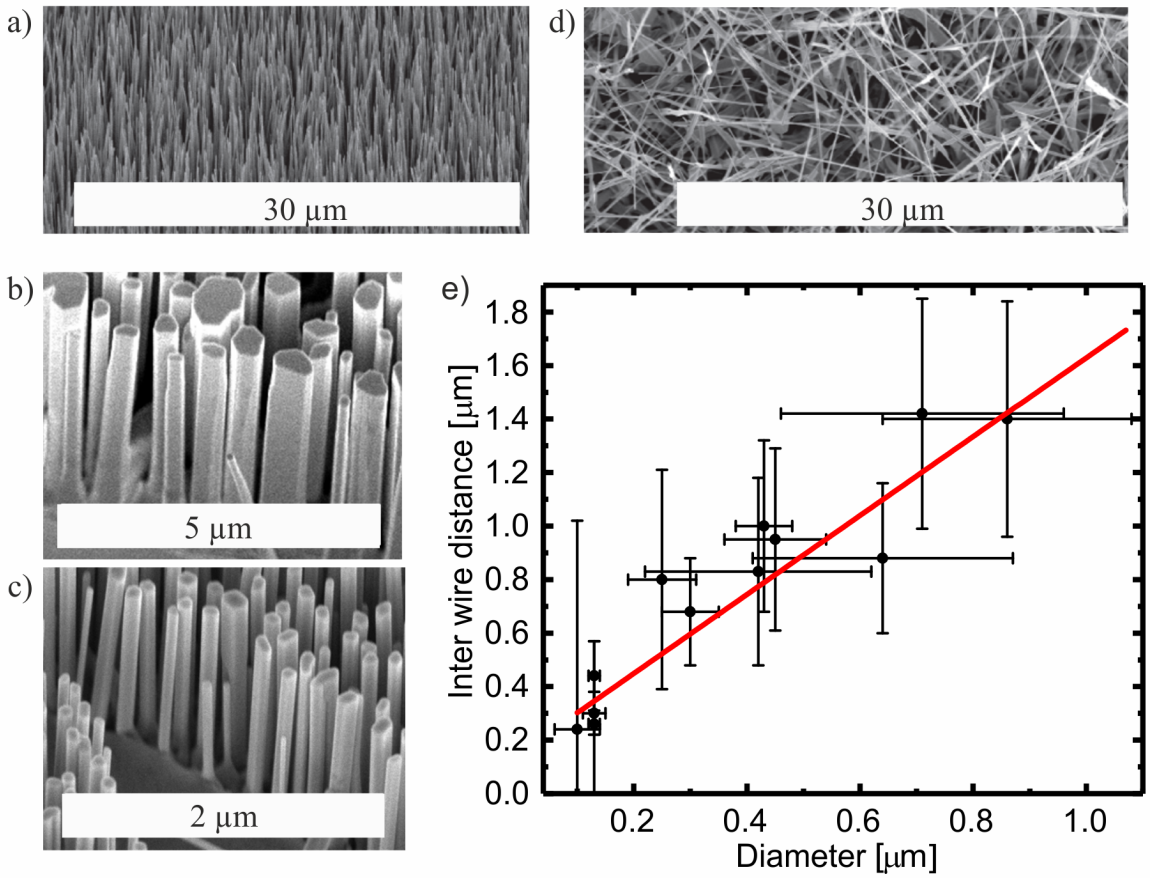

Figure 5.1: a), b) and c) SEM images of vertically aligned NW arrays. b) and c) vertically aligned NW arrays with thick and thin ZnO NWs of roughly 430 and 150 nm mean diameters, respectively. d) SEM image of a randomly oriented NW array (disordered array). e) Measured inter-wire distance as a function of the NW diameter for samples grown under different conditions. The red line is a guide to the eye and reveals that diameter and inter-wire distance are coupled. The error bars show the standard derivative of measured NW parameters.

characteristic correlation between the wire diameter and the spacing between the wires. The measured dependence of the inter-wire spacing and the wire diameter is shown in Figure 5.1 e. It reveals that thinner wires are closer to each other, which is explained by the competitive growth mode for the used synthetization parameters [158].
Using a dry impring methode individual NWs were transferred to a clean Si substrate with a 1.5 μm thick layer of SiO_2 on top. Subsequently single NWs could be found on the substrate using an optical imaging system as well as a lithographically imprinted coordinate system on the substrate for defining and finding individual specimen.

5.1.2 Experimental setup

Figure 5.2 a depicts the used μ-photoluminescence (μ-PL) setup to measure the spontaneous emission and lasing from a single NW in reflection geometry. The femtosecond laser pulse

energy was adjusted by a combination of two wire grid polarizers (WG). The pump beam was focused with a f=10 cm CaF_2 lens under an angle of 45 degree normal of the substrate. The NW emission was detected using a 50x long working distance microscope objective with a 0.4 NA (MO) and reimaged to the entrance slit of an imaging spectrometer (Andor Shamrock 193i) equipped with a Peltier-cooled CCD (Andor Newton DU920P BR-DD). To find NWs on the SiO_2/Si substrate, it could be irradiated with a white light source and imaged to a CCD camera with the same objective and a lens when the collected radiation was redirected by a flip mirror to the CCD-camera. A band-pass filter (BP) was used to filter out the pump wavelength. The SiO_2/Si marker substrate with the NWs was fixed on a 3-axis stage with the purpose to move the sample relative to the excitation spot on the sample.

Figure 5.2 b illustrates the optical setup used to investigate the NUV emission properties of NW arrays. The intensity of the pump laser was controlled by two wire-grid polarizer (WG). The laser was focused onto the NW samples using a CaF_2 lens. The emission from the NW array samples was collected under an angle of 45 degree with a 4x microscope objective (MO, 0.15 NA) and imaged with a lens to the entrance slit of a spectrometer (Ocean Optics USB400 UV-VIS). Using a band-pass filter (BP) the reflected pump wavelength was blocked.

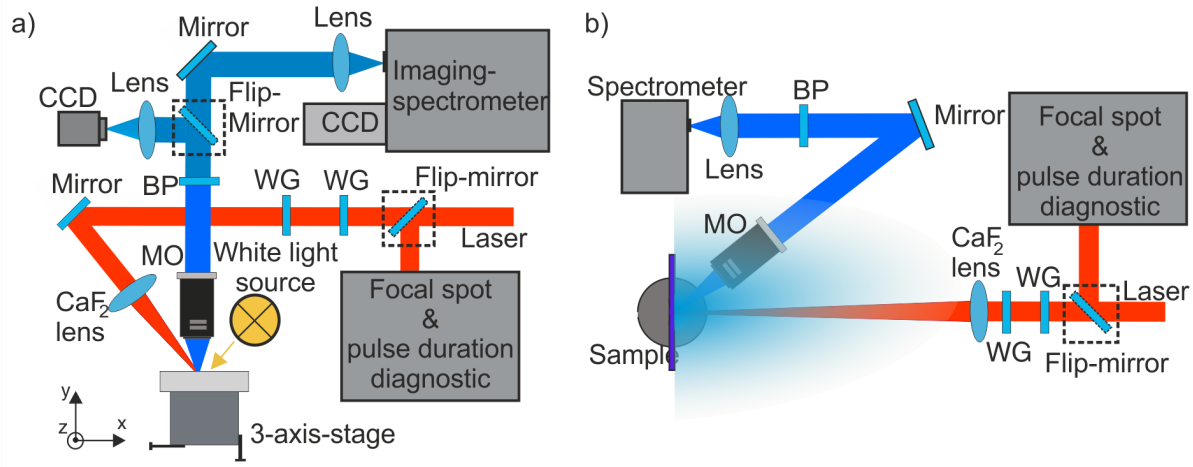

Figure 5.2: Experimental setup used to study the emission of a) single NWs and b) NW arrays. a) μ-PL setup used to study single NW NUV emission. The NW were excited under an angle by a CaF_2 lens after the laser power was attenuated by a pair of wire grid polarizers (WG). A 50x long working distance objective (MO) was used to detect the NUV emission from the NW. Additionally the objective together with a white light source and a CCD camera formed an imaging system which aims to specifically identify NWs on the SiO_2/Si substrate. The scattered pump light was filtered from the NUV emission by a band pass (BP) filter before it was detected by an imaging spectrometer equipped with a peltie cooled CCD. b) The power of the femtoscond laser pulses were adjusted by a pair of wire grid (WG) polarizers before the laser beam was focused onto the sample by a CaF_2 lens. The emission was collected by a 4x microcope objective (MO) in reflection geometry and refocused to a UV-VIS spectrometer. To block scattered pump light, a band pass (BP) was installed.

Experiments at 0.8 μm were performed with 45 fs laser pulses from a Ti:Saphire chirped pulse amplification system operating at 1 kHz repetition rate which generated pulses with energies up

to 0.7 mJ. The pulse duration was measured using a second harmonic (SH) autocorrelator (see Figure 4.2 a) and the spatial distribution of the intensity in the focus was recorded with a CCD-camera (ThorLabs BC106N-VIS) (see Figure 4.3 a). A three-stage OPA based on potassium titanyl arsenate (KTA) nonlinear crystals was used to generate Mid-IR 0.1 mJ, 100 fs laser pulses at a repetition rate of 500 Hz. The white light seeded OPA was pumped by 8.5 mJ, 200 fs pulses originating from Yb:CaF_2 regenerative amplifier operating at 1030 nm central wavelength. The signal and idler pulses generated in the OPA were tunable in the spectral range of 1.4-2.0 μm and 2.0-4.0 μm, respectively. The mid-IR idler pulses, which are slightly negatively chirped, were compressed to roughly 100 fs duration by inserting different amount of silicon plates possessing positive dispersion in this spectral range. The mid-IR laser pulses were temporally and spatially characterized using second-harmonic-generation frequency resolved optical gating (SH-FROG) and knife edge methods, respectively (see exemplary Figure 4.2 c and Figure 4.3 b).
In all experiments the intensity on the target was calculated using Equation A.5 from the measured pulse energy, temporal pulse duration and spatial intensity distribution on the sample. The pulse duration and the focal spot size of the 0.8 μm pumping beam was 45 fs and 600 μm, respectively. Both varied within the range 105-130 fs and 100-200 μm in the spectral range of 1.5-4 μm, where the wavelength can be adjusted. All experiments were carried out at ambient conditions and room temperature.

5.2 Strong field pumped lasing

Stimulated emission in ZnO NWs was previously reported upon single photon [34] as well as under two [159] and three photon absorption [38, 160] pumping conditions. In Section 4.3 far off-resonance pumping of ZnO thin film and subsequent laser emission was demonstrated, i.e. that the pump photon energy is much smaller than the electronic band gap. Here, single NWs as well as arrays of randomly oriented NWs are excited by strong fields of femtosecond laser pulses in a wide spectral range from the near to the mid-infrared. The pulses at 0.8 μm and 3.6 μm wavelength correspond to a Keldysh parameters of γ=2 and γ=0.5 referring to Eq. 2.3, respectively. Thus, it can be expected that in this experiments the multiphoton as well as tunneling excitation mechanisms play a role. In Section 5.2.1 single ZnO NWs are pumped with laser pulses at 0.8 μm and 3.6 μm. In order to investigate the wavelength dependency of the excitation process, randomly oriented arrays are used in Section 5.2.2 to average geometric and statistical features in the excitation process.

5.2.1 Single ZnO nanowire laser

First investigations were performed using single isolated ZnO NW with diameters of 200-250 nm and lengths of 5-15 μm.

The NUV emission from the individual NWs was investigated as a function of the excitation laser intensity using the μ-PL setup shown in Figure 5.2 a. Typical pump intensity dependent emission spectra of an individual ZnO NW pumped at 0.8 μm wavelength as well as at 3.6 μm wavelength are shown in Figure 5.3 a and c, respectively. The emission spectra show similar pump laser intensity dependent features for both pump wavelengths: At low pump intensities the emission spectra reveal a broad emission centered at 390 nm which arise due to spontaneously recombining excitons and free electrons. Increasing the pumping intensities up to the pump laser threshold I_{th}, the broad spectrum of spontaneous luminescence transforms into a much narrower spectrum of stimulated emission, which resembles Fabry-Pérot modes (FPM) of the NW. The applied pump intensity is sufficient to induce gain in the ZnO which overcomes the losses and is therefore considered as laser threshold. This intensity is therefore considered as laser threshold in agreement with the literature[34]. Increasing the pump power well above the lasing threshold, the emission spectrum significantly broadens and experiences a red shift, while the distinct FP modes structure vanishes. The red-shift and the spectral broadening is caused by the band-gap renormalization in the highly excited semiconductor above the Mott-density and by heating up the gain medium [32, 37, 131, 132, 133]. The vanishing of the FPM is attributed to the dynamical change in the refractive index due to a fast change of the carrier density due to depletion of carrier inversion [32, 37]. The electron density of $2 \cdot 10^{25}\mathrm{m}^{-3}$ necessary to observe gain is one order of magnitude above the Mott density (roughly $1.5 \cdot 10^{24}\mathrm{m}^{-3}$ in ZnO at room temperature [32]), thus it is assumed that gain and emission occur from an electron hole plasma (EHP) [36, 37, 161, 162].

Figure 5.3 b and d depict the integrated yield of the NUV emission from a single ZnO NW laser as a function of the pump pulse intensity upon pump wavelengths of 0.8 μm and 3.6 μm, respectively. The data illustrated in a log-log-representation clearly reveal a S-shape behaviour. Reaching the threshold pump intensity (I_{th}) to enable lasing, the yield increased abruptly by one order of magnitude for both pumping conditions. For pump pulse intensities below and above the threshold intensity the yield follows a linear behaviour in the log-log representation as highlighted by the black lines. This rapid increase of the output signal and the spectral narrowing in combination with the observed longitudinal mode structure of the emission are clear indications of the transition from spontaneous to stimulated emission [134, 135].

Figure 5.3 e and f shows magnified luminescence images of the single-wire nanolaser, pumped at 3.6 μm wavelength with different pump intensities. Below the lasing threshold, a homogeneous, isotropic emission along the whole NW is recorded, while the emission is emitted almost completely from the end facet of the wire for a pump intensity above the lasing threshold. The images shown in Figure 5.3 e and f prove the concept introduced in Figure 2.6 that the NW end facets form a resonator. Furthermore, the outcoupling of the light occurs on the resonator end mirrors, which are the end facets of the wire in the case of a NW laser.

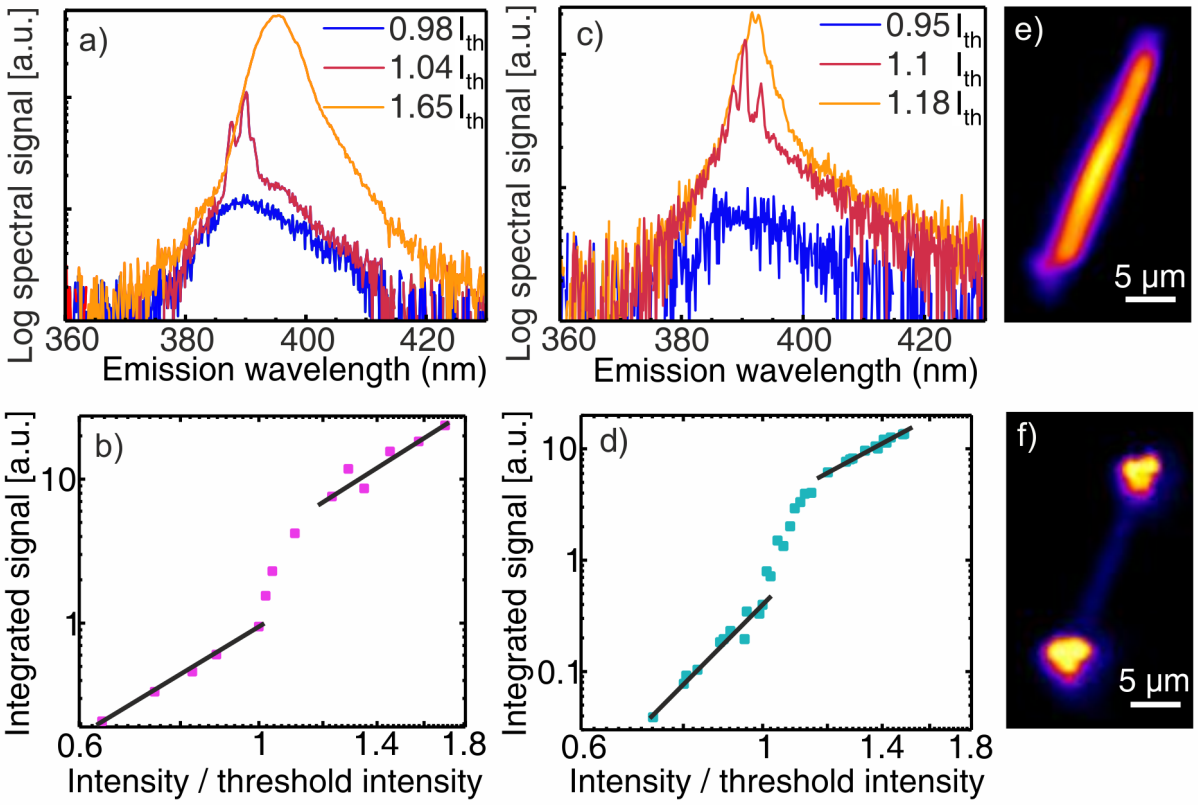

Figure 5.3: The emission spectrum of a single NW upon pumping a) by 3-photon absorption from a 0.8 μm femtosecond laser source and b) by the tunnel excitation using a 3.6 μm femtosecond laser source. Three spectra are shown for each case: below the lasing threshold (blue), slightly above threshold (red), and well above threshold (orange). Log-log scale dependence of the UV emission yield from a single NW pumped by c) three-photon absorption from a 0.8 μm femtosecond laser source and f) by the tunnel excitation using a 3.6 μm femtosecond laser source. The black lines depict the change of the slopes (kink) and highlight the rapid incerease of the integrated yield when the threshold pump intensity (I_{th}) is applied. Magnified CCD images of an emitting single ZnO NW pumped by a 3.6 μm laser when the pumping intensity is e) below the lasing threshold and f) above the lasing threshold.

A comparable threshold pump intensity of $I_{\text{th}} = 0.7\,\text{TW/cm}^2$ (0.23 V/Å field strength) was estimated for pumping at 0.8 μm and 3.6 μm. The exact calculation of the threshold pump intensity was possible because the exact wire position in the excitation spot as well as the effect of the laser polarization on the pump process were not known due to the experimental conditions.

Further semiconductor materials

So far only ZnO have been considered as optical gain material. However, optically pumped lasing has been demonstrated in a large variety of semiconductor materials. In Cadnium Sulfide (CdS) NWs lasing was achieved upon optical pumping using single [34] and two photon absorption processes [163]. In nano- and microwires (MWs) made from perovskite material, laser emission was observed after optical excitation in the regime up to three-photon absorption [164].

Aiming to demonstrate that pumping of laser materials in the tunneling regime is not restricted to ZnO as gain materials, the aforementioned experiments were repeated with CdS NWs and $CsPbBr_3$ perovskite MWs. Both the CdS and perovskite material exhibit a direct electronic band structure with a gap of 2.45 eV and 2.3 eV and were excited by sub 100 fs laser pulses centered at 3.6 and 3.2 μm, respectively. Similar spectral characteristics were obtained with single cadmium sulfide (CdS) NWs and $CsPbBr_3$ perovskite MW as shown in Fig. 5.4. Figure 5.4 a depicts the emission spectra from a CdS NW with a diameter and length of roughly 300 nm and 10 μm, respectively, as a function of the pump laser intensity. For low pump intensities the emission is dominated by a broad photoluminescence spectrum due to spontaneous recombination of excitons and free carriers. Increasing the pump power narrow band emission lines, FP-modes appear superimposed to the broad spontaneous emission. The spectral intensity grows rapidly and shift spectrally to longer wavelengths when the pump intensities is further increased. For even higher pump intensities the FPMs transform into a continuous spectrum. This evolution can be understood, in analogy to the case of ZnO emission explained above. In Figure 5.4 b the results of optically excited $CsPbBr_3$ perovskite MWs are shown. The used microwire was 6.3 μm long and had a diameter of 1.6 μm. For low excitation intensities only a broad emission is detected, spectrally located at the band gap energy,. Increasing the pump intensity narrow band lines appear, which shift towards longer wavelengths for stronger pumping intensities. Due to dimensions of the MW it is assumed that this modes result from an interplay of FP-modes and the formation of whispering gallery modes [42]. The inset in Figure 5.4 b shows the spectrally integrated yield as a function of the pump power in a log-log representation. The emission yield shows a S-curve which is characteristic for the transition from spontaneous to lasing emission [134]. Figure 5.4 c and d shows magnified CCD images of the emitting perovskite MW below (Fig. 5.4 c) and above (Fig. 5.4 d) the threshold pump intensity I_{th}. Similar to images taken from ZnO NW, shown in Fig.5.3 e and f, the whole MW emits homogeneously below the threshold intensity when recombination is dominated by spontaneous emission. For higher laser intensities above I_{th}, stimulated recombination dominates and the emission is localized on the end facets of the microwire.

The dependence of the emission on the pump intensity proves that CdS NW and $CsPbBr_3$ perovskite MW can be excited up to population inversion in the strong field excitation regime. The Keldysh parameter was determined to be 0.7 and 0.8 in the case of CdS and $CsPbBr_3$ perovskite material, demonstrating, that optical pumping occurred dominantly in the tunneling excitation regime. Thus tunneling excitation can be established as a general excitation mechanism and is not specific to a particular semiconductor nanomaterial.

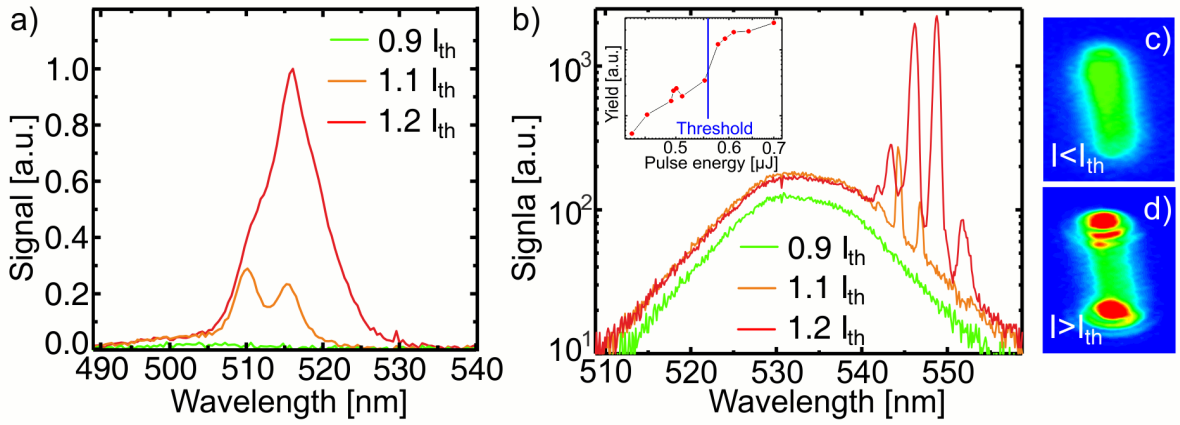

Figure 5.4: Emission from a single CdS and perovskite wire. a) Emission spectra from a single CdS NW as a function of the excitaiton power. Optical excitation was supplied by a femtosecond laser pulse with a central wavelength of 3.6 μm. The emission spectra clearly show a transiton from a weak broadband spontaneous to strong and narrowband stimulated emission when the pump power is increased. b) Emission from an optical excited $CsPbBr_3$ Perovskite microwire. Femtosecond laser pulses at 3.2 μm were used to pump the material up to inversion which is manifestated in the emission spectra by the appearance of narrow band lines on top of broad band emission. Inset: Spectrally integrated yield as a function of the pump pulse energy in a log-log representation exhibit the characteristic S-shape trend indicating the transition from spontanous emission to lasing. c) and d) CCD images of the excited wire below and above the threshold to observe lasing, respectively.

5.2.2 Wavelength dependence of lasing threshold

Figures 5.3 clearly demonstrates that lasing of a single semiconductor NW can be achieved in both the three-photon absorption (γ=2) and the tunneling excitation regime (γ=0.5). Remarkably, the threshold pumping intensity is very similar in both excitation regimes in spite of the large difference in the excitation wavelengths (nearly a factor of 5) and the significant difference in the underlying physical excitation mechanism.

Thus, the question rises how the lasing threshold pump intensity of individual ZnO NW depends on the pump wavelength. Arrays formed by randomly oriented NW (see Figure 5.1 d) were used to investigate the dependence of the lasing pump threshold on the pump wavelength, by ruling out influences of the nanolaser emission on orientation and statistical variations in geometric parameters of individual wires (length, diameter, interwire spacing). The emission from the disordered array can be considered as an incoherent superposition of the emission from individual NW lasers. A detailed comparison of emission characteristics of a single wire and the disordered array of wires was reported in Ref. [160]. Figure 5.5 a and b depict the emission spectra as a function of the pump laser intensity for a pump wavelength of 0.8 μm and 3.6 μm. A broad band NUV emission centered at 390 nm is detected for low pump intensities (I<I_{th}) . Increasing the laser intensity to a value around the threshold (I=I_{th}), a rapidly growing and narrower peak appears on top of the previous broad emission band. For an even higher excitation power (I>I_{th}) the emission peak broadens and experiences a redshift. The spectral evolution can

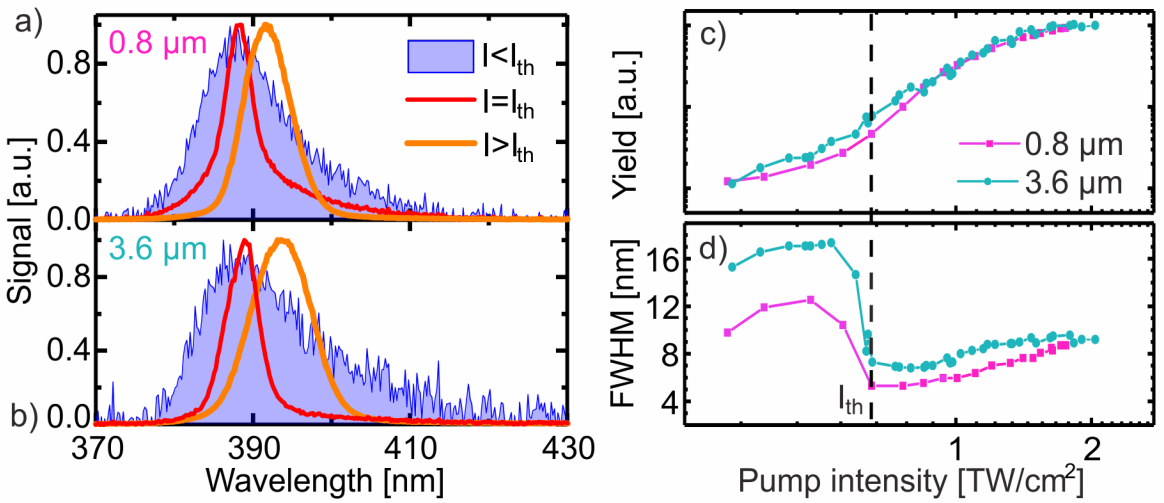

Figure 5.5: NUV Emission spectra from a random oriented NW array excited by femtosecond laser pulses at a) 0.8 μm and b) 3.6 μm. The spectra show the emission as a function of the pump laser intensities: below (blue), close to (red) and above (orange) the threshold pump intensity. In contrast to the lasing emission spectra observed from single NW a continous spectra instad of FPM are detected, due to the superposition of many NW with varying geometry c) The spectrally integrated intensity in a log-log representation and d) full-width half-maximum (FWHM) spectral width of the UV emission from NW arrays as a function of pump intensity. The dashed vertical line with the arrow indicates the threshold pumping intensity which is defined as the intensity when the emission and band width rapidly increases and narrows, respectively.

be explained in analogy to the observed findings for single nanowire laser. The emission spectra is based on spontaneous recombination of excited excitons and free electrons for low pump intensities. Increasing the pump laser intensity enables the onset of gain in the ZnO material of the NWs. Reaching the pump conditions, when the gain overcomes the losses of the NW laser system, stimulated recombination processes dominate the emission spectra. In the NW this is linked to the formation of narrow band FPM, which are in contrast to the single wire case, not visible in the spectrum from an arrays due to the superposition of the emission of many wires with different geometries. A further increase of the pump power results in a redshift of the emission spectra due to band gap renormalization and heating of the ZnO material similar to the redshift in individual NW lasers [32, 37, 131, 132, 133].

In order to enable a comparative study of lasing as function of the pump conditions, a criteria is required to define the onset of lasing. Figure 5.5 c depicts the dependence of the NUV emission yield on the pumping intensity in a log-log scale for a ZnO NW array. Furthermore, Figure 5.5 d shows the FWHM of the emission spectra as function of the pump intensity. In comparison to the single wire measurements (see Figure 5.3), the S-shape curve in the yield over intensity plot is not that pronounced due to the superposition of many individual nanolasers with different length, orientations and quality in the array leading to a smearing out of the threshold. However, the transition from spontaneous emission to lasing appears in a much clearer manner in the plot of pump intensity dependent spectral bandwidth shown in Figure 5.5 d. Hence, significant

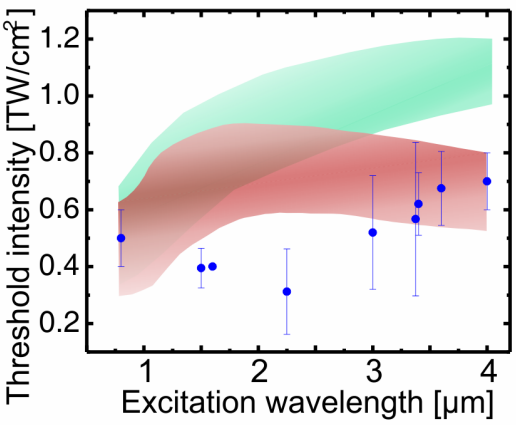

Figure 5.6: Threshold intensity as a function of the pumping wavelength measured experimentally (blue dots) and simulated numerically for the same experimental parameters using the model without FCA (greenish band) and including FCA and impact excitation (red band). The bands mark the range of threshold intensities calculated for the range of pump pulse duration used in the experiments.

spectral narrowing during the transition from spontaneous to stimulated emission demonstrates the onset of lasing. This is a well-known mechanism in laser physics [134, 135]. It has been confirmed that this threshold value is linked to the onset of lasing by time resolved measurements [160].

The lasing threshold is essentially the same for pumping the NW array at 0.8 μm and 3.6 μm wavelengths with a value of about 0.7 TW/cm^2 (0.23 V/Å) (Figure 5.5). Thus, the increase in the pumping wavelength by a factor of 5 does not essentially require an increase in the pumping intensity to achieve laser emission from the NWs. Note that the threshold intensity value determined at 0.8 μm pumping wavelength for the disordered array of NWs is very close to the threshold measured for an individual NW (see Fig. 5.3). The spectral width of the NUV lasing emission and its dependence on the pumping intensity for the NW array is almost identical to the dependence measured for the single nanowire (see Figure 5.3 and Figure 5.5).

The corresponding Keldysh parameters for 0.8 μm and 3.6 μm pumping are 2.5 and 0.5, respectively. These Keldysh parameter together with the comparable pump threshold intensities suggest that pumping with 0.8 μm wavelength proceeds clearly in the multiphoton excitation regime, whereas for the 3.6 μm pumping occurs in the tunneling regime. Figure 5.6 (blue dots) shows the dependence of the threshold pumping intensity as a function of excitation wavelength in the entire spectral range from 0.8 μm to 4 μm. Note that these measurements at different wavelengths were carried out with the same NW array sample but at different positions at the sample. Thus, the results in Figure 5.6 include possible statistical variations of morphology and optical quality along the NW array. Eventually the error bars indicate the variation of the threshold intensity value with the diameter of the pump beam, which varied for different wavelengths and for the measurements at a fixed wavelength within a factor of 2 It is obvious that intensities well below 1 TW/cm^2 are sufficient for lasing initiation in the entire near to mid-IR spectral range and that the threshold is almost independent on the pump wavelength. The experimentally measured values were compared to calculations based on the strong field excitation model presented in Section 2.1.3, in analogy to the considerations done in the case of pump

wavelength dependent lasing in ZnO thin films (Section 5.2.2). The simulations of the density of excited carriers as function of the laser wavelength and intensity are performed using Equation 2.9. Again $2 \cdot 10^{25} m^{-3}$ electrons are assumed as an adequate threshold carrier density of the ZnO active medium.

Figure 5.6 shows the simulated wavelength dependence for the threshold intensity together with the experimental data depicted as blue dots for both situations, with and without free carrier absorption depicted by red and green bands respectively. The coloured bands in Figure 5.6 represent the variations when changing the pump pulse width from minimum to maximum values of 45 and 140 fs used in the experiments. Although the results of the simulations in both cases agree with the experimental values within a factor 2.5, the model including the absorption of the laser energy by free carriers in the conduction band reveals better coincidence with the observed saturation of the threshold intensity obtained in the experiment in the mid-IR range. In addition Figure 2.2 depicts that the strong field excitation rate in the three-photon absorption regime at 0.8 μm pumping wavelength is almost two orders of magnitude higher than the excitation rate in the tunnel regime at the 3.6 μm pumping wavelength. Therefore the simulations without free-carrier absorption (see Figure 5.6) predict an increase in the threshold pumping intensities by a factor of 2 by changing the wavelength from 0.8 μm to 3.6 μm, in contradiction with the experiment. However, including free-carrier absorption enables saturation and even a slight decrease in the pumping intensity threshold within the considered wavelength range. This can be explained by more efficient acceleration of free carriers with increasing pumping wavelength that enables additional impact excitation based on electron-electron scattering. As shown in Section 2.1.2 the acceleration of the electrons in the conduction band by the electric field scales with the laser intensity and wavelength by $I \cdot \lambda^2$. Also shown in Section 2.1.2, the electron impact exciation makes a significant contribution to the population of the conduction band for pumping wavelengths above 1.5 μm. Thus, FCA plays an important role for long excitation wavelengths.

Figure 2.5 illustrates the dependence of the FCA-process on the pulse duration revealing that longer pulses increase the kinetic energy of the free electrons. Consequently, avalanche-like excitation as a result of electron heating becomes more likely with increasing pulse duration. What may associated with irreversible damage to the material. In the experiments a strong limitation of the possible pulse durations was recognized and efforts for maximum pulse compress always had to be applied.

In spite of the simplicity of the used model, which were discussed in detail in the Section 2.1.1, the numerical simulations provide reasonable agreement between the absolute calculated threshold intensity and the experimentally measured values. Astonishingly, the differences are in the range of a factor of two, because the experimentally observed threshold pumping intensities are determined by the balance between gain and loss depending on the NW geometry (length, di-

ameter), the structural quality, etc. The difference in the trend of the curves derived numerically and measured experimentally can also be related to spatial inhomogeneity of the disordered NW array.
In conclusion this section demonstrated that lasing is achieved in optically pumped semiconductor NWs which were far off-resonance excited by strong light fields. The onset of laser emission has been determined by a rapid spectral narrowing and threshold like increase of the emission yield when the pump laser threshold intensity was reached. The pump wavelength used in the experiments varied between 0.8 and 4 μm, which correspond to a ratio of the forbidden band gap to the photon energy from 3 to 11, respectively. Considering the Keldysh parameter (γ) and the scaling of threshold pump intensity as a function of the pump wavelength in comparison with calculated values, it is clear that the excitation of the NW was established via multiphoton (γ>1) below 1.5 μm as well as in the tunneling (γ<1) regime above 1.5 μm.

5.3 Single nanowire determined nanowire array emission

In the previous section arrays of randomly oriented NWs were used to study the dependence of the threshold pump intensity of NW lasers on the pump wavelength. An open issue remains regarding the lasing in NW arrays. How is the light coupling between the wires influencing the laser properties. A cross talk between the nanowires by contacts can not be excludes in arrays formed by randomly oriented NW (see Figure 5.1 b) [160]. Arrays of horizontally aligned NW (see 5.1 a,c,d) were used to study the effect of the interwire light coupling. The spectrally integrated NUV emission and its spectral width (FWHM) were estimated from the measured emission spectra in order to study the dependence of the onset of lasing in NW arrays as a function of average NW length, diameter and interwire distance.

5.3.1 Emission from an vertically ordered array of nanowire

The ZnO NW arrays were optically excited by 0.8 μm central wavelength, 45 fs duration, 1 kHz repetition rate, up to 0.7 mJ energy pulses, as delivered by a Ti:Sa amplifier system. Considering a bandgap of 3.2 eV for ZnO at room temperature, the excitation of electrons from the valence to the conduction band is achieved by three photon absorption [32, 129].
Figure 5.7 depicts the NUV emission spectra of two different NW arrays for different intensities of the pump pulse. Two characteristic sets of emission spectra were observed in the experiment. The first type showed a broadband spontaneous emission with spectral width almost independent on the pump intensity over the entire range of pumping intensities, as depicted in Figure. 5.7 a. The second type revealed an abrupt spectral narrowing at a certain threshold pump intensity (Fig. 5.7 b). As already observed in randomly oriented arrays, this spectral narrowing

manifests the transition from spontaneous emission to stimulated emission, if it is accompanied an increasing slope in the log-log plot of the pump power dependence (Fig. 5.7 c) and by time-resolved measurements, which were published elsewhere [160].

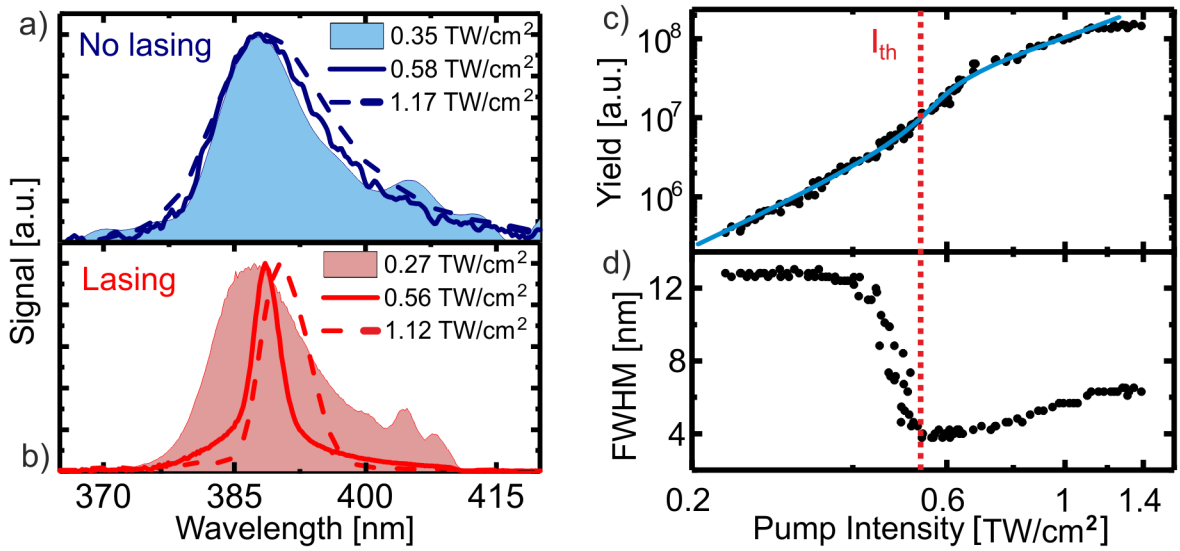

Figure 5.7: a) Emission spectra from a representative NW array don't showing the transition from spontaneous to stimulated emission. b) Evolution of the emission spectra characteristic for NW arrays showing stimulated emission. c) Pump intensity dependent integrated emission intensity from a lasing ZnO NW array. The blue line depicts the yield calculated using the lasing rate equation model. d) FWHM of the NUV emission from a lasing ZnO NW array. The red lines are a guide to the eye illustrating the increase of the slope (kink) indicating the transition to stimulated emission. The sudden increase of of the emission yield and spectral narrowing are used to determine the threshold pump intensity.

In agreement with the explanation of pump laser intensity dependent emission spectra from randomly oriented NW arrays it is assumed, that for low pump intensities, the broadband spontaneous emission centered at roughly 385 nm originates from a combination of exciton and free electron-hole recombination [30]. Previous investigations of spectral dynamics in NW arrays pumped via three-photon absorption and the respective simulations in Section 2.1.3 suggest that, for pump intensities of 0.6 TW/cm^2, around the lasing threshold, the density of the excited carriers exceeds the Mott density at room temperature. Than the emission originates from band-to-band recombination in an EHP [36]. Lasing in individual NWs with diameters less than 1 μm usually exhibit a FP-type nature [34], whereas the mode structure in MWs might include also whispering gallery type modes [43]. In the case of NW arrays, the FP mode structure is washed out in the spectrum due to statistical variations of wire length in the array [165]. Increasing the pump intensity above the threshold causes a broadening (Fig. 5.7 d) and redshift of the central emission wavelength (Fig. 5.7 b) of the lasing spectrum [165] as well as a saturation of the emission yield (Fig. 5.7 c). The broadening can be explained by a widening of the spectral gain profile, which is characteristic of EHP gain [32]. The observed redshift for higher pump

intensities is attributed to the band gap renormalization in the EHP and heating of the ZnO material [32, 37, 131, 132, 133]. The saturation of the three-photon-absorption process leads to the observed saturation in the NUV emission yield at around 1 TW/cm^2 pump power [129]. The blue line in Figure 5.7 c depicts the calculated yield using the coupled rate Equations 2.12-2.14 using the interband three photon absorption described in Eq. 4.2 with model parameters in the range of reported values in literature and optimized to reproduce the experimental result. Note, all the spectral characteristics of NW arrays with increasing pump intensity have been observed for individual wires,too (see Figure 5.3). Therefore, its supposed that the observed lasing thresholds in arrays can be explained and qualitatively described by non-interacting individual NWs with the average length and diameter of the array.

5.3.2 Single wire parameter dependent lasing properties

The threshold gain for NWs with different lengths and diameters was calculated using Equation 2.11, the quantities for the reflectivity and the confinement factor are given in Figure 2.6 while further the waveguide losses α_w were neglected. For the reflectivity on the ZnO-Si-substrate interface a constant value of 0.19 was assumed, which was roughly estimated by the Fresnel-reflection coefficient. The contour plot shown in Figure 5.8 depicts the estimated threshold gain values, when the wire length and diameter were varied from 1 to 14 μm and from 100 to 900 nm, respectively. The blue dots mark the investigated arrays which showed lasing, while arrays with absent lasing emission are depicted in red. Thus, only arrays consisting of wires with average diameters >200 nm and/or lengths >5 μm showed stimulated emission in the experiments. The length dependence can be understood, since a minimum length of gain material is necessary to compensate the cavity losses. Thus, no lasing is observed even at the highest pump intensities used in the experiment, which were close to the damage threshold of the arrays. The corresponding gain thresholds for arrays showing lasing are in the range of 0.1 to 0.5 μm^{-1}. This numbers are in a good agreement with previously reported numbers for single ZnO NW [34] in which wires with similar geometrical parameters like the averaged geometrical parameters of wires in the used array samples. Figure 5.7 provides, in fact, a rough estimate for the gain achievable in ZnO NW arrays under conditions of three-photon absorption. For example, an absence of lasing in experiments with NW arrays having the average diameter larger than 300 nm and length larger than 2 μm implies that the gain value remains below the calculated threshold value of 1μm^{-1}. Therefore, the reported results might benchmark the onset of population inversion by three-photon absorption of intense off-resonance ultrashort laser pulses like the ones developed in references [32, 129]. Additionally the pump intensity required to achieve lasing emission depends on the calculated threshold gain. The threshold gain was calculated using Equation 2.11 for the average wire parameters in the lasing arrays (blue dots in Figure 5.8). The threshold gain is plotted as a function of the measured pump threshold intensity

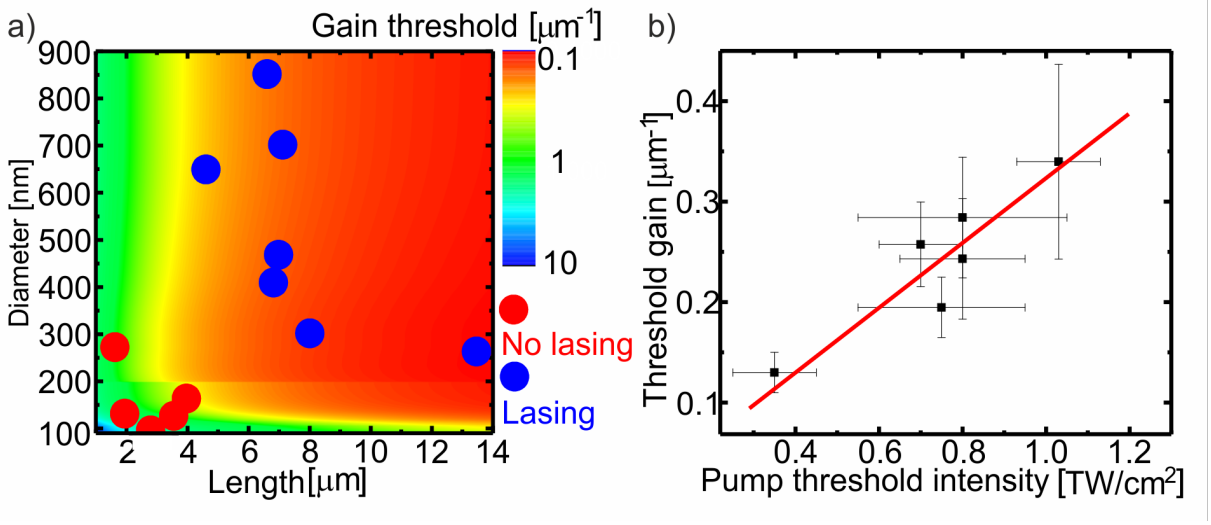

Figure 5.8: a) The contour plot depicts the calculated threshold gain values as a function of the wire diameter and length. The dots correspond to average NW diameter and length in the arrays used in the experiments. Blue dots mark the parameters for which lasing was achieved in the experiment, whereas red dots correspond to arrays with average NW parameters for which no lasing was observed. b) The calculated threshold gain vs. experimentally determined pump threshold intensity. The red line is a guide to the eye.

in Fig. 5.8 b. The uncertainties in estimating the pump threshold intensity from the experimental data determine the horizontal error bars and the vertical error bars account for variation of the gain threshold due to statistical variations of the wire parameters within different arrays. Applying a linear regression the data coincides within the error bars with the linear trend. Therefore, the lower theoretical threshold gain values for an average single wire in the array corresponds to the lower pump intensity needed to achieve lasing. This indicates that single NW properties determine the lasing capabilities of NW arrays in our experiments.

Hence, the influence of interwire coupling on lasing properties of an array remains an open question and will be discussed in the next part. Coupling effects are expected when wires are in close vicinity, i.e. an efficient interaction via the evanescent fields is possible. The spatial scale of evanescent fields as a function of the NW diameter is estimated using the solution for eigenmodes in a sub-wavelength step index cylindrical waveguide [166]. It is expected that coupling effects are the strongest in arrays with thin wires, due to the lower field localization and the shorter interwire distance for thin nanowires (see Fig. 5.1). Moreover, it can be expected that coupling between the wires might enable lasing for wires with diameters less than 200 nm where single wire lasing is not possible. For a single NW with a diameter of 100 nm (radius 50nm), the magnitude of the evanescent field halves after 30 nm measured from the surface. This corresponds to less than half the mean free space of 100 nm between the NWs. Thus, by considering the evanescent field formed outside the wire it is very unlikely that neighbouring wires can affect or couple with each other.

Furthermore, the efficiency of the interwire light coupling depends on the mutual phase shift

between the nanocavity guided modes and thus on the propagation constant β [167]. The propagation constant β for cylindrical nano-waveguides depends on the NW diameter and the refractive index [168], which is for excited ZnO NWs a function of the carrier density [32, 37]. Diameters of individual wires and thus the propagation constant of neighboring wires are not identical for the investigated samples. Eventually, the significant phase mismatch leads to a low coupling efficiency in the NW array. Note, that the coupling of the guided modes is considered in perfectly periodic NW arrays, where the formation of photonic crystal Bloch modes result in a photonic band structure [169], which can be ignored in the case of the used arrays.
In summary this section showed that lasing in VPT-grown arrays of vertically aligned NWs is possible when the individual NW of the array are longer than $5\,\mu$m and their diameter exceed 200 nm because the threshold for lasing remains below the damage threshold in this cases. The lasing characteristics from vertical aligned NW arrays is very similar to the case of single NW lasing. Thus, the onset of lasing can be determined by a weak pronounced kink in the output vs. input signal and the spectral narrowing of the emission. A comparison of the calculated gain thresholds using averaged wire parameters and the experimentally obtained threshold pump intensity reveal, that single wire parameters determine the onset of lasing in NW arrays. Calculations of the evanescent field of the guided modes outside the wire show, that the field extension is not sufficient enough in order to establish an efficient cross-talk between two neighbouring wires. Furthermore, considerations on the phase matching of the guided modes in neighbouring wires, which are necessary for interwire coupling, reveal that due to the diameter and refractive index dependent propagation constant β the coupling might be very inefficient in the case of these NW arrays. Thus, it is concluded that single wire parameters define the emission properties of vertically aligned ZnO NW arrays.

5.4 Conclusion

In this chapter ZnO NW lasing was demonstrated, using optical pumping with strong light fields provided by femtosecond laser pulses in a broad spectral range from the near to the mid-IR. The onset of lasing in single NW is determined by a threshold behaviour of the NUV emission as a function of the pump laser intensity, together with the appearance of Fabry-Pérot modes in the emission spectra. Both is accompanied by the dominant emission from the end facets of the nanowire instead of homogenous emission from the NW body. The laser threshold intensity roughly the same ($0.7\,\mathrm{TW/cm^2}$) in the case when near or mid-IR pump pulses at 0,8 or $3.6\,\mu$m, respectively. The wavelength dependence of pump laser threshold intensity in ZnO was investigated using arrays of randomly oriented NWs. The experiments revealed that this threshold is nearly independent for wavelengths between 0.8 and $4\,\mu$m. Because a large number of wires were excited in the experiment, the emission from the array is given by a superpo-

sition of many single NW laser emitters. Therefore, the onset of lasing could no longer be determined by the appearance of Fabry-Pérot modes or the emission yield as a function of the pump intensity which did not show a clear kink anymore. Instead the spectral narrowing of the emission spectrum was used to determine the threshold pump intensity, which occurs when lasing sets in. The wavelength independence of the carrier generation process and a Keldysh parameter smaller than 1 (γ=0.5 for λ=3.6 μm) proves that tunneling excitation was the dominant excitation mechanism. This results published in 2019 was, to best of my knowledge, the first demonstration of a semiconductor laser optically pumped in the tunneling regime [154]. The occurrence of lasing could be experimentally confirmed using nano- and microwires made from the material CdS and $CsPbBr_3$ Perovskite, respectively. This proved unambiguously that strong light field pumped lasing is a general physical effect in semiconductors not exclusively linked to ZnO material.

Experiments revealed a very similar threshold pump intensity of single nanowires and arrays. This raised the question about the role of interwire coupling. Therefore arrays formed by nanowires with differences in length, diameter and interwire spacing were investigated and the possibility of lasing as a function of the wire parameter was determined. The results show that the onset of lasing can be well predicted by the averaged wire parameters. Thus, lasing is only possible in arrays of wires with a minimum length and/or diameter of 5 μm and 200 nm before overcoming the damage threshold, respectively. Calculations of the evanescent fields of the guided modes in the nano waveguides and considerations of the phasematching condition between neighboring wires confirmed that interwire coupling is very unlikely and consequently the single NWs of the array define the emission properties of the VPT-grown NW array.

Beside the demonstration of nearly pump wavelength independent optically pumped lasing in the technologically promising nanowire material system, the results of this chapter show the possibility of Zener tunneling in nanoscale semiconductors and thus demonstrates the possibility of nanoscale petahertz electronics.

Chapter 6

Summary

The semiconductor material ZnO (3.2 eV band gap) was irradiated with intense laser light in the wide spectral range from the near-IR (0.8 μm, 1.5 eV) to the far-IR (10 μm, 0.13 eV). High harmonic generation (HHG) and lasing emission were detected to investigate the effect of free carriers on the laser field induced nonlinear current and light absorption. The density of excited carriers was estimated using a hybrid Keldysh-Drude model covering interband as well as intraband free carrier absorption rates.

Experiments on HHG from mid-IR laser pulses at 3.2 μm in highly excited semiconductor ZnO revealed a spectral blue shift of the harmonic signal by roughly 10 nm when the free carrier density is increased by two orders of magnitude from 0.1 to $11 \cdot 10^{24}\, m^{-3}$. Increasing the excited carrier density above the Mott-density of ZnO ($2 \cdot 10^{24}\, m^{-3}$) the near ultraviolet photoluminescence reveals a phase transition to an electron-hole-plasma (EHP).

A pump-probe experiment, using mid-IR laser pulses at 3.2 μm for pump and probe, was applied to investigate the transient modifications on the high harmonic generation process upon high photo-carrier-doping. The high harmonic signal shows modulations as a function of the pump-probe delay which oscillation frequencies at 3, 7 and 10 THz overlap with E_2 coherent optical phonon modes in ZnO. The coherent phonon excitation is impulsive, since phonon oscillation modes with a higher oscillation frequency vanish when the excitation pump pulse were temporally stretched. The symmetry properties and pump pulse intensity dependence of the lattice vibrations contradicts to the expected behaviour according to the Raman formalism. Therefore, it is assumed that the coherent optical phonons are excited by a displacive mechanism where the lattice displacement is initiated by interatomic forces as a result of the sudden change of the electric structure upon strong electron excitation. The dependence of the harmonic signal modulations on the pump and probe pulse intensity revealed the invasive nature of the probe method, i.e. the pump as well as the probe pulse determine the vibrational state of the lattice. Furthermore, investigations of the HHG efficiency as a function of the free carrier

density reveal a drop after reaching a threshold carrier density of roughly $0.4 \cdot 10^{24}\, m^{-3}$. Long pump-probe delay measurements up to 450 ps confirmed that the HHG efficiency recovery rate match to the spontaneous electron recombination rate in ZnO of roughly 110 ps. Thus, the free electrons cause the drop of the HHG efficiency.

Experiments with carrier envelope phase (CEP) controllable few cycle mid-IR laser pulses at $3.2\,\mu$m aimed to investigate the effect of the CEP on the HHG-process. The wide laser spectrum enables the overlapping of neighboring high harmonic orders, this leads to interference as a function of the CEP and the group delay dispersion of the driving laser pulse. Detecting the interferences in the high harmonic emission spectrum depicts a simple method to measure the CEP of mid-IR laser pulses.

Another focus of this work investigated lasing in polycrystalline ZnO thin films and ZnO nanowires (NWs), in order to study the interaction between strong light fields and condensed matter far from any electronic resonance.

Morphological features and the role of ion doping as well as the laser polarization were studied in NW arrays and ZnO thin films. The samples were irradiated with $0.8\,\mu$m light and electron excitation happend via a three photon absorption process. Using vertically aligned NW arrays grown by a vapour-phase-transport technique, it was shown that the emission properties can be determined from the single wire properties and interwire coupling effects can be neglected. Aluminium doping an intrinsic ZnO thin film with 0.5åt.%Aluminium atoms reduced the pump threshold intensity from 1.3 to $0.95\,\mathrm{TW/cm^2}$ by a factor of 1.4 compared to the intrinsic film. Measuring the photoluminescence as a function of the laser ellipticity showed a 1.8 times lower three photon absorption coefficient for circular compared to linear polarized light. These results demonstrated, that measuring the laser ellipticity dependent photoluminescence can be used as very simple method to determine single- and multiphoton absorption coefficients.

Lasing was demonstrated in polycrystalline ZnO thin films as well as single NW and NW arrays upon optical pumping in a wide spectral range from the near ($0.8\,\mu$m, 1.5 eV) to the far-IR ($10\,\mu$m, 0.13 eV). Note, this corresponds to a ZnO band gap (3.2 eV) to laser photon energy ratio between 3 and 26. Consequently, interband electron excitation is performed by the absorption of multiple photons as well as (Zener) tunneling. The NUV-lasing emission from the films and NWs was confirmed by a abrupt emission yield increase and spectral narrowing as well as the transition from a slow to a fast decaying temporal signal when the threshold pump intensity was reached. The onset of lasing emission is linked to gain, which sets in when a characteristic electron density of $2 \cdot 10^{25}$ is excited in the ZnO. Using the experimentally observed onset of lasing emission to monitor the excited carrier density, the highly nonlinear light absorption in ZnO material was investigated as function of the pump laser wavelength. The experiments revealed that the pump threshold intensity reduces with increasing pump wavelength. Comparing the experimental results with theoretical calculations that include interband- and intra-absorption

rates using the Keldysh and Drude formalism revealed the important role of electron impact excitation upon intraband free carrier absorption and an electron-electron scattering time of 5 fs. The electron acceleration scales beneficial towards longer wavelengths where interband electron excitation happens predominately via Zener tunneling.

In frame of this thesis it was demonstrated the first time to my knowledge that optically pumped upconversion lasing can be realised in semiconductors when the band gap to pump photon energy ratio is up to 26. Furthermore, this was the first demonstration of a laser, optically pumped in the (Zener) tunneling regime.

Regarding the application of light wave driven electronics where strong light fields are applied to condensed matter, the effects of high free carrier densities on the absorption process and the coherent electron motion have to be taken into account. Therefore, the results of this thesis are from striking importance for further developing light wave driven electronics in condensed matter.

Chapter 7

Future perspectives

The samples used in the work presented on the previous pages had one common feature, the geometrical size of the material is larger than the exciton Bohr-radius [12]. Reducing the size of the material below the limit of the excition Bohr-radius leading to electronic confinement, bringing up interesting quantum effects. For example, the confinement of the electron wavefunction leads to an enhanced exciton binding energy which is a promising feature for light emitting applications. The confinement can be achieved in one, two or three dimensions leading to 2D, 1D or 0D materials, respectively. This chapter will briefly dare an outlook on possible experiments based on already performed experiments using 2D and 0D materials.

2D-materials

2D-materials are formed by a single layer of atoms. Very prominent representatives of this class of materials are graphene (carbon) [170], MoS_2/$MoSe_2$/WS_2/WSe_2 (transition metal dichalgonides, TMD) [171] or Ruddlesden-Poper phase halide perovskite [172]. Because of their unique electronic structure this materials are promising for cost effective and more power efficient spintronic and valleytronic applications [170, 171]. Using this materials to study high harmonic generation excludes propagation effects and purely the nonlinear light matter interaction can be studied. HHG in solids is based on the motion of the electron driven by the strong field of the laser pulse, here 2D materials provide an ideal platform to study the Berry-curvature [105, 106]. Furthermore the well known chiral helicity under single photon excitation, leading to valley polarization, can perspectively used to study excitation selection rules for strong field excitation channels.

The μ-PL setup shown in Figure 5.2 b was adopted to HHG experiments (see Fig. 7.1 a) to enable experiments with well defined specimens (see Fig. 7.1 b), i.e. to distinguish between single and multilayer of 2D materials. Figure7.1 c depicts a measured high harmonic spectra up to the 16^{th} order from a WS_2 sample.

[12] 1.8 nm for ZnO

Using HHG spectroscopy in monolayer TMD samples will help to merge the fields of light wave electronics with spin- and valleytronics [173, 174, 175].

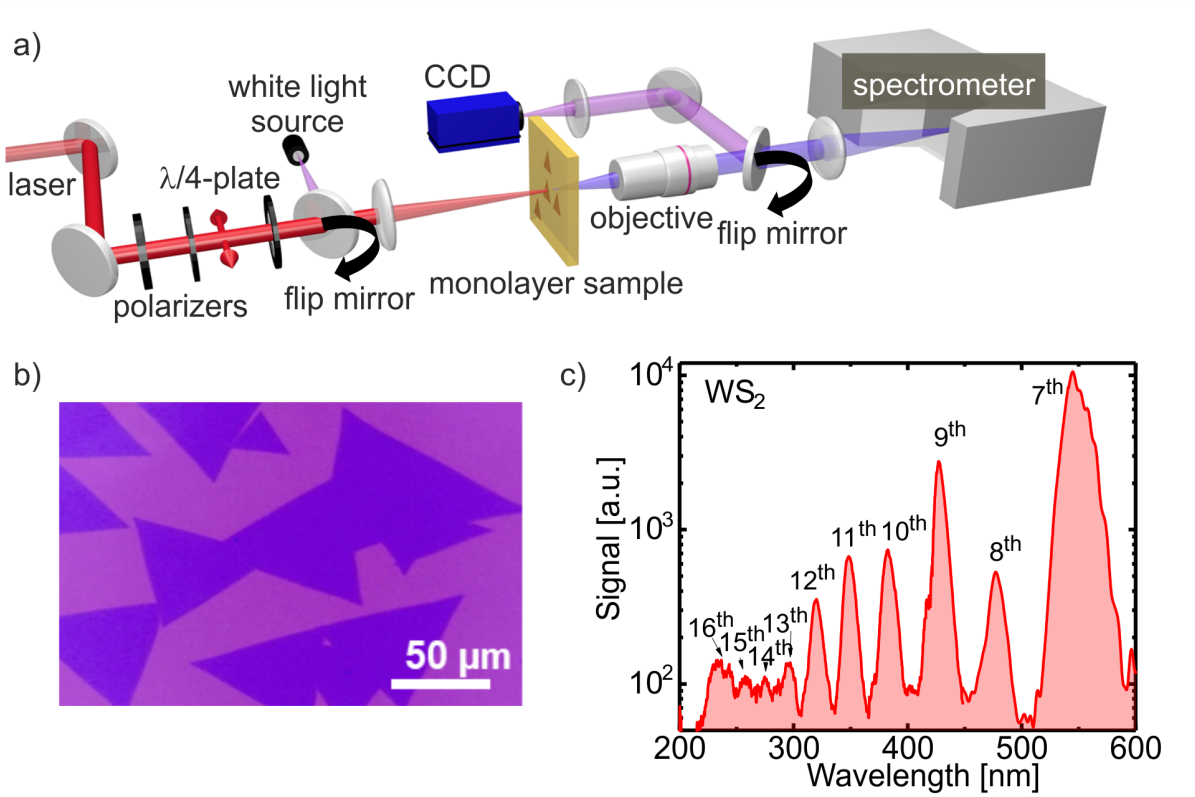

Figure 7.1: a) μ-HHG setup: combination of a high resolution microscope and HHG setup. The laser is power attenuated using two wire grid polarizer and focused onto the 2D-materials using a f=25mm CaF_2 lens. The monolayer TMD samples are grown on saphire substrate. The high harmonics are generated in the TMD sample are collected in transmission geometry using a x50 long working distance objective and focused onto the entrance slit of the spectrometer. Using a white light source and a CCD camera the same objective was used to image the sampe. b) Light microscope image of monolayer sample. c) Detected high harmonic spectrum from a WS_2 sample.

0D-materials

Confining the electron motion in all 3 dimensions a zero dimensional (0D) material is formed, also known as quantum dots (QD). QDs are formed by a periodic arrangement of atom but due to the confinement the electronic structure is given by discrete levels. QD are an ideal intermediate system between an atom/molecule with a discrete electronic structure and a solid crystal characterized by electronic bands as a result of periodic arrangement of the atoms.

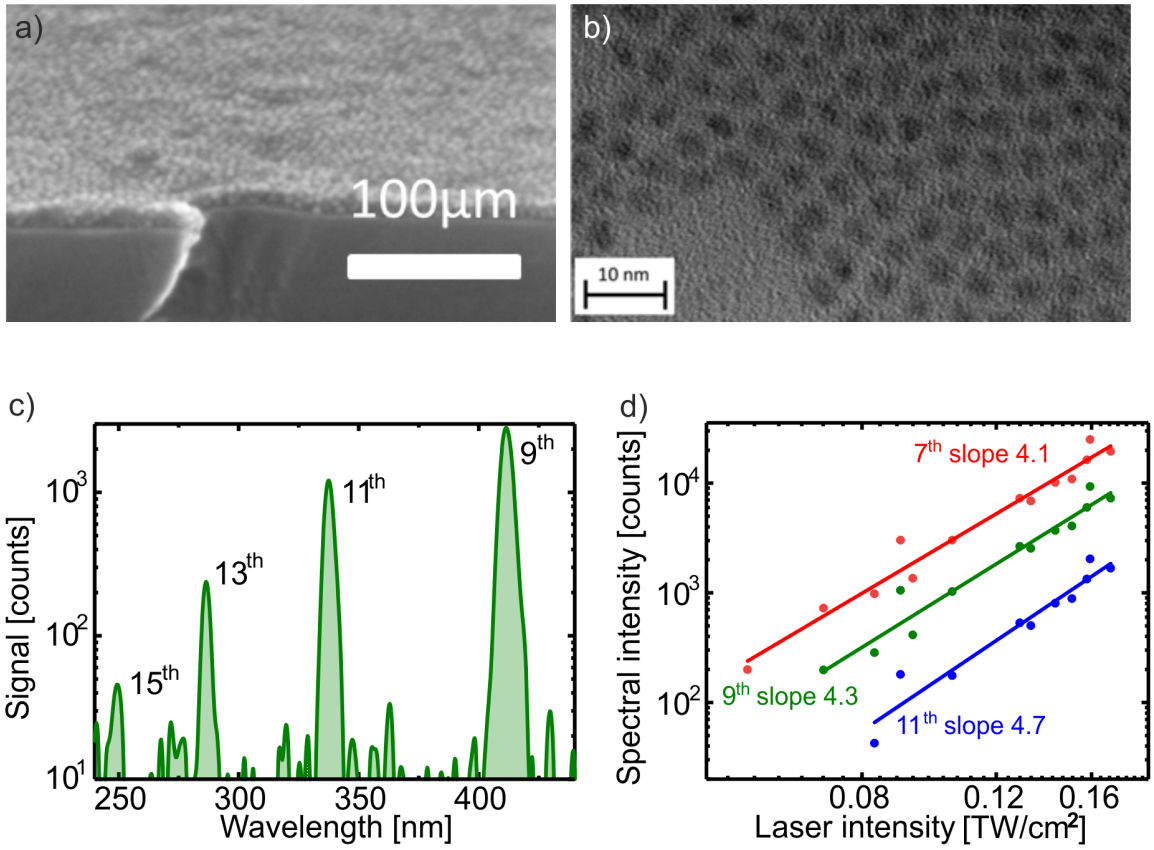

Figure 7.2: a) Transmission electron microscope (TEM) image of spin casted quantum dots (QD) on a sapphire substrate. The image reveal that the QD form a homogenous film of three layers. b) TEM image of single QD, from the image the diameter of 4 nm can be determined. c) High harmonic spectrum generated in QD-film by a mid-IR femtosecond laser pulse at 3.75 μm. d) Integrated signal of each harmonic as a function of the mid-IR laser intensity. The different harmonic orders show a very similiar dependence on the laser intensity revealing the nonpertubative origin.

Figure 7.2 a and b depicts transmission electron microscope (TEM) images of a film formed by 3 layers of CdSe QDs and individual CdSe QDs, respectively. Generating HHG in quantum confined system offers the possibility to bridge the understanding of HHG from an atom to the case when a periodic structure is used. Figure 7.2 c shows a measured harmonic spectrum generated by mid-IR laser at 3.5 μm. The non-pertubative generation mechanism was proven by measuring a similar power scaling of harmonics 7^{th}, 9^{th} and 11^{th} with the laser intensity (see Figure 7.2 d).

Beside HHG as a result of an interplay between intra- and interband contributions, due to a low work function of 5.6 eV in CdSe the ionization of free electrons and thus a HHG mechanism comparable to gases is possible. Time dependent density functional theory calculations will help to unrevealed the underlying generation mechanism.

Bibliography

[1] G. S. Singhal, G. Renger, S.K. Sopory, and K.D. Irrgang. *Concepts in Photobiology - Photosynthesis and Photomorphogenesis*. Springer Science & Business Media, Berlin Heidelberg, 2012.

[2] D. M. Chapin, C. S. Fuller, and G. L. Pearson. A new silicon p-n junction photocell for converting solar radiation into electrical power. *J. Appl. Phys.*, 25(5):676–677, 1954.

[3] A. Einstein. Über einen die Erzeugung und Verwandlung des Lichtes betreffenden heuristischen Gesichtspunkt. *Annalen der Physik*, 322(6):132–148, 1905.

[4] M. Göppert-Mayer. Über Elementarakte mit zwei Quantensprüngen. *Annalen der Physik*, 401(3):273–294, 1931.

[5] C. Zener and R. H. Fowler. A theory of the electrical breakdown of solid dielectrics. *Proceedings of the Royal Society of London. Series A, Containing Papers of a Mathematical and Physical Character*, 145(855):523–529, 1934.

[6] W. Kaiser and C. G. B. Garrett. Two-photon excitation in CaF_2: EU^{2+}. *Phys. Rev. Lett.*, 7:229–231, 1961.

[7] W. R. Zipfel, R. M. Williams, and W. W. Webb. Nonlinear magic: multiphoton microscopy in the biosciences. *Nat. Biotechnol.*, 21(11):1369–1377, 2003.

[8] F. Helmchen and W. Denk. Deep tissue two-photon microscopy. *Nat. Methods*, 2(12):932–940, 2005.

[9] H. Kroemer. Nobel prize laureates bibliography. Downloaded 03 May 2020, https://www.nobelprize.org/prizes/physics/2000/kroemer/biographical/, 2000.

[10] M. Garg, M. Zhan, T. T. Luu, H. Lakhotia, T. Klostermann, A. Guggenmos, and E. Goulielmakis. Multi-petahertz electronic metrology. *Nature*, 538(7625):359–363, 2016.

[11] H. Mashiko, Y. Chisuga, I. Katayama, K. Oguri, H. Masuda, J. Takeda, and H. Gotoh. Multi-petahertz electron interference in Cr:Al_2O_3 solid-state material. *Nat. Commun.*, 9(1):1468, 2018.

[12] J. Schoetz, Z. Wang, E. Pisanty, M. Lewenstein, M. F. Kling, and M. F. Ciappina. Perspective on petahertz electronics and attosecond nanoscopy. *ACS Phot.*, 6(12):3057–3069, 2019.

[13] S. Sederberg, D. Zimin, S. Keiber, F. Siegrist, M. S. Wismer, V. S. Yakovlev, I. Floss, C. Lemell, J. Burgdörfer, M. Schultze, F. Krausz, and N. Karpowicz. Attosecond optoelectronic field measurement in solids. *Nat. Commun.*, 11(1):430, 2020.

[14] O. Schubert, M. Hohenleutner, F. Langer, B. Urbanek, C. Lange, U. Huttner, D. Golde, T. Meier, M. Kira, S. W. Koch, and R. Huber. Sub-cycle control of terahertz high-harmonic generation by dynamical Bloch oscillations. *Nat. Photonics*, 8(2):119–123, 2014.

[15] F. Schlaepfer, M. Lucchini, S. A. Sato, M. Volkov, L. Kasmi, N. Hartmann, A. Rubio, L. Gallmann, and U. Keller. Attosecond optical-field-enhanced carrier injection into the GaAs conduction band. *Nat. Phys.*, 14(6):560–564, 2018.

[16] A. Schiffrin, T. Paasch-Colberg, N. Karpowicz, V. Apalkov, D. Gerster, S. Mühlbrandt, M. Korbman, J. Reichert, M. Schultze, S. Holzner, J. V. Barth, R. Kienberger, R. Ernstorfer, V. S. Yakovlev, M. I. Stockman, and F. Krausz. Optical-field-induced current in dielectrics. *Nature*, 493(7430):70–74, 2013.

[17] S. Ghimire, A. D. DiChiara, E. Sistrunk, P. Agostini, L. F. DiMauro, and D. A. Reis. Observation of high-order harmonic generation in a bulk crystal. *Nature*, (7):138–141, 2011.

[18] A. A. Lanin, E. A. Stepanov, A. V. Mitrofanov, D. A. Sidorov-Biryukov, A. B. Fedotov, and A. M. Zheltikov. High-order harmonic analysis of anisotropic petahertz photocurrents in solids. *Opt. Lett.*, 44(8):1888–1891, 2019.

[19] L. V. Keldysh. Ionization in the field of a strong electromagnetic wave. *Sov. Phys. JETP*, 20:1307–1314, 1965.

[20] P. Balling and J. Schou. Femtosecond-laser ablation dynamics of dielectrics: basics and applications for thin films. *Rep. Prog. Phys.*, 76(3):036502, 2013.

[21] N. W Ashcroft and D. N Mermin. *Solid State Physics*. Oldenbourg Verlag, München, improved edition, 2012.

[22] D. Ristau. *Laser-Induced Damage in Optical Materials*. Taylor & Francis, 2014.

[23] M. Schultze, K. Ramasesha, C.D. Pemmaraju, S.A. Sato, D. Whitmore, A. Gandman, J. S. Prell, L. J. Borja, D. Prendergast, K. Yabana, D. M. Neumark, and S. R. Leone. Attosecond band-gap dynamics in silicon. *Science*, 346(6215):1348–1352, 2014.

[24] A. Sommer, E. M. Bothschafter, S. A. Sato, C. Jakubeit, T. Latka, O. Razskazovskaya, H. Fattahi, M. Jobst, W. Schweinberger, V. Shirvanyan, V. S. Yakovlev, R. Kienberger, K. Yabana, N. Karpowicz, M. Schultze, and F. Krausz. Attosecond nonlinear polarization and light-matter energy transfer in solids. *Nature*, 534(7605):86–90, 2016.

[25] P. A. Zhokhov and A. M. Zheltikov. Field-cycle-resolved photoionization in solids. *Phys. Rev. Lett.*, 113:133903, Sep 2014.

[26] K. Yabana, T. Sugiyama, Y. Shinohara, T. Otobe, and G. F. Bertsch. Time-dependent density functional theory for strong electromagnetic fields in crystalline solids. *Phys. Rev. B*, 85:045134, 2012.

[27] S. Y. Kruchinin. Non-Markovian pure dephasing in a dielectric excited by a few-cycle laser pulse. *Phys. Rev. A*, 100:043839, 2019.

[28] O. Sergaeva, V. Gruzdev, D. Austin, and E. Chowdhury. Ultrafast excitation of conduction-band electrons by high-intensity ultrashort laser pulses in band-gap solids: Vinogradov equation versus drude model. *J. Opt. Soc. Am. B*, 35(11):2895–2905, 2018.

[29] G. P. Agrawal and N. K. Dutta. *Semiconductor Lasers*. Springer Science & Business Media, Berlin Heidelberg, 2013.

[30] C. F. Klingshirn. *Semiconductor Optics*. Springer Science & Business Media, Berlin Heidelberg, 2012.

[31] C. F. Klingshirn, A. Waag, A. Hoffmann, and J. Geurts. *Zinc Oxide - From Fundamental Properties Towards Novel Applications*. Springer Science & Business Media, Berlin Heidelberg, 2010.

[32] M. A. M. Versteegh, T. Kuis, H. T. C. Stoof, and J. I. Dijkhuis. Ultrafast screening and carrier dynamics in ZnO: Theory and experiment. *Phys. Rev. B*, 84:035207, 2011.

[33] C. Klingshirn, J. Fallert, O. Gogolin, M. Wissinger, R. Hauschild, M. Hauser, H. Kalt, and H. Zhou. Linear and nonlinear optics, dynamics, and lasing in ZnO bulk and nanostructures. *J. Lumi.*, 128(5–6):792 – 796, 2008.

[34] M. A. Zimmler, F. Capasso, S. Müller, and C. Ronning. Optically pumped nanowire lasers: invited review. *Semicond. Sci. Technol.*, 25(2):024001, 2010.

[35] C. Klingshirn. ZnO: Material, Physics and Applications. *Chem. Phys. Chem.*, 2007.

[36] C. Klingshirn, R. Hauschild, J. Fallert, and H. Kalt. Room-temperature stimulated emission of ZnO: Alternatives to excitonic lasing. *Phys. Rev. B*, 75:115203, 2007.

[37] M. Wille, C. Sturm, T. Michalsky, R. Röder, C. Ronning, R. Schmidt-Grund, and M. Grundmann. Carrier density driven lasing dynamics in ZnO nanowires. *Nanotechnology*, 27(22):225, 2016.

[38] M. A. M. Versteegh, D. Vanmaekelbergh, and J. I. Dijkhuis. Room-Temperature Laser Emission of ZnO Nanowires Explained by Many-Body Theory. *Phys. Rev. Lett.*, 108:157402, 2012.

[39] R. Röder, T. P. H. Sidiropoulos, C. Tessarek, S. Christiansen, R. F. Oulton, and C. Ronning. Ultrafast Dynamics of Lasing Semiconductor Nanowires. *Nano Letters*, 15(7):4637–4643, 2015.

[40] R. Yan, D. Gargas, and P. Yang. Nanowire photonics. *Nat. Photonics*, 3(10):569–576, 2009.

[41] R. Röder and C. Ronning. Review on the dynamics of semiconductor nanowire lasers. *Semicond. Sci. Technol.*, 33(3):033001, 2018.

[42] Yue-De Yang, Min Tang, Fu-Li Wang, Zhi-Xiong Xiao, Jin-Long Xiao, and Yong-Zhen Huang. Whispering-gallery mode hexagonal micro-/nanocavity lasers. *Photon. Res.*, 7(5):594–607, 2019.

[43] T. Michalsky, M. Wille, M. Grundmann, and R. Schmidt-Grund. Tunable and switchable lasing in a ZnO microwire cavity at room temperature. *J. Phys. D: Appl. Phys.*, 51(42):425305, 2018.

[44] C. C. Kuo, W.-R. Liu, B. H. Lin, W. F. Hsieh, C.-H. Hsu, W. C. Lee, M. Hong, and J. Kwo. Vertical-cavity and randomly scattered lasing from different thicknesses of epitaxial zno films grown on Y_2O_3-buffered Si (111). *Opt. Express*, 21(2):1857–1864, 2013.

[45] M. Kawasaki, A. Ohtomo, I. Ohkubo, H. Koinuma, Z.K. Tang, P. Yu, G.K.L. Wong, B.P. Zhang, and Y. Segawa. Excitonic ultraviolet laser emission at room temperature from naturally made cavity in zno nanocrytal thin films. *Mat. Sci. Engi.: B*, 56(2):239 – 245, 1998.

[46] Z. K. Tang, M. Kawasaki, A. Ohtomo, H. Koinuma, and Y. Segawa. Self-assembled ZnO nano-crystals and exciton lasing at room temperature. *Journal of Crystal Growth*, 287(1):169 – 179, 2006.

[47] H. Cao, Y. G. Zhao, H. C. Ong, S. T. Ho, J. Y. Dai, J. Y. Wu, and R. P. H. Chang. Ultraviolet lasing in resonators formed by scattering in semiconductor polycrystalline films. *Appl. Phys. Lett.*, 73(25):3656–3658, 1998.

[48] S. F. Yu, C. Yuen, S. P. Lau, and H. W. Lee. Zinc oxide thin-film random lasers on silicon substrate. *Appl. Phys. Lett.*, 84(17):3244–3246, 2004.

[49] C. Cachoncinlle, C. Hebert, J. Perrière, M. Nistor, A. Petit, and E. Millon. Random lasing of ZnO thin films grown by pulsed-laser deposition. *Appl. Sur. Sci.*, 336:103 – 107, 2015. E-MRS 2014 Spring Meeting. Symposium J. Laser Interaction with Advanced Materials: Fundamentals and Applications.

[50] D. S. Wiersma. The physics and applications of random lasers. *Nat. Phys.*, 4(5):359–367, 2008.

[51] F. Luan, B. Gu, A. S. L. Gomes, K.-T. Yong, S. Wen, and P. N. Prasad. Lasing in nanocomposite random media. *Nano Today*, 10(2):168 – 192, 2015.

[52] R. Sapienza. Determining random lasing action. *Nat. Rev. Phys.*, 1(11):690–695, 2019.

[53] K. Seeger. *Semiconductor Physics - An Introduction*. Springer Science & Business Media, Berlin Heidelberg, 2013.

[54] S. Richter, O. Herrfurth, S. Espinoza, M. Rebarz, M. Kloz, J. A. Leveillee, A. Schleife, S. Zollner, M. Grundmann, J. Andreasson, and R. Schmidt-Grund. Ultrafast dynamics of hot charge carriers in an oxide semiconductor probed by femtosecond spectroscopic ellipsometry, 2019. arXiv.

[55] B. E. Sernelius, K.-F. Berggren, Z.-C. Jin, I. Hamberg, and C. G. Granqvist. Band-gap tailoring of ZnO by means of heavy Al doping. *Phys. Rev. B*, 37:10244–10248, 1988.

[56] R. Buschlinger, M. Lorke, and U. Peschel. Coupled-mode theory for semiconductor nanowires. *Phys. Rev. Appl.*, 7:034028, 2017.

[57] J. P. Richters, J. Kalden, M. Gnauck, C. Ronning, C. P. Dietrich, H. von Wenckstern, M. Grundmann, J. Gutowski, and T. Voss. Modal gain and its diameter dependence in single-ZnO micro- and nanowires. *Semicond. Sci. Technol.*, 27(1):015005, 2011.

[58] C. Klingshirn, J. Fallert, H. Zhou, J. Sartor, C. Thiele, F. Maier-Flaig, D. Schneider, and H. Kalt. 65 years of ZnO research – old and very recent results. *Phys. Status Solidi (B)*, 247(6):1424–1447, 2010.

[59] M. Ferray, A. Huillier, X. F. Li, L. A. Lompre, G. Mainfray, and C. Manus. Multiple-harmonic conversion of 1064 nm radiation in rare gases. *J. Phys. B*, 21(3):L31–L35, 1988.

[60] Ch. Spielmann, N. H. Burnett, S. Sartania, R. Koppitsch, M. Schnürer, C. Kan, M. Lenzner, P. Wobrauschek, and F. Krausz. Generation of coherent x-rays in the water window using 5-femtosecond laser pulses. *Science*, 278(5338):661–664, 1997.

[61] T. Popmintchev, M.-C. Chen, D. Popmintchev, P. Arpin, S. Brown, S. Ališauskas, G. Andriukaitis, T. Balčiunas, O. D. Mücke, A. Pugzlys, A. Baltuška, B. Shim, S. E. Schrauth, A. Gaeta, C. Hernández-García, L. Plaja, A. Becker, A. Jaron-Becker, M. M. Murnane, and H. C. Kapteyn. Bright coherent ultrahigh harmonics in the keV x-ray regime from mid-infrared femtosecond lasers. *Science*, 336(6086):1287–1291, 2012.

[62] C. Winterfeldt, Ch. Spielmann, and G. Gerber. Colloquium: Optimal control of high-harmonic generation. *Rev. Mod. Phys.*, 80:117–140, 2008.

[63] A. H. Chin, O. G. Calderón, and J. Kono. Extreme midinfrared nonlinear optics in semiconductors. *Phys. Rev. Lett.*, 86:3292–3295, 2001.

[64] M. Sivis, M. Taucer, G. Vampa, K. Johnston, A. Staudte, A. Y. Naumov, D. M. Villeneuve, C. Ropers, and P. B. Corkum. Tailored semiconductors for high-harmonic optoelectronics. *Science*, 357(6348):303–306, 2017.

[65] K. Imasaka, T. Kaji, T. Shimura, and S. Ashihara. Antenna-enhanced high harmonic generation in a wide-bandgap semiconductor ZnO. *Opt. Express*, 26(16):21364–21374, 2018.

[66] G. Vampa, B. G. Ghamsari, S. Siadat Mousavi, T. J. Hammond, A. Olivieri, E. Lisicka-Skrek, A. Yu Naumov, D. M. Villeneuve, A. Staudte, P. Berini, and P. B. Corkum. Plasmon-enhanced high-harmonic generation from silicon. *Nat. Phys.*, 13(7):659–662, 2017.

[67] D. Franz, S. Kaassamani, D. Gauthier, R. Nicolas, M. Kholodtsova, L. Douillard, J.-T. Gomes, L. Lavoute, D. Gaponov, N. Ducros, S. Février, J. Biegert, L. Shi, M. Kovacev, W. Boutu, and H. Merdji. All semiconductor enhanced high-harmonic generation from a single nanostructured cone. *Sci. Rep.*, 9(1):5663, 2019.

[68] S. Ghimire and D. A. Reis. High-harmonic generation from solids. *Nat. Phys.*, 15(1):10–16, 2019.

[69] G. Vampa, C. R. McDonald, G. Orlando, D. D. Klug, P. B. Corkum, and T. Brabec. Theoretical analysis of high-harmonic generation in solids. *Phys. Rev. Lett.*, 113:073901, 2014.

[70] A. A. Lanin, E. A. Stepanov, A. B. Fedotov, and A. M. Zheltikov. Mapping the electron band structure by intraband high-harmonic generation in solids. *Optica*, 4(5):516–519, 2017.

[71] S. Gholam-Mirzaei, J. Beetar, and M. Chini. High harmonic generation in ZnO with a high-power mid-IR OPA. *Appl. Phys. Lett.*, 110(6):061101, 2017.

[72] R. Hollinger,, V. Shumakova,, A. Pugzlys,, A. Baltuska,, S. Khujanov,, Ch. Spielmann,, and D. Kartashov,. High-order harmonic generation traces ultrafast coherent phonon dynamics in ZnO. *EPJ Web Conf.*, 205:02025, 2019.

[73] R. Hollinger, D. Hoff, P. Wustelt, S. Skruszewicz, Y. Zhang, H. Kang, D. Würzler, T. Jungnickel, M. Dumergue, A. Nayak, R. Flender, L. Haizer, M. Kurucz, B. Kiss, S. Kühn, E. Cormier, C. Spielmann, G. G. Paulus, P. Tzallas, and M. Kübel. Carrier-envelope-phase measurement of few-cycle mid-infrared laser pulses using high harmonic generation in ZnO. *Opt. Express*, 28(5):7314–7322, 2020.

[74] K. Werner, M. G. Hastings, A. Schweinsberg, B. L. Wilmer, D. Austin, C. M. Wolfe, M. Kolesik, T. R. Ensley, L. Vanderhoef, A. Valenzuela, and E. Chowdhury. Ultrafast mid-infrared high harmonic and supercontinuum generation with n_2 characterization in zinc selenide. *Opt. Express*, 27(3):2867–2885, 2019.

[75] R. W. Boyd. *Nonlinear Optics*. Academic Press, Amsterdam, Boston, 2013.

[76] J. M. Calleja and Manuel Cardona. Resonant Raman scattering in ZnO. *Phys. Rev. B*, 16:3753–3761, 1977.

[77] T. C. Damen, S. P. S. Porto, and B. Tell. Raman effect in zinc oxide. *Phys. Rev.*, 142:570–574, 1966.

[78] T. Sander, S. Eisermann, B. K. Meyer, and P. J. Klar. Raman tensor elements of wurtzite ZnO. *Phys. Rev. B*, 85:165208, 2012.

[79] I. H. Lee, K. J. Yee, K. G. Lee, E. Oh, D. S. Kim, and Y. S. Lim. Coherent optical phonon mode oscillations in wurtzite ZnO excited by femtosecond pulses. *J. Appl. Phys.*, 93(8):4939–4941, 2003.

[80] C. Aku-Leh, J. Zhao, R. Merlin, J. Menéndez, and M. Cardona. Long-lived optical phonons in ZnO studied with impulsive stimulated Raman scattering. *Phys. Rev. B*, 71:205211, 2005.

[81] K. Ishioka, H. Petek, V. E. Kaydashev, E. M. Kaidashev, and O. V. Misochko. Coherent optical phonons of ZnO under near resonant photoexcitation. *J. Phys Cond. Matt.*, 22(46):465803, 2010.

[82] G. Lanzani, G. Cerullo, and S. D. Silvestri. *Coherent Vibrational Dynamics*. CRC Press, Boca Raton, Fla, 2007.

[83] Y.-X. Yan, E. B. Gamble, and K. A. Nelson. Impulsive stimulated scattering: General importance in femtosecond laser pulse interactions with matter, and spectroscopic applications. *The Journal of Chemical Physics*, 83(11):5391–5399, 1985.

[84] P. Y. Emelie, J. D. Phillips, B. Buller, and U. D. Venkateswaran. Free carrier absorption and lattice vibrational modes in bulk ZnO. *J. Elec. Mat.*, 35(4):525–529, 2006.

[85] W. A. Kutt, W. Albrecht, and H. Kurz. Generation of coherent phonons in condensed media. *IEEE J. Quan. Elec.*, 28(10):2434–2444, 1992.

[86] R. Merlin. Generating coherent THz phonons with light pulses. *Solid State Commun.*, 102(2):207 – 220, 1997. Highlights in Condensed Matter Physics and Materials Science.

[87] A. von Hoegen, R. Mankowsky, M. Fechner, M. Först, and A. Cavalleri. Probing the interatomic potential of solids with strong-field nonlinear phononics. *Nature*, 555(7694):79–82, 2018.

[88] M. Först, C. Manzoni, S. Kaiser, Y. Tomioka, Y. Tokura, R. Merlin, and A. Cavalleri. Nonlinear phononics as an ultrafast route to lattice control. *Nat. Phys.*, 7(11):854–856, 2011.

[89] K. Uchida, K. Nagai, N. Yoshikawa, and K. Tanaka. Inherent limit to coherent phonon generation under non-resonant light field driving, 2019.

[90] T. Sander, S. Eisermann, B. K. Meyer, and P. J. Klar. Raman tensor elements of wurtzite ZnO. *Phys. Rev. B*, 85:165208, 2012.

[91] R. Cuscó, E. Alarcón-Lladó, J.i Ibáñez, L. Artús, J. Jiménez, B. Wang, and M. J. Callahan. Temperature dependence of Raman scattering in ZnO. *Phys. Rev. B*, 75:165202, 2007.

[92] Z. Wang, H. Park, Y. H. Lai, J. Xu, C. I. Blaga, F. Yang, P. Agostini, and L. F. DiMauro. The roles of photo-carrier doping and driving wavelength in high harmonic generation from a semiconductor. *Nat. Commun.*, 8(1):1686, 2017.

[93] J. M. Szarko, J. K. Song, C. W. Blackledge, I. Swart, S. R. Leone, S. Li, and Y. Zhao. Optical injection probing of single ZnO tetrapod lasers. *Chem. Phys. Lett.*, 404(1–3):171 – 176, 2005.

[94] J. C. Johnson, K. P. Knutsen, H. Yan, M. Law, Y. Zhang, P. Yang, and R. J. Saykally. Ultrafast carrier dynamics in single ZnO nanowire and nanoribbon lasers. *Nano Letters*, 4(2):197–204, 2004.

[95] B. Wolter, M. G. Pullen, M. Baudisch, M. Sclafani, M. Hemmer, A. Senftleben, C. D. Schröter, J. Ullrich, R. Moshammer, and J. Biegert. Strong-field physics with mid-ir fields. *Phys. Rev. X*, 5:021034, 2015.

[96] S. Y. Kruchinin, F. Krausz, and V. S. Yakovlev. Colloquium: Strong-field phenomena in periodic systems. *Rev. Mod. Phys.*, 90:021002, 2018.

[97] J. Weisshaupt, V. Juvé, M. Holtz, S. Ku, M. Woerner, T. Elsaesser, S. Alisauskas, A. Pugzlys, and A. Baltuska. High-brightness table-top hard x-ray source driven by sub-100-femtosecond mid-infrared pulses. *Nat. Photonics*, 8(12):927–930, 2014.

[98] C. I. Blaga, J. Xu, A. D. DiChiara, E. Sistrunk, K. Zhang, P. Agostini, T. A. Miller, L. F. DiMauro, and C. D. Lin. Imaging ultrafast molecular dynamics with laser-induced electron diffraction. *Nature*, 483(7388):194–197, 2012.

[99] Z. Samsonova, S. Höfer, V. Kaymak, S. Ališauskas, V. Shumakova, A. Pugžlys, A. Baltuška, T. Siefke, S. Kroker, A. Pukhov, O. Rosmej, I. Uschmann, C. Spielmann, and D. Kartashov. Relativistic interaction of long-wavelength ultrashort laser pulses with nanowires. *Phys. Rev. X*, 9:021029, 2019.

[100] B. Wolter, M. G. Pullen, A.-T. Le, M. Baudisch, K. Doblhoff-Dier, A. Senftleben, M. Hemmer, C. D. Schröter, J. Ullrich, T. Pfeifer, R. Moshammer, S. Gräfe, O. Vendrell, C. D. Lin, and J. Biegert. Ultrafast electron diffraction imaging of bond breaking in di-ionized acetylene. *Science*, 354(6310):308–312, 2016.

[101] V. Shumakova, P. Malevich, S. Alisauskas, A. Voronin, A. M. Zheltikov, D. Faccio, D. Kartashov, A. Baltuska, and A. Pugzlys. Multi-millijoule few-cycle mid-infrared pulses through nonlinear self-compression in bulk. *Nat. Commun.*, 7(1):12877, 2016.

[102] M. Hemmer, M. Baudisch, A. Thai, A. Couairon, and J. Biegert. Self-compression to sub-3-cycle duration of mid-infrared optical pulses in dielectrics. *Opt. Express*, 21(23):28095–28102, 2013.

[103] S. Gholam-Mirzaei, J. E. Beetar, A. Chacón, and M. Chini. High-harmonic generation in ZnO driven by self-compressed mid-infrared pulses. *J. Opt. Soc. Am. B*, 35(4):A27–A31, Apr 2018.

[104] D. Franz. *High harmonic generation in crystals assisted by local field enhancement in nanostructures*. Theses, Université Paris-Saclay, May 2018.

[105] H. Liu, Y. Li, Y. S. You, S. Ghimire, T. F. Heinz, and D. A. Reis. High-harmonic generation from an atomically thin semiconductor. *Nat. Phys.*, 13(3):262–265, 2017.

[106] T. T. Luu and H. J. Wörner. Measurement of the Berry curvature of solids using high-harmonic spectroscopy. *Nat. Commun.*, 9(1):916, 2018.

[107] Y. S. You, Y. Yin, Y. Wu, A. Chew, X. Ren, F. Zhuang, S. Gholam-Mirzaei, M. Chini, Z. Chang, and S. Ghimire. High-harmonic generation in amorphous solids. *Nat. Commun.*, 8(1):724, 2017.

[108] Y. S. You, M. Wu, Y. Yin, A. Chew, X. Ren, S. Gholam-Mirzaei, D. A. Browne, M. Chini, Z. Chang, K. J. Schafer, M. B. Gaarde, and S. Ghimire. Laser waveform control of extreme ultraviolet high harmonics from solids. *Opt. Lett.*, 42(9):1816–1819, 2017.

[109] H. Shirai, F. Kumaki, Y. Nomura, and T. Fuji. High-harmonic generation in solids driven by subcycle midinfrared pulses from two-color filamentation. *Opt. Lett.*, 43(9):2094–2097, 2018.

[110] M. Garg, H. Y. Kim, and E. Goulielmakis. Ultimate waveform reproducibility of extreme-ultraviolet pulses by high-harmonic generation in quartz. *Nat. Photonics*, 12(5):291–296, 2018.

[111] P. Zu, Z. K. Tang, G. K. L. Wong, M. Kawasaki, A. Ohtomo, H. Koinuma, and Y. Segawa. Ultraviolet spontaneous and stimulated emissions from ZnO microcrystallite thin films at room temperature. *Solid State Commun.*, 103(8):459 – 463, 1997.

[112] D. M. Bagnall, Y. F. Chen, Z. Zhu, T. Yao, S. Koyama, M. Y. Shen, and T. Goto. Optically pumped lasing of ZnO at room temperature. *Appl. Phys. Lett.*, 70(17):2230–2232, 1997.

[113] S. F. Yu, C. Yuen, S. P. Lau, and H. W. Lee. Zinc oxide thin-film random lasers on silicon substrate. *Appl. Phys. Lett.*, 84(17):3244–3246, 2004.

[114] A. Mitra and R. K. Thareja. Photoluminescence and ultraviolet laser emission from nanocrystalline ZnO thin films. *J. Appl. Phys.*, 89(4):2025–2028, 2001.

[115] A.-S. Gadallah, K. Nomenyo, C. Couteau, D. J. Rogers, and G. Lérondel. Stimulated emission from ZnO thin films with high optical gain and low loss. *Appl. Phys. Lett.*, 102(17):171105, 2013.

[116] Ü. Özgür, A. Teke, C. Liu, S.-J. Cho, H. Morkoç, and H. O. Everitt. Stimulated emission and time-resolved photoluminescence in rf-sputtered ZnO thin films. *Appl. Phys. Lett.*, 84(17):3223–3225, 2004.

[117] X. Q. Zhang, I. Suemune, H. Kumano, J. Wang, and S. H. Huang. Surface-emitting stimulated emission in high-quality zno thin films. *J. Appl. Phys.*, 96(7):3733–3736, 2004.

[118] S. Cho, J. Ma, Y. Kim, Y. Sun, G. K. L. Wong, and J. B. Ketterson. Photoluminescence and ultraviolet lasing of polycrystalline ZnO thin films prepared by the oxidation of the metallic Zn. *Appl. Phys. Lett.*, 75(18):2761–2763, 1999.

[119] R. Matsuzaki, H. Soma, K. Fukuoka, K. Kodama, A. Asahara, T. Suemoto, Y. Adachi, and T. Uchino. Purely excitonic lasing in ZnO microcrystals: Temperature-induced transition between exciton-exciton and exciton-electron scattering. *Phys. Rev. B*, 96:125306, 2017.

[120] P. Zhang, W. Steelant, and M. Kumar, M.and Scholfield. Versatile photosensitizers for photodynamic therapy at infrared excitation. *J. Am. Chem. Soc.*, 129(15):4526–4527, 2007.

[121] M. C. Fischer, J. W. Wilson, F. E. Robles, and W. S. Warren. Invited review article: Pump-probe microscopy. *Rev. Sci.c Inst.*, 87(3):031101, 2016.

[122] J. Zhou, Z. Liu, and F. Li. Upconversion nanophosphors for small-animal imaging. *Chem. Soc. Rev.*, 41:1323–1349, 2012.

[123] B. Redding, M. A. Choma, and H. Cao. Speckle-free laser imaging using random laser illumination. *Nat. Photonics*, 6(6):355–359, 2012.

[124] D. A. Parthenopoulos and P. M. Rentzepis. Three-dimensional optical storage memory. *Science*, 245(4920):843–845, 1989.

[125] M. C. Larciprete and M. Centini. Second harmonic generation from ZnO films and nanostructures. *Appl. Phys. Rev.*, 2(3):–, 2015.

[126] R. Hollinger, D. Gupta, M. Zapf, M. Karst, R. Röder, I. Uschmann, U. Reislöhner, D. Kartashov, C. Ronning, and C. Spielmann. Polarization dependent multiphoton absorption in ZnO thin films. *J. Phys. D: Appl. Phys.*, 53(5):055102, 2019.

[127] E. Zolotoyabko. *Basic Concepts of X-Ray Diffraction*. John Wiley & Sons, New York, 2014.

[128] M. D.; Biersack J. P. Ziegler, J. F.; Ziegler. *SRIM, the Stopping and Range of Ions in Matter*. SRIM Company, 2008.

[129] Bing Gu, Jun He, Wei Ji, and Hui-Tian Wang. Three-photon absorption saturation in ZnO and ZnS crystals. *J. Appl. Phys.*, 103(7):073105, 2008.

[130] D. M. Bagnall, Y. F. Chen, Z. Zhu, T. Yao, M. Y. Shen, and T. Goto. High temperature excitonic stimulated emission from ZnO epitaxial layers. *Appl. Phys. Lett.*, 73(8):1038–1040, 1998.

[131] L. Bergman, X.-B. Chen, J. L. Morrison, J. Huso, and A. P. Purdy. Photoluminescence dynamics in ensembles of wide-band-gap nanocrystallites and powders. *J. Appl. Phys.*, 96(1):675–682, 2004.

[132] Y. Yang, H. Yan, Z. Fu, B. Yang, L. Xia, Y. Xu, J. Zuo, and F. Li. Photoluminescence investigation based on laser heating effect in ZnO-ordered nanostructures. *The Journal of Physical Chemistry B*, 110(2):846–852, 2006.

[133] J. Dai, M.-H. Yuan, J.-H. Zeng, Q.-F. Dai, S. Lan, C. Xiao, and S.-L. Tie. Three-photon-induced blue emission with narrow bandwidth from hot flower-like ZnO nanorods. *Opt. Express*, 23(22):29231–29244, 2015.

[134] I. D. W. Samuel, E. B. Namdas, and G. A. Turnbull. How to recognize lasing. *Nat. Photonics*, 3(10):546–549, 2009.

[135] A. E. Siegman. *Lasers*. University Science Books, Sausalito, California, 1986.

[136] M. S. Shamsi, M. Ahmadi, and M. Sabet. Al doped ZnO thin films; preparation and characterization. *Journal of Nanostructures*, 8(4):404–407, 2018.

[137] M. Lin, J.-M. Huang, C.-S. Ku, C.-M. Lin, H.-Y. Lee, and J.-Y. Juang. High mobility transparent conductive Al-doped ZnO thin films by atomic layer deposition. *Journal of Alloys and Compounds*, 727:565–571, 2017.

[138] V. V. Temnov, K. Sokolowski-Tinten, P. Zhou, A. El-Khamhawy, and D. von der Linde. Multiphoton ionization in dielectrics: Comparison of circular and linear polarization. *Phys. Rev. Lett.*, 97:237403, 2006.

[139] D. J. Little, M. Ams, P. Dekker, G. D. Marshall, J. M. Dawes, and M. J. Withford. Femtosecond laser modification of fused silica: the effect of writing polarization on Si-O ring structure. *Opt. Express*, 16(24):20029–20037, 2008.

[140] M. Ams, G. D. Marshall, and M. J. Withford. Study of the influence of femtosecond laser polarisation on direct writing of waveguides. *Opt. Express*, 14(26):13158–13163, 2006.

[141] D. Liu, Y. Li, M. Liu, H. Yang, and Q. Gong. The polarization-dependence of femtosecond laser damage threshold inside fused silica. *Appl. Phys. B*, 91(3):597, 2008.

[142] W. Gawelda, D. Puerto, J. Siegel, A. Ferrer, A. Ruiz de la Cruz, H. Fernández, and J. Solis. Ultrafast imaging of transient electronic plasmas produced in conditions of femtosecond waveguide writing in dielectrics. *Appl. Phys. Lett.*, 93(12):121109, 2008.

[143] D. Du, X. Liu, and G. Mourou. Reduction of multi-photon ionization in dielectrics due to collisions. *Appl. Phys. B*, 63(6):617–621, 1996.

[144] S. B. Arifzhanov, A. M. Danishevskii, E. L. Ivchenko, S. F. Kochegarov, and V. K. Subashlev. Role of the various types of transitions in three photon absorption in InAs. *Sov. Phys. JETP*, 47:88, 1978.

[145] A. M. Danishevskii, S. F. Kochegarov, and V. K. Subashlev. Three-photon absorption and linear-circular dichroism of InAs. *Sov. Phys. JETP*, 43:158, 1976.

[146] E. V. Chelnokov, N. Bityurin, I. Ozerov, and W. Marine. Two-photon pumped random laser in nanocrystalline ZnO. *Appl. Phys. Lett.*, 89(17):171119, 2006.

[147] H. Cao, Y. G. Zhao, S. T. Ho, E. W. Seelig, Q. H. Wang, and R. P. H. Chang. Random laser action in semiconductor powder. *Phys. Rev. Lett.*, 82:2278–2281, 1999.

[148] H. Cao, J. Y. Xu, S.-H. Chang, and S. T. Ho. Transition from amplified spontaneous emission to laser action in strongly scattering media. *Phys. Rev. E*, 61:1985–1989, Feb 2000.

[149] J. Shah. *Ultrafast Spectroscopy of Semiconductors and Semiconductor Nanostructures*. Springer Science & Business Media, Berlin Heidelberg, 2nd enlarged ed. 1999 edition, 1999.

[150] J.-C. Diels, W. Rudolph, P. F. Liao, and P. Kelley. *Ultrashort Laser Pulse Phenomena*. Academic Press, Amsterdam, Boston, 2. aufl. edition, 2006.

[151] J. Tian, G. Weng, Y. Wang, X. Hu, S. Chen, and J. Chu. Random lasing in ZnO nanopowders based on multiphoton absorption for ultrafast upconversion application. *ACS Appl. Nano Mater.*, 2(4):1909–1919, 2019.

[152] S. W. Eaton, A. Fu, A. B. Wong, C.-Z. Ning, and P. Yang. Semiconductor nanowire lasers. *Nat. Rev. Mater.*, 1(6):16028, 2016.

[153] R. Hollinger, D. Gupta, M. Zapf, R. Röder, D. Kartashov, C. Ronning, and C. Spielmann. Single nanowire defined emission properties of ZnO nanowire arrays. *J. Phys. D: Appl. Phys.*, 52(29):295101, 2019.

[154] R. Hollinger, P. Malevich, V. Shumakova, S. Ališauskas, M. Zapf, R. Röder, A. Pugžlys, A. Baltuška, C. Ronning, C. Spielmann, and D. Kartashov. Strong light-field driven nanolasers. *Nano Letters*, 19(6):3563–3568, 2019. PMID: 31117748.

[155] A. Johannes, S. Noack, W. Paschoal Jr., S. Kumar, D. Jacobsson, H. Pettersson, L. Samuelson, K. A. Dick, G. Martinez-Criado, M. Burghammer, and C. Ronning. Enhanced sputtering and incorporation of Mn in implanted GaAs and ZnO nanowires. *J. Phys. D: Appl. Phys.*, 47(39):394003, 2014.

[156] R. S. Wagner and W. C. Ellis. Vapour-Liquid-Solid Mechanism of Single Crystal Growth. *Appl. Phys. Lett.*, 4(5):89–90, 1964.

[157] Y. Xia, P. Yang, Y. Sun, Y. Wu, B. Mayers, B. Gates, Y. Yin, F. Kim, and H. Yan. One-Dimensional Nanostructures: Synthesis, Characterization, and Applications. *Adv. Mater.*, 15(5):353–389, 2003.

[158] L. E. Jensen, M. T. Björk, S. Jeppesen, A. I. Persson, B. J. Ohlsson, and L. Samuelson. Role of surface diffusion in chemical beam epitaxy of InAs nanowires. *Nano Letters*, 4(10):1961–1964, 2004.

[159] C. Zhang, F. Zhang, T. Xia, N. Kumar, J. Hahm, J. Liu, Z. L. Wang, and J. Xu. Low-threshold two-photon pumped ZnO nanowire lasers. *Opt. Express*, 17(10):7893–7900, 2009.

[160] R. Hollinger, Z. Samsonova, D. Gupta, C. Spielmann, R. Röder, L. Trefflich, C. Ronning, and D. Kartashov. Enhanced absorption and cavity effects of three-photon pumped ZnO nanowires. *Appl. Phys. Lett.*, 111(21):213106, 2017.

[161] C. F. Zhang, Z. W. Dong, G. J. You, S. X. Qian, and H. Deng. Multiphoton route to ZnO nanowire lasers. *Opt. Lett.*, 31(22):3345–3347, 2006.

[162] T. Nakamura, K. Firdaus, and S. Adachi. Electron-hole plasma lasing in a ZnO random laser. *Phys. Rev. B*, 86:205103, 2012.

[163] L. Zhang, K. Wang, Z. Liu, G. Yang, G. Shen, and P. Lu. Two-photon pumped lasing in a single CdS microwire. *Appl. Phys. Lett.*, 102(21):211915, 2013.

[164] Y. Gao, S. Wang, C. Huang, N. Yi, K. Wang, S. Xiao, and Q.i Song. Room temperature three-photon pumped $CH_3NH_3PbBr_3$ perovskite microlasers. *Sci. Rep.*, 7(1):45391, 2017.

[165] C. Karras, R. Röder, W. Paa, C. Ronning, and H. Stafast. Excitation energy dependent ultrafast luminescence behavior of cds nanostructures. *ACS Phot.*, 4(5):1067–1075, 2017.

[166] L. Tong, J. Lou, and E. Mazur. Single-mode guiding properties of subwavelength-diameter silica and silicon wire waveguides. *Opt. Express*, 12(6):1025–1035, 2004.

[167] B. E. A. Saleh and M. C. Teich. *Fundamentals of photonics*. Wiley-VCH, Weinheim, 2. ed. edition, 2008.

[168] A. V. Maslov and C. Z. Ning. Reflection of guided modes in a semiconductor nanowire laser. *Appl. Phys. Lett.*, 83(6):1237–1239, 2003.

[169] K. T. Fountaine, W. S. Whitney, and H. A. Atwater. Resonant absorption in semiconductor nanowires and nanowire arrays: Relating leaky waveguide modes to Bloch photonic crystal modes. *J. Appl. Phys.*, 116(15):153106, 2014.

[170] D. Akinwande, C. Huyghebaert, C.-H. Wang, M. I. Serna, S. Goossens, L.-J. Li, H. S P. Wong, and F. H. L. Koppens. Graphene and two-dimensional materials for silicon technology. *Nature*, 573(7775):507–518, 2019.

[171] J. R. Schaibley, H. Yu, G. Clark, P. Rivera, J. S. Ross, K. L. Seyler, W. Yao, and X. Xu. Valleytronics in 2D materials. *Nat. Rev. Mater.*, 1(11):16055, 2016.

[172] Y. Zheng, T. Niu, X. Ran, J. Qiu, B. Li, Y. Xia, Y. Chen, and W. Huang. Unique characteristics of 2D Ruddlesden–Popper (2DRP) perovskite for future photovoltaic application. *J. Mater. Chem. A*, 7:13860–13872, 2019.

[173] F. Langer, C. P. Schmid, S. Schlauderer, M. Gmitra, J. Fabian, P. Nagler, C. Schüller, T. Korn, P. G. Hawkins, J. T. Steiner, U. Huttner, S. W. Koch, M. Kira, and R. Huber. Lightwave valleytronics in a monolayer of tungsten diselenide. *Nature*, 557(7703):76–80, 2018.

[174] M. Baudisch, A. Marini, J. D. Cox, T. Zhu, F. Silva, S. Teichmann, M. Massicotte, F. Koppens, L. S. Levitov, F. J. García de Abajo, and J. Biegert. Ultrafast nonlinear optical response of Dirac fermions in graphene. *Nature Com.*, 9(1):1018, 2018.

[175] M. Volkov, S. A. Sato, F. Schlaepfer, L. Kasmi, N. Hartmann, M. Lucchini, L. Gallmann, A. Rubio, and U. Keller. Attosecond screening dynamics mediated by electron localization in transition metals. *Nat. Phys.*, 15(11):1145–1149, 2019.

[176] T. H. Maiman. Stimulated optical radiation in ruby. *Nature*, 187(4736):493–494, 1960.

[177] D. Strickland and G. Mourou. Compression of amplified chirped optical pulses. *Optics Com.*, 56(3):219 – 221, 1985.

[178] J. D. Jackson. *Classical Electrodynamics*. Walter de Gruyter, Berlin, 4. ed. edition, 2006.

[179] P. A. Franken, A. E. Hill, C. W. Peters, and G. Weinreich. Generation of optical harmonics. *Phys. Rev. Lett.*, 7:118–119, 1961.

[180] Y. R. Shen. *The principles of nonlinear optics*. Wiley-Interscience, New York, 1. aufl. edition, 2003.

[181] G. Cerullo and S. De Silvestri. Ultrafast optical parametric amplifiers. *Rev. Sci. Instrum.*, 74(1):1–18, 2003.

[182] U. Elu, T. Steinle, D. Sánchez, L. Maidment, K. Zawilski, P. Schunemann, U. D. Zeitner, C. Simon-Boisson, and J. Biegert. Table-top high-energy 7μm OPCPA and 260mJ Ho:YLF pump laser. *Opt. Lett.*, 44(13):3194–3197, 2019.

[183] C. Gaida, M. Gebhardt, T. Heuermann, F. Stutzki, C. Jauregui, J. Antonio-Lopez, A. Schülzgen, R. Amezcua-Correa, A. Tünnermann, I. Pupeza, and J. Limpert. Watt-scale super-octave mid-infrared intrapulse difference frequency generation. *Light Sci. Appl.*, 7(1):94, 2018.

[184] G. C. Bhar, P. Kumbhakar, A. K. Chaudhary, and U. Chatterjee. Tunable infrared generation in KTA and applications. *Pramana*, 53(2):321–330, 1999.

[185] K. L. Vodopyanov. Optical THz-wave generation with periodically-inverted GaAs. *Laser & Photonics Reviews*, 2(1-2):11–25, 2008.

[186] S. Witte and K. S. E. Eikema. Ultrafast optical parametric chirped-pulse amplification. *IEEE Journal of Selected Topics in Quantum Electronics*, 18(1):296–307, 2012.

[187] N. Thiré, R. Maksimenka, B. Kiss, C. Ferchaud, G. Gitzinger, T. Pinoteau, H. Jousselin, S. Jarosch, P. Bizouard, V. Di Pietro, E. Cormier, K. Osvay, and N. Forget. Highly stable, 15 W, few-cycle, 65 mrad CEP-noise mid-IR OPCPA for statistical physics. *Opt. Express*, 26(21):26907–26915, 2018.

[188] N. Thiré, R. Maksimenka, B. Kiss, C. Ferchaud, P. Bizouard, E. Cormier, K. Osvay, and N. Forget. 4-W, 100-kHz, few-cycle mid-infrared source with sub-100-mrad carrier-envelope phase noise. *Opt. Express*, 25(2):1505–1514, 2017.

[189] E. N. Osika, A. Chacón, L. Ortmann, N. Suárez, J. A. Pérez-Hernández, B. Szafran, M. F. Ciappina, F. Sols, A. S. Landsman, and M. Lewenstein. Wannier-bloch approach to localization in high-harmonics generation in solids. *Phys. Rev. X*, 7:021017, 2017.

[190] M. Baudrier-Raybaut, R. Haïdar, P. Kupecek, P. Lemasson, and E. Rosencher. Random quasi-phase-matching in bulk polycrystalline isotropic nonlinear materials. *Nature*, 432(7015):374–376, 2004.

Appendix

Appendix A

Femtosecond near and mid-IR laser pulses

The first realization of a laser device in 1962 by Th. Maiman [176] demonstrated the high spatial as well as temporal coherence properties of laser light. The possibility to operate a laser in a pulsed regime enables to bundle a high number of photons in a short time window and thus enables high light intensities. The need for high intensity laser sources, for academic as well as industrial applications [22], lead to the development of the chirped pulse amplification (CPA) technique which was honoured by the noble prize in 2018 [177]. In this thesis the interaction of intense femtosecond laser pulses in a wide spectral range from the near infrared (0.8 μm, 1.55 eV) to the far infrared (10 μm, 0.12 eV) with solid matter and nanostructures is investigated. A laser pulse is formed by a superposition of phase locked spectral modes, which form the spectrum of the pulse

$$F(\omega) = F_0 \cdot \exp\left[-2\ln(2)\frac{(\omega-\omega_0)^2}{\Delta\omega_{FWHM}^2}\right], \tag{A.1}$$

with the spectral amplitude F_0, central frequency ω_0 and spectral width (full width half maximum, FWHM) $\Delta\omega_{FWHM}$. In equation A.1 the phase of the spectral components was neglected. Applying a fast Fourier transformation, the electric field of a laser pulse

$$F(t) = \underbrace{F_{el} \cdot \exp\left[-2\ln(2)\frac{t^2}{\tau_{FWHM}^2}\right]}_{envelope} \cdot \exp\underbrace{[\mathrm{i}\omega_0 t]}_{phase} \tag{A.2}$$

in the time domain can be described by its envelope and phase [150]. With F_{el} is the field amplitude and τ_{FWHM} the full width half maximum of pulse duration. Because only the spectral and temporal structure of the pulse is from interest the spatial dependence of the laser field is neglected [167]. In the case of a transform limited Gaussian pulse (i.e. that any phase dependence is neglected), the FWHM spectral width $\Delta\omega_{FWHM}$ and the FWHM pulse duration

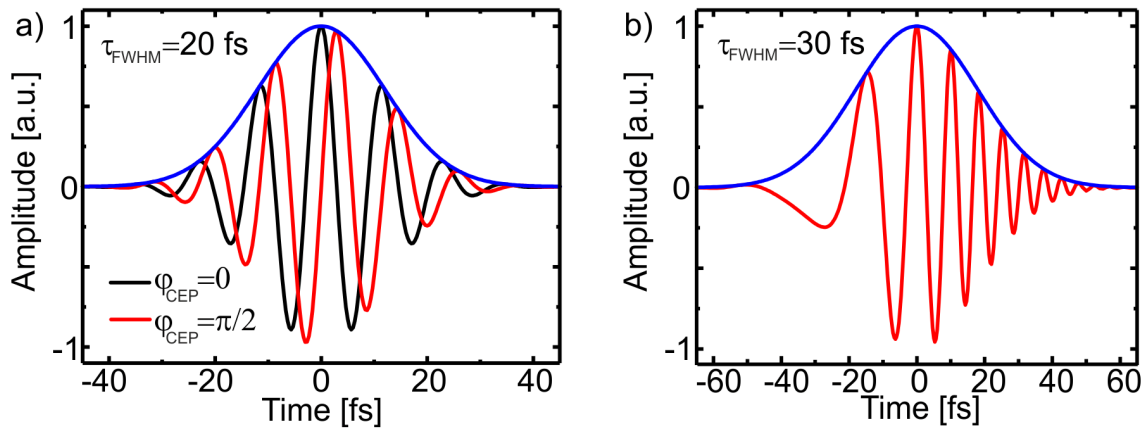

Figure A.1: a) Illustration of the calculated envelope and oscillatory part of a 20 fs laser pulse with a central wavelength at 3.5 μm. The black and the red lines depict the case when the CEP is 0 and π, respectively. b) Envelope and oscilating electric field of a pulse time dependent phase, i.e. a quadratic phase.

τ_{FWHM} are linked by the pulse duration bandwidth product

$$\tau_{FWHM}\Delta\omega_{FWHM} = 2\pi \cdot 0.44 \tag{A.3}$$

while the factor 0.44 appears for pulses with a Gaussian shape. The relationship described in Equation A.3 defines the shortest possible pulse for a given spectrum and implies that as broader a spectrum is, the shorter the corresponding pulse become [167].

Power density

The measure of the power density (which is equal to intensity) is given by the poynting vector

$$|\mathbf{S}(t)| = \frac{c\epsilon_0}{2}|\mathbf{F}_{el}(t)|^2 = |I(t)|. \tag{A.4}$$

Whereby ϵ_0 and c are the vacuum permittivity and the speed of light, respectively [178].

In practice the field amplitude F_0 or the related peak intensity I_0 of the laser pulse can not be measured directly. The measurable observable in the laboratory deals the average power P_{av} of the laser. Together with the pulse repetition rate f_{rep}, the pulse energy $E_{pulse} = P_{av}/f_{rep}$ can be determined. For a Gaussian pulse the peak intensity

$$I_0 = \frac{4}{\tau_{FWHM} w_0^2 \pi}\sqrt{\frac{\ln(2)}{\pi}}E_{\text{pulse}} \tag{A.5}$$

is determined from the pulse energy E_{pulse}, pulse duration τ_{FWHM} and the beam radius w_0^2 (measured at exp(-2) of its maximum).

Phase of a laser pulse:

Now the temporal and spectral phase of the laser pulse will be considered. The spectral phase

$$\phi_\omega = \phi_{CEP} + \phi_1 (\omega - \omega_0) + \frac{\phi_2}{2} (\omega - \omega_0)^2 \tag{A.6}$$

can be described using a series expansion. The constant term ϕ_{CEP} also know as carrier-envelope-phase (CEP) describes the phase offset between the envelope and the oscillatory part of the pulse (see Figure A.1 a). The linear term represents the oscillation frequency of the electric field ω_0, which is normally the central frequency or center of mass of the spectrum. Figure A.1 depicts the oscillatory part of the Fourier limited electric field and the envelope of a 20 fs laser pulse with a central wavelength at 3.5 μm (ω_0=0.5 PHz) for $\phi_{CEP} = 0$ (black) and $\phi_{CEP} = \pi/2$ (red). The relative group delay T_g of the spectral components is given by $\frac{\mathrm{d}\phi_\omega}{\mathrm{d}\omega}$. In the case of $\phi_2 = 0$, ϕ_1 defines the frequency independent group velocity (i.e. no dispersion). All higher order terms describe effects when the laser pulse spectrum varies with time as a result of dispersion, $\phi_2 = \frac{\mathrm{d}T_g}{\mathrm{d}\omega}$ also known as the group delay dispersion (GVD). In the case of $\phi_2 = 0$ the temporal variations of the phase $\mathrm{d}\phi_t/\mathrm{d}t$ is constant, i.e., all spectral components of the laser pulse propagate in phase. In this dispersion less case the pulse does not suffer from broadening while propagation. If $\phi_2 \neq 0$ the phase of the laser pulse (spectral components) varies over time, leading to pulse broadening. The effect of pulse broadening due to dispersion is called 'chirp', with the n-1 order of the exponent of $(\omega - \omega_0)^n$ describing the order of the chirp. In the mid-IR spectral range transparent material showing normal and anormal dispersion exist, what makes pulse stretching/compression using different types of materials possible[13]. Figure A.1 b depicts the the influence of a non-zero GVD on the pulse electric field.

Nonlinear optics:

Soon after the demonstration of the first laser device nonlinear light matter interaction was investigated [179]. The response of matter on light is described by the introduced polarization field P. For low light intensities the polarization field is proportional to the electric field. The proportionality factor is called electric susceptibility χ. Increasing the intensity new physical phenomena appear which can be described by a power series of the polarization field

$$P(t) = \chi_1(\omega)F_{el}(t) + \chi_2(\omega)F_{el}(t)^2 + \chi_3(\omega)F_{el}(t)^3 + ... \tag{A.7}$$

It is important to note that

$$\chi_1 >> \chi_2 >> \chi_3 >> ... \tag{A.8}$$

guarantees a convergence of Equation A.7 [75, 180].

While the second order nonlinear processes (χ_2) describes three-wave-mixing processes like

[13] A few GVD values in fs^2/mm of materials used for pulse compression at 3.1 μm wavelength: silicon 485, germanium 1468, CaF_2 -133, BaF_2 -64, YAG -460, sapphire -695

Second Harmonic Generation (SHG), Sum- and Difference-Frequency Generation (SFG and DFG), third order processes (χ_3) cover four-wave-mixing like third harmonic generation (THG) as well as the nonlinear Kerr-effect, explains an intensity dependent refractive index. Harmonic generation in frame of Eq. A.7 is called pertubative since the emission signal scales with I^n, while I is the laser power and n the nonlinear harmonic order. The symmetry properties of the material susceptibility χ determines if odd and even or only odd order harmonics are generated [180].

Appendix B

Optical parametric amplification (OPA)

An optical parametric amplifier (OPA) is a laser source based on the nonlinear optical parametric generation (OPG) process. This process can be explained, similar to sum-frequency and difference frequency generation by the χ_2 nonlinearty of crystalls. Figure B.1 depicts the χ_2 parametric nonlinear process. The input is given by a strong pump and a weak seed wave. The pump wave with a photon energy of $h\nu_p$ is split into the so called signal and idler wave carrying photon energies of $h\nu_s$ and $h\nu_i$, respectively. Due to energy conservation $h\nu_p = h\nu_s + h\nu_i$ must be valid. Further the momentum, $k_p = k_i - k_s$, of the pump wave has to be conserved in the nonlinear process, too. In case of non-collinear arrangement of pump and seed wave the momentum conservation additionally defines the angle of generated waves (Fig. B.1 d).

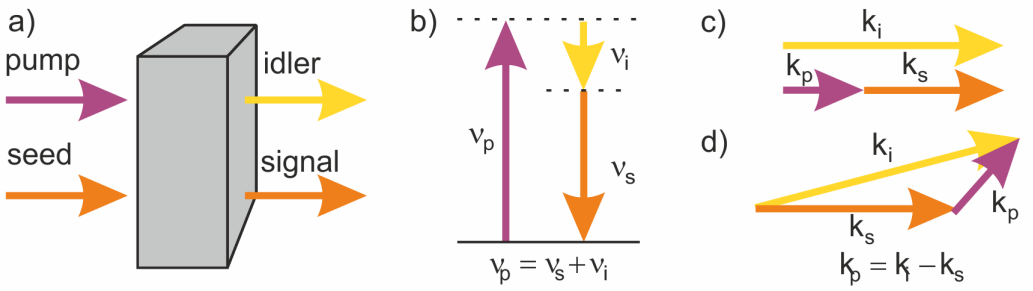

Figure B.1: a) Schematic illustration of the optical parametric generation (OPG) process. A pump and seed wave are converted into a signal and idler wave due to the χ_2 nonlinear OPG process. Three wave mixing process: b) Energy conserviation of the pump (ν_p), signal (ν_s) and idler (ν_i) photon energies contributing to the OPG process. c) and d) Momentum conservation of the pump (k_p), signal (k_s) and idler (k_i) photons contributing in a collinear and non-collinear OPG process, respectively.

The second input wave (Fig. B.1 a), called the seed wave, has the purpose to enhances the efficiency of the parametric process at the seed wave frequency and to control the phase of signal and idler wave. Because the pump wavelength is fixed, there is always a given idler (signal)

wavelength in the case the seed wave defines the signal (idler) wave due to energy conservation issues (see Fig. B.1 b) [167, 181].
To achieve high conversion efficiency, phase matching, i.e. matching of phase velocities, of the pump and signal/idler have to be achieved.
Further the group velocities of pump and signal/idler pulse have to be matched to achieve a high conversion bandwidth [75, 180].
In femtosecond OPA a femtosecond seed signal is amplified in a nonlinear optical parametric generation process by a femtosecond pump pulse. Compared to laser sources based on pumped gain media, this has several advantages:

1. Wavelength tunability
2. High gain bandwidth enables the generation of few-cycle laser pulses
3. High temporal contrast of laser pulse due to the instantaneous nature of parametric amplification
4. No thermal loading effects because the parametric generation process includes only virtual states, no excitation of the gain material

Generation of femtosecond mid-IR laser pulses
In this work, investigations on the interaction of intense femtosecond laser pulses in the near to the far-IR spectral range with condensed matter are presented. In the following part the OPA configuration used for experiments are briefly introduced.
As explained above in the parametric amplification system a pump wave amplifies a signal and idler wave in a nonlinear crystal. Thus one key part of a femtosecond OPA is the femtosecond pump laser providing the pump wave. For a stable and high quality output performance of an OPA their are high standards on the spatial and temporal pump beam parameters. Further the pump laser performance must be very stable to avoid power fluctuations of the parametric process. Nowadays chirped pulse amplifications systems using titan doped sapphire (Ti:Sa) and ytterbium doped glasses (e.g. Yb:CaF_2) laser materials reach the expected performance and are widely used [14]. Second a nonlinear material with a high χ_2 value and damage threshold which can be grown defect free with large apperature size are needed. Additionally for high conversion efficiency the pump wave phase velocity must be matched to the signal and idler wave phase velocity. To develop a proper constellation of pump laser and nonlinear materials cover all required parameters is still part of active research and beyond the scope of this thesis. Thus only the configurations of pump laser and nonlinear crystals used in this thesis will be discussed briefly.

[14] Newest approaches to generate femtosecond laser pulses in the mid-IR are using thulium and holmium doped glasses as laser materials which emit around $2\,\mu$m [182, 183]. Because such a system was not used in this work and the OPAs pumped by thulium and holmium lasers are still rare it will not be considered here.

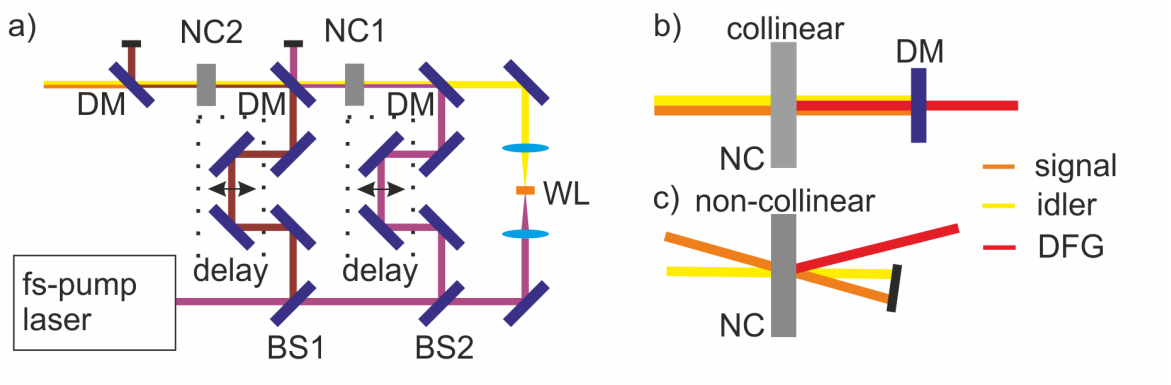

Figure B.2: a) Schematic illustration of a white light seeded and femtosecond laser pumped optical parametric amplifier (OPA). The pump laser power is splitted in three parts using beamsplitter (BS1 and BS2). A very small fraction of the pump laser power is used to generate the white light seed (WL) using the nonlinear Kerr-effect (self-focusing and self-phase-modulation) in a piece of glass, e.g. YAG or sapphire. The seed is subsequently overlapped with parts of the pump laser in nonlinear crystals (NC1 and NC2) to perform the parametric amplification prcoess. The temporal overlap of the seed and pump pulse is adjusted by delay lines at every OPA stage seperately. After every OPA stage, i.e. after every nonlinear crystal, the generated signals are seperated from the pump laser, e.g. using dichroic mirrors (DM). b) and c) Frequency downconversion using the difference frequency generation (DFG) process between the signal and idler wave in a nonlinear crystal (NC). b) and c) illustrate the collinear and non-collinear DFG arrangement. Adopted from [181].

1. Ti:Sa (0.8 μm) pumped OPA based on beta-barium borat (BBO) nonlinear crystal. The signal and idler wave range from 1.2 to 1.6 μm and from 1.6 to 2.8 μm, respectively.

2. Yb:CaF_2 (1.03 μm) pumped OPA based on potassium titanyl arsenate (KTA) nonlinear crystal The signal and idler wave are tunable in the range from 1.4-2.0 μm and 2.0-4.0 μm, respectively. This is especially promising because it allows to transform a pump photon from the near-IR directly to mid-IR.
   The signal and idler output of a Yb:CaF_2 pumped KTA based OPA was used for experiments presented in Section 5.

Figure B.2 depicts the schematic illustration of a white light seeded two-stage OPA. The pump laser from a CPA laser system is devided in 3 parts using beamsplitters (BS1 and BS2). First only a few percent of the pump beam, is used for white light generation by self phase modulation in a thin glass plate (e.g. sapphire, YAG) with the aim to generate the seed signal for the first OPA stage, the so called preamplifier. The seed signal is amplified in the first and second OPA stage by overlapping the seed signal with the pump in nonlinear crystals (NC1 and NC2). The timing between all waves (seed and pump of respective stage) are adjusted by separate delay lines (DL). Dichroic mirrors (DM) are used after every OPA stage to separate the generated waves from the pump beam.
To generate ultrashort laser pulses at even longer wavelengths, difference frequency mixing of the signal and idler wave has to be performed. Similar considerations which were done for the chosen OPA nonlinear crystal have to applied here, too. In the presented work two different

nonlinear crystals for DFG between the signal and idler wave from a BBO based OPA were used. To generate femtosecond laser pulses up to roughly 5 μm wavelength a KTA crystal was used [184]. To avoid absorption above 5 μm and to enable DFG up to 18 μm a gallium selenide (GaSe) crystal [185] was used.
Experimental results were the signal and idler wave output of a Ti:Sa pumped BBO based OPA and the DFG-signal generated in a KTA and GaSe crystal are presented in Section 4.
Due to the operation scheme of a femtosecond OPA, that a femtosecond seed signal is overlapped by a femtosecond pump pulse, the power scaling of such devices are limited by gain saturation and the nonlinear crystal damage threshold. To avoid this effects the spot size of the pump and seed pulses have to be expanded, therefore large aperture and high quality crystals are needed, what is technically and economically difficult. To circumstance this problem, the peak intensity of the pump pulse can be reduced by temporally stretching the pulse. In optical parametric chirped pulse amplification (OPCPA) systems the light amplification based on a parametric generation in a nonlinear crystal, identical to OPA, is performed using seed and pump pulses with a durations in the picosecond range. To obtain ultrashort (femtosecond) pulses it is important that the seed-phase can be compensated after the OPA processes in order to recompress the pulse [186].
In a OPCPA system, the narrowband, picoseconds long, but powerful pump beam overlaps with a seed pulse stretched to picoseconds duration in a nonlinear crystal. The amplified spectral bandwidth is determined by phase-matching conditions and the ratio of the pump- and seed pulse duration. OPCPA inherits many of the above discussed attractive features from OPA, thus OPCPA systems nowadays are reliable sources of high power, high repetition rate, CEP-stable ultrashort laser pulses in the near as well as in the mid-IR spectral range [186].

Appendix C

High repetition rate, few-cycle, CEP controllable OPCPA laser source

Figure C.1 depicts a schematic illustration of the optical parametric chirped pulse amplification laser system (OPCPA, Fastlite Starzz) operated at the Extreme Light Infrastructure-Attosecond Light Pulse Source (ELI-ALPS) in Szeged, Hungary. In a first step a small fraction of the pi-

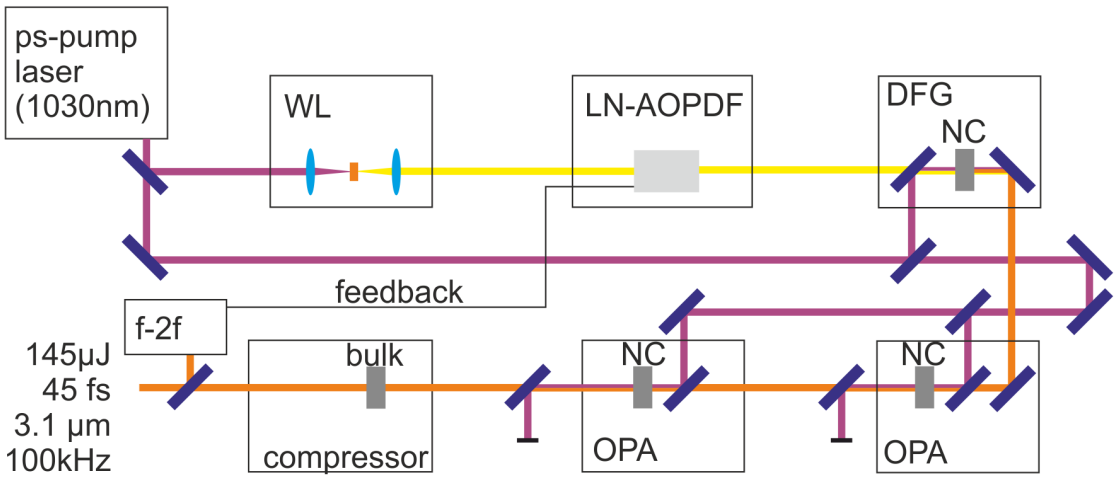

Figure C.1: Schematic illustration of the optical parametric chirped pulse amplification (OPCPA) system used to investigate the CEP dependence of high harmonic generation in bulk ZnO. Adopted from [187].

cosecond pump laser operating at 1030 nm is used to generate a broad band continuum via white light generation (WL). The phase of the white light is controlled in a Lithium Niobate ($LiNbO_3$) acousto-optic programmable dispersive filter (LN-AOPDF, Fastlite). Next the difference frequency generation (DFG) between the pump beam and the white light seed is performed with the aim to obtain a CEP stable seed beam in the mid-IR at 3.2 μm. This seed pulse is amplified

in three OPA stages based on MgO-doped periodically poled Lithium Niobate (MgO-PPLN) nonlinear crystals (NC) before the pulses are compressed in bulk silicon material [187, 188].

Appendix D

Triangular vs. sinusoidal CEP variation

Figure D.1 depicts the high harmonic spectra generated in crystalline ZnO as a function of the laser pulse CEP. In the experiment the CEP was varied by a acusto-optical phase modulator (Fastlite, Dazzler) controlled by an alternating voltage. Figure D.1 a and b shows the results when a triangular and a sinusoidal voltage waveform is applied, respectively. The used voltage waveform is clearly imprinted in the interference pattern between the 7^{th} and 9^{th} as well as between the 9^{th} and 11^{th} harmonic.

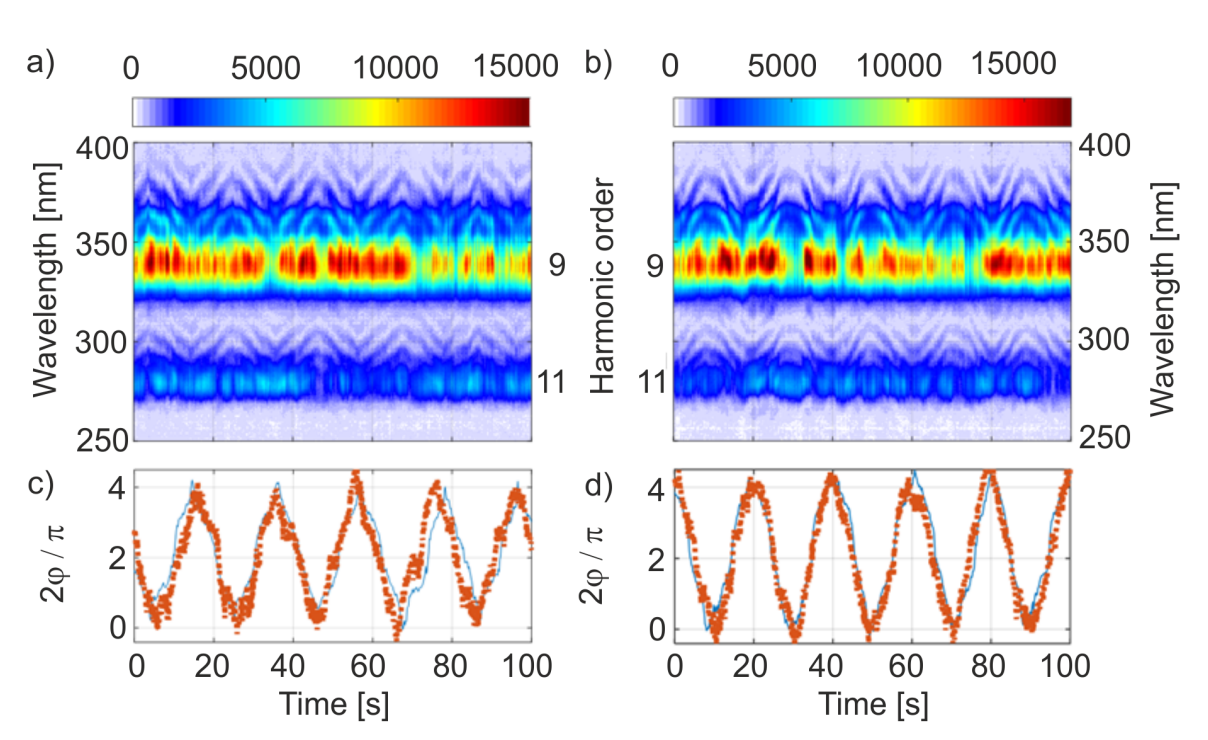

Figure D.1: High harmonic emission from ZnO as a function of the CEP. The CEP was varied by a a) triangular and b) sinusoidal voltage pattern.

Appendix E

HHG in ZnO thin films

As shown in Figure 4.12 higher order harmonics are efficiently generated in the used polycrystalline ZnO thin films when irradiated with mid-IR femtosecond laser pulses. Figure E.1 a depicts the emission spectrum from a ZnO thin irradiated by a 3.75 μm laser pulse in the range of the sensitivity of the used spectrometer. Beside the lasing peak at 400 nm, harmonic orders from the near infrared (5^{th}, 750 nm) down to the ultraviolet (15^{th}, 250 nm) spectral region are detected. In Figure E.1 b the integrated yield of the individual harmonics as a function of laser intensity is shown. Every harmonic order shows a similar scaling what proves the non-pertubative generation mechanism. Remarkable the grains, enhance scattering, do not reduce

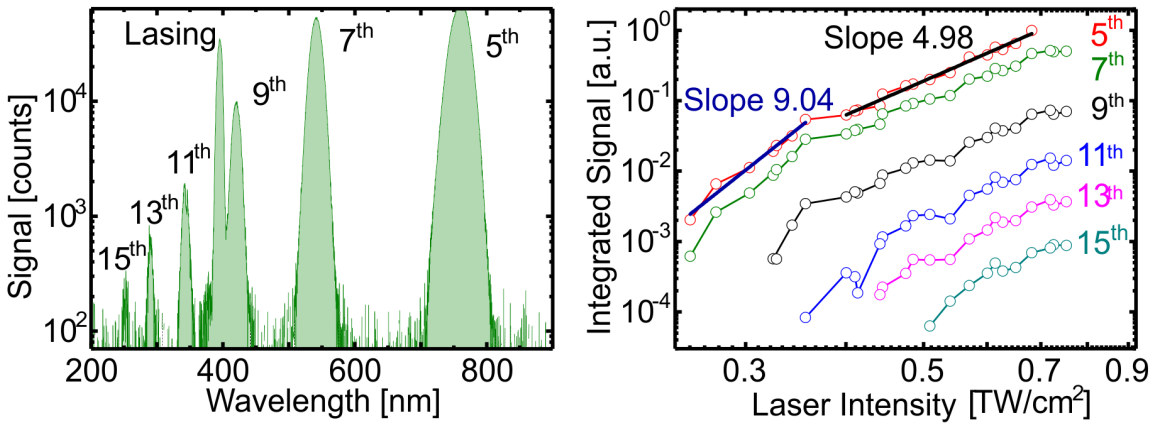

Figure E.1: a) High harmonic spectra generated from a roughly 100 fs pulse at 3.75 μm. b) The integrated yield of the harmonics as a function of the mid-IR laser intensity. The similar scaling of the observed harmonic orders are a prove for the non-pertubative generation mechanism.

HHG yield.

If we adopt the three-step model of HHG to solids the oscillatory radius of the quasi free elec-

tron [189]

$$x_{max} = \frac{eF_{el}\lambda^2}{4\pi m_e c^2} \tag{E.1}$$

is determined by the wavelength λ and field strength F_{el} of the laser, e is the elementary charge, c the vacuum speed of ligth and m_{e} the effective mass of the electron ($0.29\,m_0$, with m_0 the rest mass of an electron). Using the present parameters a maximum oscillatory radius of roughly 40 nm is calculated. Thus the electrons can be effectively driven inside a crystalline grain without immediately scattering with a grain boundary.

Experiments showed a much more efficient HHG in intrinsic polycrystalline ZnO films with parameters given in Section 4.1.1 compared to crystalline bulk with a thickness down to $100\,\mu$m. Werner *et al.* [74] suggested random quasi-phase matching (RQPM) as the responsible process increasing the efficiency. Here phase matching of the fundamental wave and the generated harmonic field (see Figure B.1) is achieved without any preferential materialsorientation or specific polarization selection rules. Further any wavelength-dependent resonant size effects can be neglected [190].

List of abbreviations and symbols

Abbreviations

Å	Ångström
a.u.	arbitrary units
at.	Atom
ACF	Autocorrelation Function
AGS (AgGaS)	Silver Gallium Sulfide
Al	Aluminium
ASE	Amplified Spontaneous Emission
BBO	Beta Barium Borat
CaF_2	Calciumfluorid
CB	Conduction Band
CCD	Charged Coupled Device
CdS	Cadmium Sulfide
CdSe	Cadmium Selenide
CE	Carrier Envelop
CEP	Carrier Envelop Phase
cm	Centimeter
CPA	Chirped Pulse Amplification
DECP	Displaceive Excitation of Coherent Phonons
DFG	Difference Frequency Generation
DOS	Density of States
EHP	Electron Hole Plasma
ELI-ALPS	Extrem Light Infrastructure-Attosecond Light Pulse Source
eV	Electron Volt
far IR	Far Infrared
FFT	Fast Fourier Transformation
fs	Femtosecond
FWHM	Full Width Half Maximum

FP	Fabry Pérot
FPM	Fabry Pérot Mode
FROG	Frequency Resolved Optical Gating
GaSe	Gallium Selenide
GVD	Group Velocity Dispersion
FCA	Free Carrier Absorption
HE	Fundamental mode
HgCdTe	Mercury Cadmium Telluride
HHG	High Harmonic generation
INRS-EMT	National Institute of Scientific Research- Energy, Materials and Telecommunications
ISRS	Impulsive Stimulated Raman Scattering
KTA	Potassium Titanyle Arsenate
keV	Kilo Electron Volt
kHz	Kilohertz
μm	Micrometer
m	Meter
MgO	Magnesium Oxide
mid IR	middle Infrared
mJ	Millijoule
MO	Microscope Objective
NW	Microwire
NA	Numerical Aperture
NIR	Near Infrared
nm	Nanometer
NUV	Near Ultra Violet
NW	Nanowire
OPA	Optical Parametric Amplification
OPCPA	Optical Parametric Chirped Pulse Amplification
PHz	Petahertz
PL	Photoluminescence
PMT	Photo Multiplier Tube
ps	Picosecond
RF	Radio Frequency
SEM	Scanning Electron Microscope
SFG	Sum Frequency Generation
SH	Second Harmonic
SHG	Second Harmonic Generation

Si	Silicon
SiO_2	Silicon Dioxide
TD-DFT	Time Dependent-Density Functional Theory
TE	Transverse Electric
TFP	Thin Film Polarizer
THz	Terrahertz
THG	Third Harmonic Generation
Ti:Sa	Titanium doped Saphire
TPA	Three Photon Absorption
TW	Terrawatt
UV	Ultra Violet
WG	Wire Grid
V	Volt
VB	Valence Band
VIS	Visible
VLS	Vapour Liquid Solid
VPT	Vapour Transport Technique
XRD	x-ray Diffraction
XUV	Extrem Ultra Violet
YAG	Yttrium Aluminium Granat
Yb	Ytterbium
Yb:CaF_2	Ytterbium doped Calciumfluorid
ZnO	Zinc Oxide

Symbols

$\hbar$	Reduced Planck's constant ($1.06 \cdot 10^{-34}$ m^2kg/s)
c	Speed of light ($3 \cdot 10^8$ m/s)
ϵ_0	Electric permittivity ($8.85 \cdot 10^{-12}$ As/Vm)
e	Electric charge $1.6 \cdot 10^{-19}$ C
π	3.14
n_r	Refractive index ZnO
λ_{ZnO}	Wavelength of light in the matter ($=\lambda/n_r(\lambda)$)
$\alpha_{3,lin}$, $\alpha_{3,circ}$	Three photon absorption coefficient in the case of linear and circular polarized light
α_A, α_B	Three photon absorption coefficients according to the model given in [32]
I_S	Three photon absorption saturation intensity
$^\circ C$	Degree Celsius, unit for Temperature
β	Propagation constant of a guided mode

Δf	Cavity spectral mode spacing
L	Cavity length
Γ	Nanowire waveguide confinement factor
R	Reflectivity
$g(\lambda)$	Spectrally resolved ZnO gain spectrum
g_0	Constant ZnO gain value
n_0	Excited Carrier density necessary to observe lasing (inversion density)
n_C	Saturation carrier density
I_{th}	Threshold pump intensity to observe lasing
α_{w}	Cavity losses (without reflectivity losses from the end mirrors)
T_{e}, T_{h}	Electron and hole temperature
T_{l}	Lattice temperature
μ_{e}, μ_{h}	Quasi Fermi level of electrons and holes
s	Photon density
n_{e}	Thermalized excited electron density
n_{e}^*	Non thermalized (hot) excited electron density
n_{FCA}	Carrier density excited via impact ionization subsequent free carrier absorption
E_{e}	Critical energy of impact ionization
γ_{s}	Electron scattering rate (Drude model)
τ_{C}	Cooling time
τ_{e}	Spontaneous recombination time
τ_{s}	Photon lifetime
E_{g}	Band gap
m^*	Effective mass ZnO ($0.29{\cdot}m_0$)
m_0	Electron rest mass ($9.11 \cdot 10^{-31}$ kg)
γ	Keldysh parameter
$E_{\mathrm{g,eff}}$	Modified band gap used in Kelysh formalism considering the Stark effect
$K(x)$, $E(x)$	Complete elliptical integrals of the first and second kind
U_{p}	Pondermotive energy
E_g^{MP}	Modified band gap used in Kelysh formalism in the multiphoton absorption limit
N	Number of absorbed photons
n	Harmonic or nonlinear order
Π_{n}	Harmonic signal of n^{th}-order (intensity)
ϕ_{int}	Phase of interfering harmonic orders
ϕ_0	Constant phase term of interfering harmonic orders
$\Delta\phi_{\mathrm{int}}$	Intrinsic phase introduced by the HHG process (atto-chirp)
v_{g}	Group velocity

$\lambda_{\text{x-ray}}$	X-ray wavelength used for XRD characterization of ZnO thin films
Δ_{FWHM}	FWHM width of XRD rocking curve
Θ	Diffraction angle XRD
Θ_{B}	Bragg angle
θ	Cut angle nonlinear crystals
Ω	Oscillation frequency phonon mode
τ_{Phonon}	Oscillation periode phonon oscillation
Q	Lattice displacement
d	Thickness sample
ΔT	Pump-probe delay
Δt	Group delay between the red and blue part of two adjacent harmonic orders
t	Time
λ	Wavelength
ω	Angular frequency
$W(t)$	Mutual energy transfer of a laser pulse with induced polarization field in matter
λ_0	Central wavelength laser pulse spectrum
ω_0	Central angular frequency laser pulse spectrum
$F(\omega)$	Laser pulse spectrum
$F(t)$	Laser pulse time domain
F_0	Laser pulse spectral amplitude
F_{el}	Laser pulse amplitude, time domain
$\Delta\omega_{\text{FWHM}}$	Laser pulse FWHM spectral width (angular frequency)
$\Delta\lambda_{\text{FWHM}}$	Laser pulse FWHM spectral width (wavelength)
τ_{FWHM}	Laser pulse FWHM duration
ϕ_{CEP}	Carrier envelope phase, constant phase term
ϕ_1	Linear laser phase term
ϕ_2	Quadratic laser phase term
$S(t)$	Poynting vector
$P(t)$	Polarization field
χ_1	Linear order of material susceptibility
χ_2	Quadratic order of material susceptibility
χ_3	Cubic order of material susceptibility
I_0	Laser pulse peak intensity
E_{pulse}	Laser pulse energy
w_0	Laser pulse beam radius (exp(−2)-width)
T_{g}	Laser pulse group delay

List of Figures

List of publications

Publications in peer-reviewed journals

R. Hollinger, D. Hoff, P. Wustelt, S. Skruszewicz, Y. Zhang, H. Kang, D. Würzler, T. Jungnickel, M. Dumergue, A. Nayak, R. Flender, L. Haizer, M. Kurucz, B. Kiss, S. Kühn, E. Cormier, Ch. Spielmann, G. G. Paulus, P. Tzallas, M. Kübel (2020): Carrier-envelope-phase measurement of few-cycle mid-infrared laser pulses using high harmonic generation in ZnO, In: Optics Expess: 28, 7314

R. Hollinger, D. Gupta, M. Zapf, M. Karst, R. Röder, I. Uschmann, U. Reislöhner, D. Kartashov, C. Ronning, Ch. Spielmann (2019): Polarization dependent multiphoton absorption in ZnO thin films, In: Journal of Physics D: Applied Physics, 53, 055102

R. Hollinger, P. Malevich, V. Shumakova, S. Ališauskas, M. Zapf, R. Röder, A. Pugžlys, A. Baltuška, C. Ronning, Ch. Spielmann, D. Kartashov (2019): Strong light-field driven nanolasers, In: Nano Letters, 19, 3563

R. Hollinger, D. Gupta, M. Zapf, R. Röder, D. Kartashov, C. Ronning, Ch. Spielmann (2019): Single nanowire defined emission properties of ZnO nanowire arrays, In: Journal of Physics D: Applied Physics, 52, 295101

Z. Samsonova, S. Höfer, **R. Hollinger**, T. Kämpfer, I. Uschmann, R. Röder, L. Trefflich, O. Rosmej, E. Förster, C. Ronning, D. Kartashov, Ch. Spielmann (2018): Hard X-ray Generation from ZnO Nanowire Targets in a Non-Relativistic Regime of Laser-Solid Interactions, In: Applied Sciences, 8, 1728

R. Hollinger, Z. Samsonova, D. Gupta, Ch. Spielmann, R. Röder, L. Trefflich, C. Ronning, D. Kartashov (2017): Enhanced absorption and cavity effects of three-photon pumped ZnO nanowires, In: Applied Physics Letters, 111, 213106

Publications in preparation

N. C. Geib, **R. Hollinger**, E. Haddad, P. Herrmann, F. Légaré, T. Pertsch, Ch. Spielmann, M. Zürch, F. Eilenberger: Simplified dispersion scan setup for measuring few-cycle laser pulses in the mid-infrared.

R. Hollinger, V. Shumakova, T. Lettau, M. Zürch, Ch. Spielmann, A. Pugžlys, A. Baltuška, U. Peschel, S. Gräfe, D. Kartashov: Ultrafast lattice dynamics in semiconductors traced by high-order harmonic generation.

R. Hollinger, E. Haddad V. Shumakova, M. Zapf, R. Röder, P. Herrmann, I. Uschmann, U. Reislöhner, M. Zürch, A. Pugžlys, A. Baltuška, F. Légaré, D. Kartashov, C. Ronning, Ch. Spielmann: Role of free carriers in the absorption of intense long wavelength light.

Conference talks

R. Hollinger, P. Malevich, V. Shumakova, S. Ališauskas, U. Reislöhner, M. Zapf, M. Karst, D. Gupta, I. Uschmann, R. Röder, A. Pugžlys, A. Baltuška, C. Ronning, Ch. Spielmann, D. Kartashov, Nanoscale semiconductor laser sources pumped in strong field regime, International Conference on Metamaterials and Nanophotonics – MetaNano, St-Petersburg, Russia, July 2019

D. Kartashov, **R. Hollinger**, V. Shumakova, A. Schleusener, Ch. Reichardt, J. Irrek, A. Baltuška, A. Pugžlys, M. Wächtler, Ch. Spielmann, High harmonic generation in arrays of CdSe quantum dots, Conference on Lasers and Electro-Optics/Europe and the European Quantum Electronics, Munich, Germany, June 2019

R. Hollinger, V. Shumakova, A. George, Z. Tang, Ch. Spielmann, A. Baltuška, A. Pugžlys, A. Turchanin, D. Kartashov, Comparative study of high order harmonic generation in monolayer-thick semiconductors, Conference on Lasers and Electro-Optics/Europe and the European Quantum Electronics, Munich, Germany, Germany, June 2019

S. Khujanov, D. Kartashov, **R. Hollinger**, Ch. Spielmann, Time-resolved third harmonic generation spectroscopy of coherent phonons in bulk ZnO, DoKDoK – Doctoral Student Conference on Optics, Friedrichroda, Germany, September 2018

R. Hollinger, V. Shumakova, A. Pugžlys, A. Baltuška, S. Khujanov, Ch. Spielmann, D. Kartashov, High-order harmonic generation traces ultrafast coherent phonon dynamics in ZnO, Ultrafast Phenomena XXI, Hamburg, Germany, July 2018 – **accepted as post deadline submission**

R. Hollinger, P. Malevich, V. Shumakova, S. Ališauskas, L. Trefflich, R. Röder, A. Pugžlys, A. Baltuška, C. Ronning, Ch. Spielmann, D. Kartashov, Semiconductor laser optically pumped in the tunneling regime, Deutsche Physikalische Gesellschaft - Frühjahrestagung, Erlangen, Germany, March 2018

R. Hollinger, V. Shumakova, R. Röder, A. Pugžlys, A. Baltuška, C. Ronning, Ch. Spielmann, D. Kartashov, Coexistence of high-order harmonic generation and lasing in CdS nanowires, DoKDoK – Doctoral Student Conference on Optics, Suhl, Germany, September 2017.

R. Röder, **R. Hollinger**, Z. Samsonova, Ch. Spielmann, C. Ronning, D. Kartashov, High intensity light-nanowire interaction: From tunnel excitation for nanowire lasing to hard X-Ray generation, Material research Society - Fall meeting, Boston, USA, 2017.

R. Hollinger, S. Ališauskas, V. Shumakova, L. Trefflich, R. Röder, A. Pugžlys, D. Kartashov, A. Baltuška, C. Ronning, Ch. Spielmann, From three-photon to tunnel ionization pumped ZnO nanolasers, Conference on Lasers and Electro-Optics/Europe and the European Quantum Electronics, Munich, Germany, June 2017.

R. Hollinger, Z. Samsonova, D. Kartashov, R. Röder, L. Trefflich, C. Ronning, Ch. Spielmann, Stimulated UV Emission from ZnO nanostructures pumped by intense NIR laser pulses,DoKDoK – Doctoral Student Conference on Optics, Opburg, Germany, September 2016.

Conference posters

R. Hollinger, V. Shumakova, A. Pugžlys, A. Baltuška, Ch. Spielmann, D. Kartashov, "Coherent optical phonons traced by high harmonic generation in ZnO", ETSF-workshop on electronic excitations, Jena, Germany, September 2019.

R. Hollinger, P. Malevich, V. Shumakova, S. Ališauskas, U. Reislöhnen. M. Zapf, M. Karst, D. Gupta, I. Uschmann, R. Röder, A. Pugžlys, A. Baltuška, C. Ronning, Ch. Spielmann, D. Kartashov, Novel optical pumping regime for semiconductor nanolasers, International conference on Nano- and Metamaterials – Nanometa, Seefeld, Austria, January 2018.

R. Hollinger, P. Malevich, V. Shumakova, S. Ališauskas, L. Trefflich, R. Röder, A. Pugžlys, A. Baltuška, C. Ronning, Ch. Spielmann, D. Kartashov, Semiconductor laser optically pumped in the tunnel excitation regime, Ultrafast Phenomena XXI, Hamburg, Germany 2018.

R. Hollinger, P. Malevich, V. Shumakova, S. Ališauskas, L. Trefflich, R. Röder, A. Pugžlys, A. Baltuška, C. Ronning, Ch. Spielmann, D. Kartashov, Wavelength independent threshold for stimulated emission in ZnO nanowires under nonlinear pumping in the range from 0.8 to 4 μm, International conference on multiphoton processes, Budapest, Hungary 2017.

Z. Samsonova, **R. Hollinger**, D. Kartashov, M. Zürch, R. Röder, L. Trefflich, C. Ronning, Ch. Spielmann, Second Harmonic Generation from ZnO Nanostructured Surface by Femtosecond Laser Pulses at Near Damage Threshold Intensities, Conference on Lasers and Electro-Optics/Europe and the European Quantum Electronics, Munich, Germany, June 2015

Acknowledgement

Finally I want to thank all those people who made this thesis possible. This is by no means a completely list of people who made important contributions.

In particular I would like to thank my doctoral supervisor Prof. Dr. Christian Spielmann. Thank you for your trust over the past 7 years and the opportunities you have given me.

Special thanks goes to the postdocs I worked with and from who I learned: Dr. D. Kartashov, Dr. M. Zürch, and Dr. S. Höfer. Most of my practical skills and most of my knowledge I owe to you.

All colleagues and collaborators I worked with.
IOQ QE: Dr. A. Hoffmann, Dr. B. Landgraf, Dr. R. Sollapur, F. Tuitje, T. Helk, Dr. Z. Sun, M. Mallick, Harshita, V. Korolev, Dr. Z. Sansonova, P. Herrmann, D. Gupta, M. Karst, E. E. Zadeh
IOQ NLO: Prof. Dr. G. G. Paulus, Dr. M. Kübel, Dr. P. Wustelt, S. Skruszewicz, D. Hoff
IOQ X-ray group: Dr. I. Uschmann, Dr. K. S. Schulze, Dr. R. Lötsch, A. Schmitt
IFP: Prof. Dr. C. Ronning, Dr. R. Röder, M. Zapf.
IAP: N. Geib, Dr. F. Eilenberger
TU Vienna: Prof. Dr. A. Baltuska, Dr. A. Pugzlys, Dr. V. Shumakova, Dr. P. Malevich, Dr. S. Alisauskas, E. Kaksis, I. Astrauskas
INRS Varennes: Prof. Dr. F. Légaré, E. Haddad
Prof. Dr. S. Gräfe, Prof. Dr. S. Botti, Dr. M. Wächtler
Thank you for your support. This work would not have been possible without your help.

Moreover, I would like the thank H. Marschner, M. Damm, B. Beleites, F. Ronneberger for their continuous support over all the years I have been working in the IOQ.

Extraordinary thanks goes to my family. My Parents and brothers for their strong support throughout my whole life. Without your support, this work, my entire studies, would not have been possible.

Last but not least I want to say thanks to all my friends in Jena. All the nice people I met related to the university, Cucuma e.V. Freie Bühne Jena e.V., Frei-Raum e.V., Crossroads e.V..

Ehrenwörtliche Erklärung

Ich erkläre hiermit ehrenwörtlich, dass ich die vorliegende Arbeit selbständig, ohne unzulässige Hilfe Dritter und ohne Benutzung anderer als der angegebenen Hilfsmittel und Literatur angefertigt habe. Die aus anderen Quellen direkt oder indirekt übernommenen Daten und Konzepte sind unter Angabe der Quelle gekennzeichnet.

Bei der Auswahl und Auswertung folgenden Materials haben mir die nachstehend aufgeführten Personen in der jeweils beschriebenen Weise unentgeltlich geholfen:

1. Die Gruppe um Prof. A. Baltuška (TU Wien, Österreich). Entwicklung, Bereitstellung und Betreuung des in Kapitel 5 benutzen OPA-Lasersystesms.

2. Die Gruppe um Prof. F. Légaré (INRS Varennes, Kanada). Entwicklung, Bereitstellung und Betreuung des in Kapitel 4 benutzen OPA-Lasersystesms.

3. Die Gruppe um Prof. R. Ronning (IFP, FSU Jena, Deutschland). Synthese der ZnO und CdS Nanodraht und Dünnschichtproben, welche in Kapitel 4 und 5 dieser Arbeit verwendet wurden.

4. Die Gruppe um Dr. S. Makarov (ITMO, St. Petersburg, Russland). Synthese der Perovskit-Proben, welche in Kapitel 5 untersucht wurden.

5. Ingo Uschmann (IOQ, FSU Jena, Deutschland). XRD-Charakterisierung der ZnO Dünnschichtproben

6. ELI-ALPS, Ungarn. Entwicklung, Bereitstellung und Betreuung des in Kapitel 3 benutzten CEP-kontrollierbaren OPCPA-Lasersystesms.

Weitere Personen waren an der inhaltlich-materiellen Erstellung der vorliegenden Arbeit nicht beteiligt. Insbesondere habe ich hierfür nicht die entgeltliche Hilfe von Vermittlungs- bzw. Beratungsdiensten (Promotionsberater oder andere Personen) in Anspruch genommen. Niemand hat von mir unmittelbar oder mittelbar geldwerte Leistungen für Arbeiten erhalten, die im Zusammenhang mit dem Inhalt der vorgelegten Dissertation stehen.

Die Arbeit wurde bisher weder im In- noch im Ausland in gleicher oder ähnlicher Form einer anderen Prüfungsbehörde vorgelegt.

Die geltende Promotionsordnung der Physikalisch-Astronomischen Fakultät ist mir bekannt.

Ich versichere ehrenwörtlich, dass ich nach bestem Wissen die reine Wahrheit gesagt und nichts verschwiegen habe.

Jena, den 04.05.2020

.....

Richard Hollinger